

JWST Observations of Young protoStars (JOYS+): Detection of icy complex organic molecules and ions

I. CH₄, SO₂, HCOO⁻, OCN⁻, H₂CO, HCOOH, CH₃CH₂OH, CH₃CHO, CH₃OCHO, CH₃COOH

W. R. M. Rocha^{1,2}, E. F. van Dishoeck^{2,3}, M. E. Ressler⁴, M. L. van Gelder², K. Slavicinska^{1,2}, N. G. C. Brunken², H. Linnartz¹, T. P. Ray⁵, H. Beuther⁶, A. Caratti o Garatti⁷, V. Geers⁸, P. J. Kavanagh⁹, P. D. Klaassen⁸, K. Justannont¹⁰, Y. Chen², L. Francis², C. Gieser³, G. Perotti⁶, Ł. Tychoniec¹¹, M. Barsony¹², L. Majumdar^{13,14}, V. J. M. le Gouellec¹⁵, L. E. U. Chu¹⁵, B. W. P. Lew¹⁶, Th. Henning⁶, and G. Wright⁸

(Affiliations can be found after the references)

Received xxxx; accepted yyyy

ABSTRACT

Context. Complex organic molecules (COMs) are ubiquitously detected in the gas phase and are thought to be mostly formed on icy grains. Nevertheless, no unambiguous detection of COMs larger than CH₃OH in ices has been reported so far, but exploring this matter in more detail has become possible with the unprecedented possibilities offered by the *James Webb* Space Telescope (JWST) within the infrared (IR) spectral range with its very high sensitivity and spectral resolution in the critical 5–10 μm range, the fingerprint region of oxygen-bearing COMs.

Aims. In the program JWST Observations of Young protoStars (JOYS+), more than 30 protostars are being observed with the Medium Resolution Spectrograph (MRS) of the Mid-IR Instrument (MIRI). The goal of this study is to comprehensively explore the COMs ice signatures in one low- and one high-mass protostar, NGC 1333 IRAS 2A and IRAS 23385+6053, respectively.

Methods. We perform global continuum and silicate subtractions of the MIRI-MRS spectra, followed by a local continuum subtraction in optical depth scale in the range around 6.8 and 8.6 μm, the ice COM fingerprint region. Different choices of local continuum and silicate subtraction were explored. Next, we fit observational data with a large sample of available IR laboratory ice spectra. We use the ENIGMA fitting tool, a genetic algorithm-based code that not only finds the best fit between the lab data and the observations but also performs statistical analysis of the solutions, such as deriving the confidence intervals and quantifying fit degeneracy.

Results. We report the best fits for the spectral ranges between 6.8 and 8.6 μm in NGC 1333 IRAS 2A and IRAS 23385+6053, originating from simple molecules and COMs, as well as negative ions. In total, 10 chemical species are needed to reproduce the astronomical data. The strongest feature in this range (7.7 μm) is dominated by CH₄ and has contributions of SO₂ and OCN⁻. Our results indicate that the 7.2 and 7.4 μm bands are mostly dominated by HCOO⁻. We also find statistically robust detections of COMs based on multiple bands, most notably CH₃CHO, CH₃CH₂OH, and CH₃OCHO. The likely detection of CH₃COOH is also reported. Based on the ice column density ratios between CH₃CH₂OH and CH₃CHO of NGC 1333 IRAS 2A and IRAS 23385+6053, we find compelling evidence that these COMs are formed on icy grains. Finally, the derived ice abundances for NGC 1333 IRAS 2A correlate well with those in comet 67P/GC within a factor of 5.

Conclusions. Based on the high-quality JWST (MIRI-MRS) spectra, we conclude that COMs are present in interstellar ices, thus providing additional proof for a solid-state origin of these species in star-forming regions. In addition, the good correlation between the ice abundances in comet 67P and NGC 1333 IRAS 2A is fully in line with the idea that cometary COMs can be significantly inherited from the early protostellar phases.

Key words. Astrochemistry – ISM: molecules – solid state: volatile

1. Introduction

Complex organic molecules (COMs) are molecules with 6 atoms or more and have at least one atom of Carbon (Herbst & van Dishoeck 2009). They are intrinsically important to comprehend the chemical complexity developed in star-forming regions since these materials are the feedstock for future exoplanetary systems. Once available in primitive planetary systems, this material can potentially promote the habitability of planets. An important question for delivering organic material to new solar systems is whether the molecules are in the gas phase or in ices as part of icy dust grains. Only in the latter case water and organic molecules are expected to be effectively delivered to terrestrial planets as discussed by Morbidelli et al. (2012); van Dishoeck et al. (2014); Morbidelli et al. (2018); O’Brien et al. (2018); van Dishoeck

et al. (2021) and the lower UV photodestruction cross-section of those molecules in the solid-phase (e.g., Öberg 2016). Yet, very little information is available about these organic molecules in ices. The *James Webb* Space Telescope (JWST) provides a tool to change the situation by observing ice features during the early protostellar phases with higher resolution and sensitivity than before.

Gas-phase observations have been exceptionally successful in probing the chemical complexity towards low-mass and massive young stellar objects (LYSOs and MYSOs, respectively) as shown in the literature (e.g., Blake et al. 1987; Cazaux et al. 2003; Bergner et al. 2017; Manigand et al. 2020; Belloche et al. 2020; van Gelder et al. 2020; Jørgensen et al. 2020; Nazari et al. 2021; Gieser et al. 2021), and the observations and abundances of many COMs are summarized in the review by Jørgensen

et al. (2020). The current consensus is that COMs are efficiently formed in the solid phase, and desorb into the gas phase by thermal and non-thermal mechanisms. Nevertheless, methanol (CH_3OH) is the only COM securely identified in the solid phase based on the infrared (IR) spectra from the United Kingdom Infrared Telescope (UKIRT; Grim et al. 1991; Skinner et al. 1992; Dartois et al. 1999), Infrared Space Observatory (*ISO*, e.g., Gibb et al. 2004), Very Large Telescope (Pontoppidan et al. 2004; Dartois et al. 2003; Thi et al. 2006), Infrared Telescopic Facility (Chu et al. 2020), *Spitzer* Space Telescope (Boogert et al. 2008; Bottinelli et al. 2010), AKARI (Shimonishi et al. 2010; Perotti et al. 2021), and recently with JWST (e.g., Yang et al. 2022; McClure et al. 2023). Larger COMs compared to CH_3OH have been tentatively identified based on only a single infrared (IR) vibrational mode or were proposed as possible carriers for yet unidentified features, such as ethanol - $\text{CH}_3\text{CH}_2\text{OH}$ and acetaldehyde - CH_3CHO (Schutte et al. 1999; Öberg et al. 2011; Terwisscha van Scheltinga et al. 2018). These two COMs were also tentatively identified in the JWST high spectral resolution and sensitivity spectrum of IRAS 15398–3359 (Yang et al. 2022) and towards two background stars (McClure et al. 2023), although at lower spectral resolution. Other upper limits have been determined for methyl formate (CH_3OCHO ; Terwisscha van Scheltinga et al. 2021), methylamine (CH_3NH_2 ; Rachid et al. 2021), methyl cyanide (CH_3CN ; Rachid et al. 2022), and formamide (NH_2CHO ; Schutte et al. 1999; Slavicinska et al. 2023). Boudin et al. (1998) also estimated upper limits for molecules such as ethane (C_2H_6), acetylene (C_2H_2), hydrazine (N_2H_4), hydrogen peroxide (H_2O_2) and the hydrozonium ion (N_2H_5^+).

In parallel, gas phase formation of COMs through ion-molecule reactions has been proposed as well (e.g., Balucani et al. 2015; Skouteris et al. 2018; Vazart et al. 2022). The recent detection in a protoplanetary disk of gas phase CH_3^+ (Berné et al. 2023), an important intermediate in such reactions, supports the idea that COM formation is not exclusively realized on icy grains. This study focuses on the latter.

In the mid-IR spectral range, icy COMs have multiple absorption features, at for example, $\sim 5.8 \mu\text{m}$, $6.8\text{--}7.0 \mu\text{m}$, $7.2 \mu\text{m}$, $7.4 \mu\text{m}$, $\sim 8 \mu\text{m}$, and $\sim 9.5\text{--}9.8 \mu\text{m}$. However, due to the spectral overlap with the features of other molecules (including dust grain species), the bands at 7.2 and $7.4 \mu\text{m}$ bands have been considered the main fingerprint of COMs (e.g., Schutte et al. 1999; Öberg et al. 2011; Terwisscha van Scheltinga et al. 2018), which is also emphasized in this work. For example, Schutte et al. (1999) proposed that the $7.2 \mu\text{m}$ band can be due to HCOOH (formic acid) ice, notably, the O–H bending mode of the carboxylic functional group and the C–H bending mode. In particular, Bisschop et al. (2007) finds a good match between the $7.2 \mu\text{m}$ band of the high-mass protostar W33A and the tertiary mixture $\text{HCOOH}:\text{CH}_3\text{OH}:\text{H}_2\text{O}$. The assumption that HCOOH would be the only carrier of the $7.2 \mu\text{m}$ band would lead to an unrealistic high solid-state abundance which is not in line with gas-phase observations (Bisschop et al. 2007). Nevertheless, this is not an argument for excluding HCOOH as a component of the interstellar ice, because it is also visible at other wavelengths (e.g., $5.8 \mu\text{m}$). Instead, this indicates that HCOOH is not the main carrier of the $7.2 \mu\text{m}$ band. As an alternative, Boudin et al. (1998) and Öberg et al. (2011) propose that the deformation mode in the methyl functional group (CH_3) of ethanol can be the carrier for the $7.2 \mu\text{m}$ band. In the case of the $7.4 \mu\text{m}$ absorption feature, Schutte et al. (1999) propose that the formate ion (HCOO^-) and acetaldehyde can be the carriers of this band. In all cases, these tentative assignments need a convincing profile fit with laboratory data to confirm these chemical species as carriers of

those bands. These fits must also consider a larger spectral range around the $7\text{--}8 \mu\text{m}$ range where other typical vibrational modes of COMs are also detectable.

In addition to COMs, ions such as OCN^- (cyanate ion), HCOO^- and NH_4^+ have been proposed to be present in interstellar ices mostly as part of salts produced by acid-base reactions (e.g., Geballe 1984; Grim & Greenberg 1987; Schutte et al. 1999; Schutte & Khanna 2003; Gálvez et al. 2010; Maté et al. 2012; Moreno et al. 2013; Bergner et al. 2016; Kruczkiewicz et al. 2021). The presence of OCN^- in ice mantles can be considered a secure detection based on comprehensive laboratory experiments and extensive analysis towards several protostars (e.g., Geballe 1984; van Broekhuizen et al. 2004) and towards background stars (McClure et al. 2023), and the good correlation between gas-phase abundances of HNCO and OCN^- ice (Öberg et al. 2009a). In the case of HCOO^- and NH_4^+ , Boogert et al. (2015) argue that a convincing profile fit is still needed to firmly confirm the presence of these ions in ice mantles. If present in interstellar ices, these ions are likely part of refractory salts such as ammonium formate ($\text{NH}_4^+\text{HCOO}^-$) studied in the laboratory and found in comet 67P/G-C (e.g., Poch et al. 2020). In addition, the presence of OCN^- and HNCO in ices has a strong astrobiological appeal: HNCO participates as a peptide bond between two single amino acids (e.g., Fedoseev et al. 2015; Quénard et al. 2018; Colzi et al. 2021; Ligterink et al. 2022).

In this work, we address the presence of simple molecules, COMs, and ions in protostellar ices using newly observed JWST spectra of two protostars with the Medium Resolution Spectrograph (MRS) of the Mid-Infrared Instrument (MIRI) under the JOYS+ program¹ (JWST Observations of Young protoStars; van Dishoeck et al. 2023). The first source is a high-mass ($\sim 220 M_\odot$; $d = 4.9$ kpc; Molinari et al. 1998, 2008) star-forming region called IRAS 23885+6053 (hereafter IRAS 23385). This cluster is highly embedded in its natal molecular cloud and shows maser emissions of H_2O (Casoli et al. 1986) and CH_3OH (Kurtz et al. 2004), characteristic of shocks. *Spitzer* observations of this source reveal extended emission of polycyclic aromatic hydrocarbons (PAHs) that are excited in this region by surrounding sources with spectral types between B1.5 and B5 (Molinari et al. 2008). NOEMA (Northern Extended Millimeter Array) observations of this source show a variety of gas-phase molecules, such as OCS , H_2CO , HNCO , CH_3OH and CH_3CN (Cesaroni et al. 2019). No other gas-phase COM have been detected in this region apart from CH_3OH and CH_3CN (Gieser et al. 2021). Recently, Beuther et al. (2023) present the rich MIRI-MRS spectrum of IRAS 23885, with focus on the outflow tracers $\text{H}_2(0\text{--}0) \text{S}(7)$, $[\text{Fe II}] (^4\text{F}_{9/2} - ^6\text{D}_{9/2})$ and $[\text{Ne II}] (^2\text{P}_{1/2} - ^2\text{P}_{3/2})$, and an accretion tracer, the Humphreys α $\text{HI}(7\text{--}6)$ emission line detected at a $3\text{--}4\sigma$ level. A multiwavelength analysis using MIRI and NOEMA data provides information about the hot, warm and cold molecular components in IRAS 23385 (Gieser et al. 2023). In addition, Francis et al. (submitted) analyse the compact gaseous molecular emission in IRAS 23385.

The second source targeted in this work is the low-mass Class 0 protostar NGC 1333 IRAS 2A (hereafter IRAS 2A) (e.g., Jørgensen et al. 2005; Brinch et al. 2009), a well-studied hot-corino located in the Perseus complex, specifically in the NGC 1333 molecular cloud, at a distance of 299 ± 3 pc (Ortiz-León et al. 2018; Zucker et al. 2018). This is a protobinary system (Looney et al. 2000; Reipurth et al. 2002), hosting two collimated jets (Sandell et al. 1994; Tobin et al. 2015). IRAS 2A is also a source where several gas-phase COMs are identified (e.g.,

¹ <https://miri.strw.leidenuniv.nl/>

156 Bottinelli et al. 2007), including glycolaldehyde (HCOCH₂OH; 216
157 Coutens et al. 2015; Taquet et al. 2015; De Simone et al. 2017), 217
158 an important sugar molecule that participates in the formation of 218
159 ribose, a component of the ribonucleic acid (RNA). 219

160 Compared to the *Spitzer* Space Telescope, which had enough 220
161 sensitivity to observe the brighter low-mass protostars but low 221
162 spectral resolution, the JWST (MIRI/MRS) observations are 222
163 qualitatively superior. The MIRI-MRS resolving power (R) 223
164 around the 7–8 μm region, where COMs signatures are present, 224
165 is $R = 3500\text{--}4000$ (Labiano et al. 2021), whereas the *Spitzer* In- 225
166 frared Spectrograph (IRS) offered a resolving power of only $R =$ 226
167 60. Yang et al. (2022) demonstrate for IRAS 15398–3359 that 227
168 the ice absorption features around the 7–8 μm are significantly 228
169 stronger with much higher S/N profiles due to better resolution 229
170 and sensitivity in the MIRI/MRS compared with *Spitzer*/IRS. 230

171 An important disclaimer to make is that although this pa- 231
172 per presents JWST/MIRI spectra of a high- and low-mass proto- 232
173 star, this is not a comparative work of ices in those objects. In- 233
174 stead, we show data from two sources that were observed first in 234
175 our programs. A suitable comparison of ice features in different 235
176 sources needs a more extended list of protostars and will be per- 236
177 formed in future work. This paper is structured as follows: Sec- 237
178 tion 2 introduces the JWST/MIRI observations of IRAS 23385 238
179 and IRAS 2A, the method for the data reduction, and the back- 239
180 ground subtraction. In Section 3 we describe how the ice bands 240
181 are isolated, the fitting procedure, the method for quantifying 241
182 the fitting degeneracy, and which criteria we use for a firm de- 242
183 tection. We focus in this paper on the 6.8–8.6 μm range, and 243
184 therefore molecules with vibrational modes outside this interval 244
185 are not discussed (e.g., H₂O, CO₂, NH₄⁺). The results are shown 245
186 in Section 4, which includes the spectral fits, degeneracy analy- 246
187 sis and ice column densities. The discussions of these results are 247
188 presented in Section 5, outlining the important insights from the 248
189 JWST observations, and how the ice COMs abundances corre- 249
190 late between the low- and high-mass protostar, as well as with the 250
191 comet 67P/G-C. The conclusions are summarized in Section 6. 251

192 Below we provide some guidelines for a selective reading of 252
193 this paper: 253

- 194 – JWST data treatment and subtractions performed on the 254
195 data: Sections 2.1, 2.2, 3.1, 3.2, 3.3. Appendices A and B. 255
- 196 256
- 197 – Fitting methodology and results: Sections 3.4 and 4.1. 257
198 Appendices C and G. 258
- 199 259
- 200 – Statistical analysis and degeneracy: Sections 3.5 and 4.2. 260
201 Appendices H, I and J. 261
- 202 262
- 203 – Identification criteria and suggestions for future works: 263
204 Sections 3.6 and 3.7. Appendices E and F. 264
- 205 265
- 206 – Ice column densities, abundances, and correlations: Sec- 266
207 tions 4.3, 4.4, 4.5, 5.1.3, and 5.3. Appendix D and K. 267
- 208 268
- 209 – Ice chemical complexity discussions: Sections 4.1, 5.1 and 269
210 5.2. Appendix L. 270

211 2. Observations 272

212 2.1. Data reduction 273

213 IRAS 23385+6053 (R.A. 23^h40^m54.5^s, Dec. +61^d10^m28^s) and 274
214 NGC 1333 IRAS 2A (R.A. 03^h28^m55.57^s, Dec. +31^d14^m36.97^s) 275
215 were observed with JWST as part of the guaranteed observation 276

216 time (GTO) 1290 (P.I. E. F. van Dishoeck) and 1236 (P.I. M. 217
218 Ressler), respectively. 219

220 All data presented in this paper were taken with the Mid- 221
222 InfraRed Instrument (MIRI; Rieke et al. 2015; Wright et al. 223
224 2015, 2023) in the Medium Resolution Mode (MRS; Wells 225
226 et al. 2015; Labiano et al. 2021; Argyriou et al. 2023). For 227
228 IRAS 23385, the observation was done in 2-point dither mode 229
230 in a 4-point mosaic surrounding the central protostellar cluster. 231
232 For IRAS2A, the observation consists of a single pointing on the 233
234 protostellar binary in 2-point dither mode. For both targets, also 235
236 dedicated background observations were performed (no dither 237
238 for IRAS 23385, 2-point dither for IRAS 2A). For both targets, 239
240 all three gratings (A, B, C) were used, providing the full wave- 241
242 length coverage of MIRI (4.9–28 μm). All data were taken using 243
244 the FASTR1 readout mode. The integration time in each grating 245
246 was 200 s and 111 s for IRAS 23385 (per pointing in the mosaic) 247
248 and IRAS 2A, respectively. 249

250 The data were processed through all three stages of 251
252 the JWST calibration pipeline (Bushouse et al. 2022), using 253
254 the reference context `jwst_1017.pmap` (IRAS 23385) 255
256 and `jwst_0994.pmap` (IRAS2A) of the JWST Calibra- 257
258 tion Reference Data System (CRDS; Greenfield & Miller 259
260 2016). The raw `uncal` data were first processed through 261
262 the `Detector1Pipeline` of the pipeline, followed by the 263
264 `Spec2Pipeline`. In the latter step, the data are corrected for 265
266 fringes using the fringe flat for extended sources (Mueller et al. 266
267 in prep.), followed by applying a residual fringe correction (Ka- 267
268 vanagh et al. in prep.). Moreover, in the case of IRAS2A, the 268
269 telescope background was subtracted in this step using the dedi- 269
270 cated background observation. However, the background obser- 270
271 vation of IRAS 23385 includes significant astronomical back- 271
272 ground emission across all wavelengths, as well as strong emis- 272
273 sion of PAHs, and could thus not be used to subtract the tele- 273
274 scope background. The background estimation and subtraction 274
275 procedure for IRAS 23385 is further discussed in Sect. 2.2. 275
276 As mentioned in Beuther et al. (2023), an astrometric correc- 276
277 tion was applied for IRAS 23385, i.e., 1.6077'' in Right As- 277
278 cension and 0.3485'' in Declination based on identified GAIA- 278
279 DR3 stars in the parallel images. No such correction was neces- 279
sary for IRAS2A. The data were further processed with the 280
`Spec3Pipeline` of the pipeline which produces cubes of all 12 281
subbands. In this step, both the master background and outlier 282
rejection routines were switched off. 283

284 The observation of IRAS 23385+6053 reveals two mid- 285
286 infrared continuum sources (Beuther et al. 2023) that are re- 286
287 solved at shorter wavelengths (channels 1 and 2, $\lambda < 12 \mu\text{m}$), 287
288 but which start to become marginally resolved at longer wave- 288
289 lengths (channel 3, $12 \mu\text{m} < \lambda < 17 \mu\text{m}$) and are completely 289
290 unresolved at the longest wavelengths (channel 4, $\lambda > 17 \mu\text{m}$). 290
291 The spectrum is therefore extracted from a large aperture of 2.5'' 291
292 in diameter (which does not increase with wavelength) centred 292
293 in between the two sources (R.A. (J2000) 23^h40^m54.49^s, Dec 293
(J2000) 61^d10^m27.40^s) to encompass the flux of both sources 294
295 across the full wavelength range. The estimated 1σ rms increases 294
296 from about 0.4 mJy below 20 μm to a few mJy at the longest 295
297 wavelengths. 296

298 In the observation of IRAS2A, only continuum emission re- 299
299 lated to the primary component of the binary is detected. The 299
300 spectrum is therefore extracted from the peak of the continuum 300
301 emission at 5.5 μm (R.A. (J2000) 03^h28^m55.57^s, Dec (J2000) 301
302 31^d14^m36.76^s). We assume that any contribution of the sec- 302
303 ondary component to the spectrum is negligible. The diameter 303
304 of the aperture was set to $4 \times 1.22\lambda/D$ to capture as much of the 304
305 source flux as possible without including too much noise. The 305

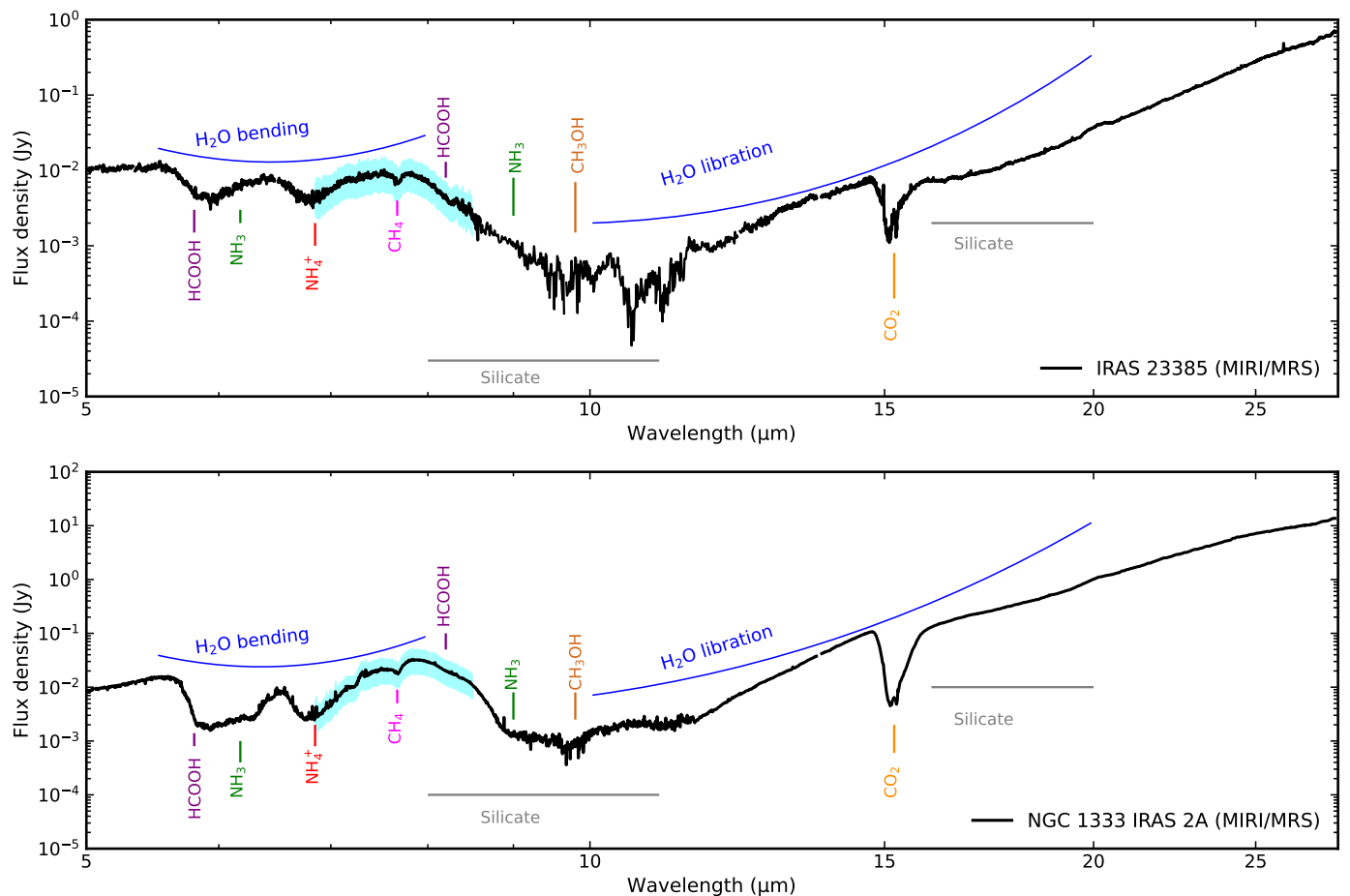


Fig. 1. MIRI MRS spectrum of the high-mass protostar IRAS 23385+6053 (top) and the low-mass protostar NGC 1333 IRAS 2A (bottom). Strong gas-phase emission lines are masked in both spectra. The assignments for the absorption bands are given and differentiated by the colours. The shaded cyan area indicates the “COMs region” that is studied in this work.

280 estimated 1σ rms is about 0.4 mJy below 15 μ m and increases
 281 to a few mJy at 19 μ m and > 10 mJy longwards of 22 μ m.

282 Figure 1 (top) shows the MIRI/MRS spectra of
 283 IRAS 23385+6053 (Beuther et al. 2023) and Figure 1 (bottom)
 284 shows IRAS 2A covering the range between 5 and 28 μ m, and
 285 with a resolving power of 4000–1500 (Labiano et al. 2021).
 286 The spectral absorption features are associated with different
 287 ice molecules where the principal molecules are labelled in this
 288 figure, and those in the cyan region will be further discussed in
 289 Section 4. We highlight the broad feature of H₂O covering the
 290 range between 5.5 and 8 μ m (bending mode) and between 10
 291 and 20 μ m (libration mode). HCOOH shows prominent features
 292 at 5.8 and 8.2 μ m which can be distinguished in these sources.
 293 Small features attributed to NH₃ (ammonia), CH₄ (methane) and
 294 NH₄⁺ (ammonium) are also seen in this spectrum. Silicates
 295 are the other main solid-state species contributing to the absorp-
 296 tion bands around 9.8 and 18 μ m. In addition to the absorp-
 297 tion features, the spectra of IRAS 23385 and IRAS 2A have various
 298 narrow emission lines which are masked in this work since it is
 299 focused on ice absorption features. We also point out that the
 300 IRAS 23385 spectrum is binned by a factor of four between 8.6
 301 and 12 μ m because of the saturated silicate band, and IRAS 2A
 302 spectrum is binned by a factor of two in the entire MIRI-MRS
 303 range.

2.2. Background subtraction for IRAS 23385+6053

304

In the case of IRAS 23385+6053, the telescope and other back- 305
 grounds could not be subtracted in either the Spec2Pipeline 306
 or Spec3Pipeline since this results in negative fluxes due to 307
 significant astronomical emission in the dedicated background 308
 observation. It is, however, crucial to remove the telescope back- 309
 ground from our observations to derive accurate ice column den- 310
 sities. The background was therefore estimated by extracting a 311
 spectrum from the science observation off-source from the main 312
 infrared continuum sources at the position within the IFU (In- 313
 tegral Field Unit) where the background flux was the lowest 314
 (R.A. (J2000) 23^h40^m54.15^s, Dec (J2000) 61^d10^m26.96^s) using 315
 the same aperture size as used for extracting the science data 316
 (2.5’). The background subtraction also results in the subtrac- 317
 tion of the 8.6 μ m and 11.3 μ m PAH features, the emission 318
 of which was about equally strong in the background-position 319
 as at the source position. However, a possible under- or over- 320
 subtraction of PAH emission does not alter the results in this 321
 work since the PAH bands are broader than the ice bands at the 322
 wavelengths targeted in this paper. The background subtracted 323
 spectrum of IRAS 23385+6053 is shown in the top panel of 324
 Fig. 1. The numerous strong gas-phase emission lines have been 325
 masked in this version of the spectrum. The unmasked version 326
 is available in Beuther et al. (2023) and van Gelder et al. (2023) 327
 for IRAS 23385 and IRAS 2A, respectively. 328

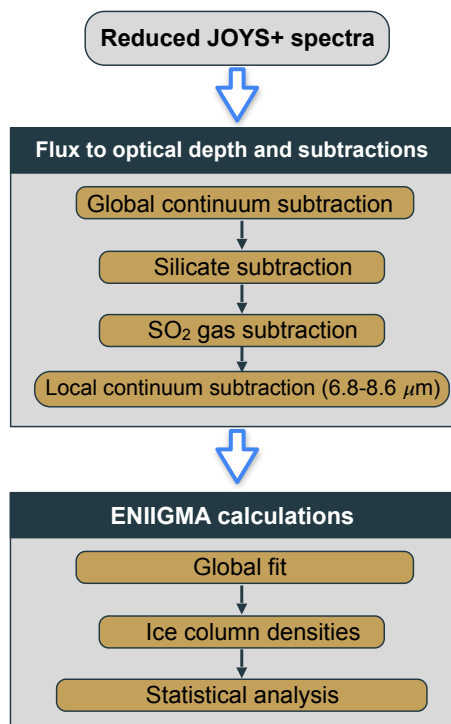


Fig. 2. Summary of the methodology used in this paper.

3. Methodology

In this section, we provide information about the methods used to trace and subtract the dust continuum profile, the procedure to remove the silicate bands, and finally, the technique used to fit and identify the ice absorption bands. The focus of this paper is on the 6.8–8.6 μm range as indicated in Figure 1, but the entire MIRI spectrum has to be taken into account for the continuum fitting. For clarity reasons, we summarize the methodology steps in a flowchart shown in Figure 2.

3.1. Continuum subtraction and silicate removal

The spectral energy distributions (SEDs) of IRAS 23385+6053 and IRAS 2A show an increasing slope towards long wavelengths which is typical of embedded protostars. Such SED shapes are also observed towards many high-mass protostars (e.g., Orion BN, Orion IRC2; Gibb et al. 2004) and low-mass protostars (e.g., CrA IRAS32, IRAS 03301+311 and L1448 IRS1 Boogert et al. 2008). The shorter wavelength SED is composed of contributions by warm dust at a range of temperatures, whereas the increase in flux beyond 20 μm is due to the coldest envelope material (Adams et al. 1987). Determining the continuum of these protostars in the mid-IR range is not trivial because of the broad absorption bands in this spectral region. Often, a guided polynomial function is used (e.g., Boogert et al. 2008) to trace the continuum SED. In this work, a third-order polynomial function is used to fit selected points between 5.3–5.5 and 27–28.5 μm where there is little or no overlap exists with ice absorption bands. An additional point was added at 7.5 μm **slightly above the observational data to avoid unrealistic inflexions in the low-order polynomial that would lead to an unphysical continuum. The reason for using this point is to account for known broad absorption features in this range**, for example, the blue wing of the 9.8 μm silicate feature, the H₂O ice broad bending mode, part of the C5 component proposed in Boogert

et al. (2008), and some of the complex molecules targeted in this paper. In this case, the observed flux itself at 7.5 μm is not suitable to be used as an anchor point. Uncertainties in the position of this guiding point do not affect the conclusions of this work. Figures 3a and 3b, show the polynomial fits used for IRAS 23385 and IRAS 2A, respectively, and the emission lines are masked. Note that there is significant absorption with respect to this continuum over the entire wavelength range in both sources.

Once the continuum SED is determined, we convert the MIRI-MRS spectra of the two protostars to an optical depth scale, as shown in Figures 3c and 3d by using the equation below:

$$\tau_{\lambda} = -\ln\left(\frac{F_{\lambda}^{\text{source}}}{F_{\lambda}^{\text{cont}}}\right), \quad (1)$$

where $F_{\lambda}^{\text{source}}$ is the source spectrum and $F_{\lambda}^{\text{cont}}$ is the continuum SED.

Among the absorption bands seen in both spectra, silicates significantly contribute to the bands around 9.8 μm and 18 μm . Since the profile at 9.8 μm is positioned on top of a few ice bands, we perform a silicate removal to analyse the absorption features related to icy molecules. Often, the silicate profile observed towards the galactic centre source, GCS 3, is used to remove the silicate profile of other protostars (Boogert et al. 2008; Bottinelli et al. 2010). However, this method is not used in this work because the shape of the silicate features towards IRAS 23385+6053 and IRAS 2A are broader than GCS 3 as shown in Figures A.1 and A.2 (Appendix A), and would lead to a spurious absorption profile around 8.6 μm after removing the silicate. As an alternative method, we combine two types of silicate to match the band at 9.8 μm following the approach described in Boogert et al. (2011); Poteet et al. (2015); Do-Duy et al. (2020) and McClure et al. (2023). Specifically, we use a mixture of amorphous pyroxene ($\text{Mg}_{0.5}\text{Fe}_{0.5}\text{SiO}_3$) and olivine (MgFeSiO_4) from Dorschner et al. (1995).

We use the `optool` code (Dominik et al. 2021) to generate optical depth spectra of the two silicate types. Briefly, we assume a mixture of silicate and carbon, typical chemical species of interstellar grains, with volume fractions of 87% and 13%, for IRAS 23385 and 82% and 18% for IRAS 2A, as typically used in protostar models. The variation in the fraction of carbon in the models allows us to fit the 9.8 μm and 18 μm bands simultaneously because a higher volume fraction of amorphous carbon reduces the intensities of the silicate bands. Different carbon fractions have been used in the literature to create dust models, for example, 30% (Weingartner & Draine 2001), and 15% (Pontoppidan et al. 2005; Woitke et al. 2016). For the dust models, we assume a power-law size distribution with an exponent of -3.5 and grain sizes ranging from 0.1 to 1 μm . We adopt a distribution of hollow spheres (DHS; Min et al. 2005) to model the silicate band, as this approach mimics irregular geometries of the dust grains. The generated silicates are combined linearly to match the 18 μm band without exceeding the absorption at 9.8 μm and the blue silicate wing around 8.5 μm as shown in Figure 3c and 3d.

The optical depth ratio between the 9.8 and 18 μm silicate features is equal to 2.7 for IRAS 23385 and 2.95 for IRAS 2A. These values are higher compared to the silicates found in the diffuse interstellar medium, which ranges from 1.4 to 2.0 (Chiar & Tielens 2006). It is likely that grain growth plays a role in this case, but a detailed study of this process is beyond the scope of this work. The silicate-removed spectra of IRAS 23385

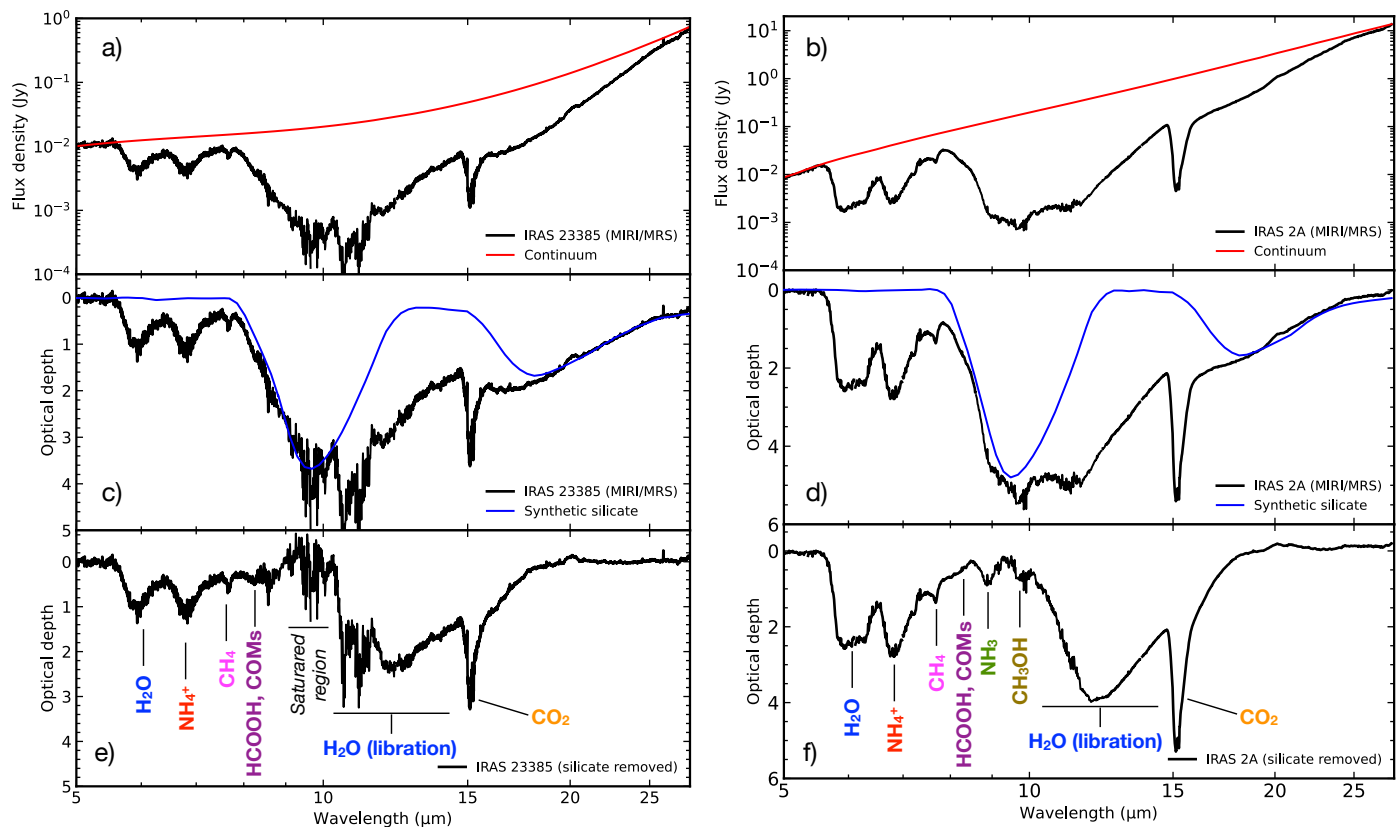


Fig. 3. Continuum (a, b) and silicate subtraction (c, d) steps in IRAS 23385 (left) and IRAS 2A (right). The spectrum of IRAS 23385 is binned by a factor of two between 9 and 11 μm due to the saturated silicate profile. A third-order polynomial function is used to trace the continuum, and the silicate profile is a combination of two laboratory silicate spectra (olivine and pyroxene). Panels e and f show the silicate subtracted spectra of both protostars, with major features labelled.

and IRAS 2A are presented in Figures 3e and 3f. By removing the silicate bands, the H_2O ice libration band is revealed around 12 μm . One can also see the ammonia umbrella mode at 9.0 μm and the methanol C-O stretch mode at 9.8 μm in IRAS 2A (Fig. 3f), but not in IRAS 23385 because of the saturation due to the silicate feature, as well as the higher noise level.

For completeness, we show in Appendix B the silicate subtraction using different silicates for IRAS 2A, the source with high signal-to-noise ratio (S/N). Those spectra are scaled to an optical depth of $\tau = 4.9$, which is the same as in the synthetic silicate fit (top panel of Figure B.1). The subtracted spectra are shown in the bottom panel. It is clear that the synthetic silicate and the MgSiO_3 model taken from Poteet et al. (2015) show very similar profiles. On the other hand, the use of the GCS 3 silicate leads to an unrealistic absorption excess. Finally, it is worth mentioning that silica (SiO_2) has a blue shoulder at 8.6 μm and a peak at 9 μm . However, the presence of silica is associated with other materials such as enstatite and forsterite whose spectral features are not seen in the sources addressed in this paper. For the different silicates considered in this paper, there are no relevant differences in the spectral shapes between 7.8 and 8.5 μm .

3.2. SO_2 gas emission subtraction

In the spectrum of IRAS 2A, clear molecular emission is superimposed on the ice absorption features between ~ 7.25 μm and ~ 7.45 μm , see Fig. 4. This emission was recently found to originate from warm gas-phase SO_2 (van Gelder et al. 2023). In order to accurately determine the contribution of ices in this

wavelength range, the gas-phase emission lines of SO_2 (ν_3) have to be subtracted from the spectrum. This was achieved by subtracting the best-fit gas-phase emission line model of SO_2 , which was recently derived by van Gelder et al. (2023). This model is very well constrained by the R branch lines at 7.3 μm .

The SO_2 emission subtracted spectrum is also presented in Figure 4 as the orange line and clearly reveals an ice absorption feature around 7.4 μm that was hidden by the SO_2 emission. The SO_2 emission is slightly over-subtracted around 7.35 μm (i.e. at the Q-branch) but this does not hamper the analysis of the ice bands since this residual is much more narrow than typical ice absorption bands.

3.3. Isolating ice features between 6.85 and 8.6 μm

Weak absorption features have been measured in the laboratory covering the range between 6.85 and 8.6 μm (e.g., Lacy et al. 1991; Schutte et al. 1999; Öberg et al. 2011), and Terwisscha van Scheltinga et al. (2018), which are compared with observational spectra of massive protostars, by Boogert et al. (2008); Öberg et al. (2011), low-mass protostars (e.g., Zasowski et al. 2009; Yang et al. 2022) and background stars (McClure et al. 2023). Most notable are the absorption features around 7.2 and 7.4 μm . To isolate these bands, previous works used a polynomial fit on the flux scale data to trace a local continuum starting around 7.0–7.14 μm and finishing around 7.8–8.0 μm (e.g., Schutte et al. 1999). This approach isolates the 7.2 and 7.4 μm features but excludes potential absorption features around 7 μm

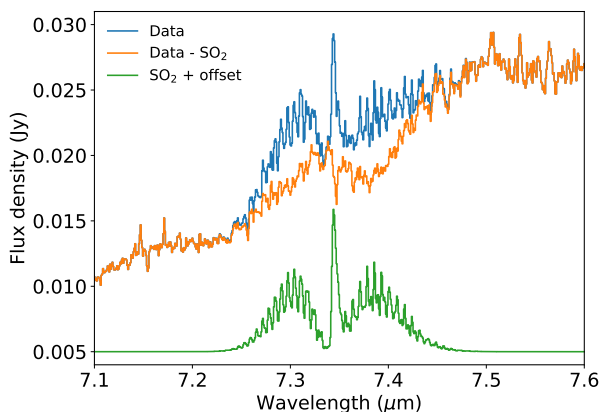


Fig. 4. The observed spectrum of IRAS 2A (blue) surrounding the 7.2 μm and 7.4 μm ice absorption features with SO_2 (ν_3) emission. The best-fit SO_2 model of van Gelder et al. (2023) is presented in green and the SO_2 subtracted spectrum of IRAS2A is shown in orange. Subtracting the SO_2 emission clearly reveals the 7.4 μm absorption feature.

475 and at wavelengths long-wards of 7.8 μm where C–H and C–O
476 absorption features of many possible molecules contribute.

477 In this work, we isolate the 7.2 and 7.4 μm features using
478 a third-order polynomial function, and following a slightly dif-
479 ferent approach. First, instead of using the spectrum on the flux
480 scale, we perform the polynomial fit on the optical depth scale
481 after removing the silicate absorption. The strong silicate band
482 makes it difficult to observe small features such as those due
483 to COMs. Second, we use guiding points fitted by a third-order
484 polynomial function, as shown in the left panels of Figure 5.
485 This additional continuum represents blended absorption pro-
486 files from the broad H_2O ice bending mode, the red wing of the
487 NH_4^+ cation, and the C5 component proposed by Boogert
488 et al. (2008). Another small contribution from the O–H bending
489 mode of CH_3OH ice is also considered in this step. The points
490 used for IRAS 23385 are at 6.8, 7.2, 7.7 and 8.5 μm and at 6.8,
491 7.3, 7.5, 9.4 and 10 μm for IRAS 2A. The positions of the guid-
492 ing points are distinct because of the differences in the absorp-
493 tion profiles of the two sources. In order to account for possible
494 C–H absorption bands, the first point at 6.8 μm is chosen to be
495 marginally above the wing of the strong 6.85 μm feature. The
496 points long-wards of 7.8 μm are selected where we expect no
497 or weak ice absorption, to account for the C–O features. In the
498 case of IRAS 2A, we use points at 9.4 and 10.0 μm because of
499 the clear absorption profiles at 9 and 9.8 μm .

500 After subtracting the local continuum fit, we isolate the ice
501 features in the range between 6.8 and 8.5 μm as shown in the
502 right panels of Figure 5. In these figures, one can see absorp-
503 tion bands at 7, 7.2, 7.4, 7.5–7.8 and 8.2 μm that are fitted and
504 discussed in Sections 4 and 5, respectively. Notably, the 8.2 μm
505 band of IRAS 23385 seems broad and asymmetric, whereas in
506 IRAS 2A the same band seems broad, weaker and symmetric.
507 The band around 7.7 μm has a prominent blue shoulder in both
508 sources, reflecting the interaction with other neighbouring chem-
509 ical species.

510 3.4. Fits and laboratory data

511 Since molecules have multiple functional groups, performing si-
512 multaneous fits at different wavelengths supports secure detec-
513 tion. Additionally, some molecules are expected to absorb in
514 the wavelength range targeted in this paper, such as CH_4 , SO_2 ,

HCOOH , CH_3CHO and $\text{CH}_3\text{CH}_2\text{OH}$ (e.g., Schutte et al. 1999; 515
Bisschop et al. 2007; Öberg et al. 2008), which are used as start- 516
ing point in the MIRI spectral ice decomposition. We fit the re- 517
gion between 6.8 and 8.6 μm of IRAS 2A and IRAS 23385 using 518
the ENIIGMA fitting tool (Rocha et al. 2021). This code searches 519
for the global minimum solution that fits the observations by 520
performing a linear combination of laboratory ice data. The ge- 521
netic algorithm approach benefits from a simple fitness function 522
(Baek et al. 2000), and here we use the root-mean-square error 523
(RMSE) given by the equation below: 524

$$RMSE = \sqrt{\frac{1}{n} \sum_{i=0}^{n-1} \left(\tau_{\nu,i}^{\text{obs}} - \sum_{j=0}^{m-1} w_j \tau_{\nu,j}^{\text{lab}} \right)^2} \quad (2)$$

525 where both experimental ($\tau_{\nu,j}^{\text{lab}}$) and observational ($\tau_{\nu,i}^{\text{obs}}$) spectrum 526
are converted to wavenumber space (ν), w_j is the scale factor, 527
and m and n are the m th and n th data point. The absorbance lab- 528
oratory data (Abs) are converted to an optical depth scale by the 529
equation $\tau_{\nu}^{\text{lab}} = 2.3Abs_{\nu}$. In the degeneracy analysis shown in 530
Section 3.5, the error of the data is taken into account.

531 In a nutshell, ENIIGMA uses genetic modelling algorithms for 532
searching the optimal coefficients of the linear combination (w). 533
Genetic algorithms are robust optimization techniques based on 534
the processes of natural selection that aim to find the global mini- 535
mum solution for complex problems (Holland 1975; Koza 1992). 536
Once the best fit is found, ENIIGMA calculates the ice column 537
density of each component using the following equation:

$$N_{\text{ice}} = \frac{1}{A} \int_{\nu_1}^{\nu_2} \tau_{\nu}^{\text{lab}} d\nu, \quad (3)$$

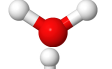
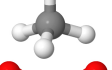
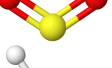
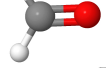
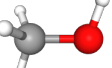
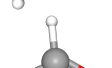

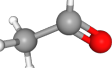
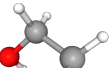
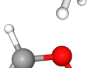
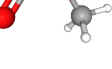
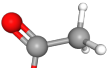
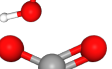
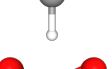
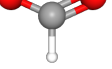
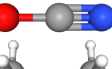
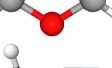
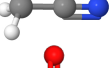
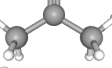
538 where A is the vibrational mode band strength of the molecule, 539
which is listed in Table 1. The band strengths of molecules 540
change depending on the chemical environment. For this reason, 541
we adopt values of corrected band strengths, when available, to 542
derive the ice column densities. The derivation of band strengths 543
is not straightforward because it depends on the ice density. The 544
typical band strength uncertainties are around 15% and 30% for 545
pure and mixed ices, respectively (Rachid et al. 2022; Slavcin- 546
ska et al. 2023).

547 The laboratory data considered in this paper are listed in Ap- 548
pendix C. These data were taken mainly from the Leiden Ice 549
Database for Astrochemistry² (LIDA; Rocha et al. 2022) and 550
from the Goddard NASA database³. The methodology used by 551
ENIIGMA to test the data available is detailed in Rocha et al. 552
(2021). Here, we provide a brief description of the method. In 553
the first stage ENIIGMA combines IR spectra of pure ice at low 554
temperature with pure ice at high temperature. The best group 555
of solutions is passed to the second step. In the second stage, 556
ENIIGMA combines the previous best solution with pure ice, with 557
all ice mixtures in the ENIIGMA database in a sequential way. At 558
this stage, all data that has an IR feature in the range fitted was 559
tested. Finally, ENIIGMA passes the best-ranked groups of solu- 560
tions to a final stage, where species from one group of solutions 561
are mixed and combined with species from another group. This 562
allows the code to diversify the number of combinations and in- 563
creases the possibility for the code to find the global minimum 564
solution not only among the coefficients but also among the lab- 565
oratory data available. In total, the code tested 3173 different

² <https://icedb.strw.leidenuniv.nl/>

³ <https://science.gsfc.nasa.gov/691/cosmicice/spectra.html>

Table 1. List of vibrational transitions and band strengths of molecules considered in this paper.

Structure	Chemical formula	Name	λ [μm]	ν [cm^{-1}]	Identification	\mathcal{A} [cm molec^{-1}]	References
	H ₂ O	Water	13.20	760	libration	3.2×10^{-17}	[1]
	CH ₄	Methane	7.67	1303	CH ₄ def.	8.4×10^{-18}	[1]
	SO ₂	Sulfur dioxide	7.60	1320	SO ₂ stretch	3.4×10^{-17}	[2]
	H ₂ CO	Formaldehyde	8.04	1244	CH ₂ rock	1.0×10^{-18}	[1]
	CH ₃ OH	Methanol	9.74	1026	C–O stretch	1.8×10^{-17}	[1]
	HCOOH	Formic acid	8.22	1216	C–O stretch	2.9×10^{-17}	[1]
	CH ₃ CHO	Acetaldehyde	7.41	1349	CH ₃ s-def./CH wag.	$4.1 \times 10^{-18,a}$	[3]
	CH ₃ CH ₂ OH	Ethanol	7.23	1383	CH ₃ s-def.	$2.4 \times 10^{-18,a}$	[4]
	CH ₃ OCHO	Methyl formate	8.25	1211	C–O stretch	$2.52 \times 10^{-17,a}$	[5]
						$2.28 \times 10^{-17,b}$	[5]
	CH ₃ COOH	Acetic acid	7.82	1278	OH bend	4.57×10^{-17}	[6]
	HCOO ⁻ (B1)	Formate ion	7.23	1383	C–O stretch	8.0×10^{-18}	[3]
	HCOO ⁻ (B2)	Formate ion	7.38	1355	C–O stretch	1.7×10^{-17}	[3]
	OCN ⁻	Cyanate ion	7.62	1312	Comb. ($2\nu_2$)	7.45×10^{-18}	[6]
	CH ₃ OCH ₃	Dimethyl ether	8.59	1163	COC str. + CH ₃ rock.	$4.9 \times 10^{-18,a}$	[5]
	CH ₃ CN	Methyl cyanide	7.27	1374	CH ₃ sym. def.	$1.2 \times 10^{-18,a}$	[5]
	CH ₃ COCH ₃	Acetone	7.33	1363	CCC asym. str.	$1.2 \times 10^{-17,a}$	[7]
	CH ₃ NH ₂	Methylamine	8.5	1176	CH ₃ rock	$1.3 \times 10^{-18,a}$	[8]
	NH ₂ CHO	Formamide	7.2	1388	CH bend	$1.4 \times 10^{-17,a}$	[9]
	HCOCH ₂ OH	Glycolaldehyde	7.3	1372	CH bend	7.7×10^{-18}	[10]

Notes. [1] Bouilloud et al. (2015), [2] Boogert et al. (1997), [3] Hudson & Ferrante (2020), [4] Boudin et al. (1998), [5] Terwisscha van Scheltinga et al. (2021), [6] This work - see Appendix D. ^aMixture with H₂O. ^bMixture with CH₃OH, [7] Rachid et al. (2020), [8] Rachid et al. (2021), [9] Slavicinska et al. (2023), [10] Hudson et al. (2005)

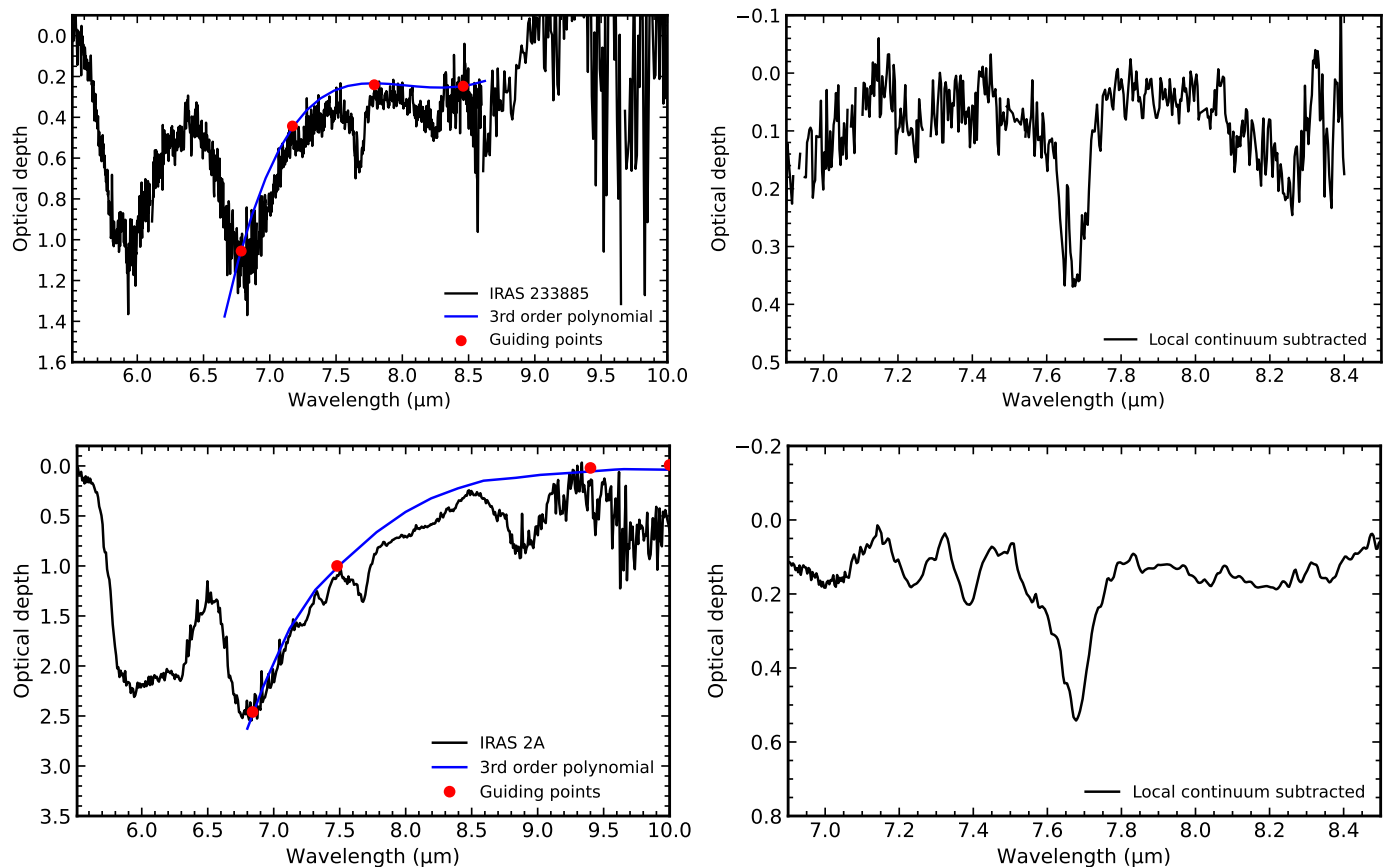


Fig. 5. Left: Local continuum in the 6.8–8.6 spectral range using a fourth-order polynomial function. Right: Isolated 6.8–8.6 optical depth spectrum in both protostars.

566 combinations, where the best solution is the best-ranked group
567 of components based on the RMSE value.

568 We note that for the purpose of this paper, we subtract the
569 absorption profiles of H_2O and CH_3OH around $6.8 \mu\text{m}$ from the
570 ice mixtures using a local subtraction with a polynomial function
571 (see Appendix E). This enables fitting the observational data after
572 local subtraction. As previously mentioned, the contribution
573 of these two molecules is taken into account in the polynomial fit
574 used to trace the local continuum between 6.8 and $8.6 \mu\text{m}$. Most
575 of the COM laboratory data have a spectral resolving power of
576 $R = 5000$, which is degraded to the nominal spectral resolution
577 of the two sources ($R \sim 3500$) around $7\text{--}8 \mu\text{m}$. In the case of
578 HCOO^- and OCN^- , we isolated the ice bands of these ions using
579 a local baseline subtraction. These two species are formed
580 from molecules engaged in an acid-base reaction, also known as
581 Bronsted-Lowry acid-base theory (Brönsted 1923; Lowry 1923),
582 and also seen in interstellar ices (e.g., Grim & Greenberg 1987;
583 Schutte & Khanna 2003; van Broekhuizen et al. 2004). The
584 amount of ions formed depends on the initial abundances of the
585 parent molecules. By isolating these bands, one can mimic at
586 first order, different initial conditions of parent species. It is also
587 worth mentioning that the baselines of HCOOH ice mixture are
588 checked before the analysis. Öberg et al. (2011) comments that
589 one should be careful when deriving the formic acid and formate
590 ion column densities because of baseline issues in some
591 experimental data measured further in the past. In addition, it
592 is important to note that HCOO^- and HCOOH share a band at
593 $7.2 \mu\text{m}$. For that reason, we would recommend using the $7.4 \mu\text{m}$
594 to quantify HCOO^- .

3.5. Degeneracy analysis

595 The ENIIGMA fitting tool performs a degeneracy analysis of the
596 coefficients in the linear combination that results in the best fit.
597 Briefly, the code performs a Gaussian variation around each coeffi-
598 cient by using the numpy function `numpy.random.normal`
599 (Harris et al. 2020), and is given by:
600

$$p(x) = \frac{1}{\sqrt{2\pi\sigma^2}} \exp\left[-\frac{(x-\mu)^2}{2\sigma^2}\right] \quad (4)$$

601 where μ values are the optimal coefficients, and σ is the standard
602 deviation around μ . This analysis allows us to calculate χ^2 values
603 for each new linear combination, and derive confidence intervals
604 based on a $\Delta\chi^2$ map (Avni & Bahcall 1980), which is formulated
605 as:

$$\chi^2 = \frac{1}{dof} \sum_{i=0}^{n-1} \left(\frac{\tau_{v,i}^{\text{obs}} - \sum_{j=0}^{m-1} w_j \tau_{v,j}^{\text{lab}}}{\gamma_{v,i}^{\text{obs}}} \right)^2 \quad (5a)$$

$$\Delta\chi^2(\alpha, \epsilon) = \chi^2 - \chi_{min}^2 \quad (5b)$$

606 where *dof* is the number of degrees of freedom, γ is the error
607 in the observational optical depth spectrum propagated from
608 the flux error assumed to be 10%, α and ϵ are the statistical sig-
609 nificance and the number of free parameters, respectively. χ_{min}^2
610 corresponds to the goodness-of-fit in the global minimum solu-
611 tion.

612 ENIIGMA also quantifies the statistical significance of a given
613 IR spectrum based on its recurrence, which is defined as:

$$\mathcal{R} = \frac{f_i}{S}, \quad (6)$$

614 where f_i is the absolute frequency of sample i (i.e. how many
615 times a specific laboratory data participates in the fit) and S is
616 the total number of solutions. If $\mathcal{R} = 100\%$, the chemical species
617 cannot be excluded from the fit. On the other hand, lower per-
618 centages mean that the spectrum can be replaced by another one
619 with a similar spectral shape without going outside of the confi-
620 dence intervals. While the confidence interval analysis evaluates
621 the degeneracy among the components in the best fit, the recur-
622 rence analysis quantifies the degeneracy among different spectral
623 data.

624 3.6. Criteria for firm COM ice detections

625 Boogert et al. (2015) classify three types of detection in ices:

- 626 1. Secure: multiple bands or bands of isotopologues are de-
627 tected in high-quality spectra;
- 628 2. Likely: A single band is detected and the profile matches the
629 laboratory spectra;
- 630 3. Possibly: A single band is detected and there is no exact
631 match between the profile and the laboratory spectra;

632 COMs bands are naturally weak, and therefore the isotopo-
633 logues criteria in (1) will be hardly satisfied for solid-phase
634 detections. In addition, to these three criteria, Jørgensen et al.
635 (2020) discuss gauges for the detection of exotic chemical
636 species in the context of gas-phase observations. They mention
637 that a firm identification needs a complete spectral survey with a
638 synthetic spectrum that accounts for all the bands of the identi-
639 fied molecules instead of using independent analytical functions
640 (e.g., Gaussian fits) of individual lines. These criteria can also
641 be applied in the context of COMs in ice, and it is strongly rec-
642 ommended to use IR laboratory data for comparison instead of
643 analytical functions (e.g., Gaussian, Lorentzian).

644 We note that different from gas-phase observations, where
645 the emission profiles are narrow and isolated, solid-phase ab-
646 sorption profiles are often blended because of the common func-
647 tional groups and broader spectral features. In addition, because
648 of the ice matrix in which the molecules are embedded, the shape
649 of the absorption bands change, with mixing ratio and tempera-
650 ture (e.g., Öberg et al. 2007; Bouwman et al. 2007). While ice
651 COMs show peculiar band shapes at high temperatures (> 70 K),
652 they are very similar at lower temperatures (see Terwisscha van
653 Scheltinga et al. (2018); Rachid et al. (2020, 2021); Terwisscha
654 van Scheltinga et al. (2021); Rachid et al. (2022); Slavicska
655 et al. (2023)). In this sense, we add to the criteria presented by
656 Boogert et al. (2015) and Jørgensen et al. (2020) that a degen-
657 eracy analysis of molecules sharing similar functional groups is
658 needed in order to claim a firm ice COM detection.

659 3.7. Remarks for future works

660 In this section, we point out some aspects important to guide
661 future works on the analysis of COMs fingerprints in protostellar
662 ices:

- 663 – The intensities of COM bands in observational data are
664 weaker compared to the major ice components. In this case,
665 special attention must be paid to the baseline correction of
666 COM IR laboratory spectra. Any minor inflexion can mimic
667 a spurious feature and lead to misinterpretation of the obser-
668 vational spectrum. An example is presented in Appendix F.
669 The example is given for $\text{H}_2\text{O}:\text{CH}_3\text{CH}_2\text{OH}$ ice spectrum
670 where a 7th-order polynomial is used to baseline correct the
671 spectrum. We show that if a lower number of data points is

672 considered around $8\ \mu\text{m}$, the polynomial function can fluctu-
673 ate and originate spurious features in the final data. Instead
674 cubic spline functions can be used to mitigate those fluc-
675 tuations. Another issue, not shown here, is that some weak
676 bands can be removed unintentionally if the user is not fam-
677 iliar with a particular dataset and source details.

- Tracing the local continuum on the observed spectrum is as
678 critical as the spectral fitting. In the COMs fingerprint region,
679 where broad bands are present, one should be careful when
680 attributing zero absorption for tracing the local continuum
681 between $6.8\text{--}8.6\ \mu\text{m}$.
682
- Analysis of observational spectra in the range between 6.8
683 and $8.6\ \mu\text{m}$ using laboratory data of H_2O - or CH_3OH -
684 containing ices must have the features of these two molecules
685 subtracted to allow direct comparison with observational
686 data after local continuum removal. Appendix E shows an
687 example of how the $\text{CH}_3\text{CH}_2\text{OH}$ bands in the mixture with
688 H_2O and CH_3OH were isolated. While a single 4th-order
689 polynomial was used in the case of $\text{H}_2\text{O}:\text{CH}_3\text{CH}_2\text{OH}$, three
690 polynomial functions with different orders were needed in
691 the case of $\text{CH}_3\text{OH}:\text{CH}_3\text{CH}_2\text{OH}$, which increases the risk of
692 creating spurious features.
693

694 4. Results

695 In this section, we show the fitting results of the protostars
696 IRAS 23385+6053 and IRAS 2A in the range between 6.8 and
697 $8.4\ \mu\text{m}$, as well as the confidence interval analysis.

698 4.1. Spectral decomposition and feature analysis

699 The fits of the IRAS23385 and IRAS 2A spectra are shown
700 in Figure 6 top and bottom, respectively (see Appendix G for
701 an incremental version of these figures, following the individ-
702 ual fitting steps). These two MIRI/MRS spectra are decom-
703 posed using nine laboratory spectra which were selected by
704 ENIGMA and they provide the global minimum solution. Among
705 the COMs fitted in this work are, CH_3CHO , $\text{CH}_3\text{CH}_2\text{OH}$,
706 CH_3OCHO (methyl formate) and CH_3COOH (acetic acid), with
707 the first three robustly detected (see §3.6 and §4.2). The simple
708 molecules identified are CH_4 , SO_2 , and HCOOH . Additionally,
709 we found a good match of two ions, HCOO^- and OCN^- . Be-
710 cause of the contribution of HCOO^- with similar intensities at
711 7.2 and $7.4\ \mu\text{m}$, we stress that these two bands are not only asso-
712 ciated with COMs.

713 The band around $7.68\ \mu\text{m}$ was clearly visible in previous ice
714 observations (e.g., Gibb et al. 2004; Öberg et al. 2008), and is
715 now seen in JWST spectra with unprecedented S/N and spec-
716 tral resolution. CH_4 ice is the main carrier of this feature, and
717 Öberg et al. (2008) suggests that SO_2 can contribute to the blue
718 wing of this band based on a Gaussian decomposition of the
719 $7.68\ \mu\text{m}$ feature. In the present work, this band is decomposed
720 into four components, with CH_4 mixed with H_2O the dominant
721 carrier. This is in line with laboratory experiments suggesting
722 a common formation pathway for CH_4 and H_2O ices (Qasim
723 et al. 2020). The blue wing has contributions of SO_2 mixed with
724 CH_3OH , and the negative cyanate ion (OCN^-) for both sources.
725 The red wing of this band can be fitted with CH_3COOH in the
726 case of IRAS 2A but is not present in IRAS 23385. A good cor-
727 relation in ice column density between sulfur-bearing molecules
728 and methanol was observed before by Boogert et al. (1997) and
729 Boogert et al. (2022). OCN^- is one of the ions formed from
730 molecules engaged in acid-base reactions, and it has a band at

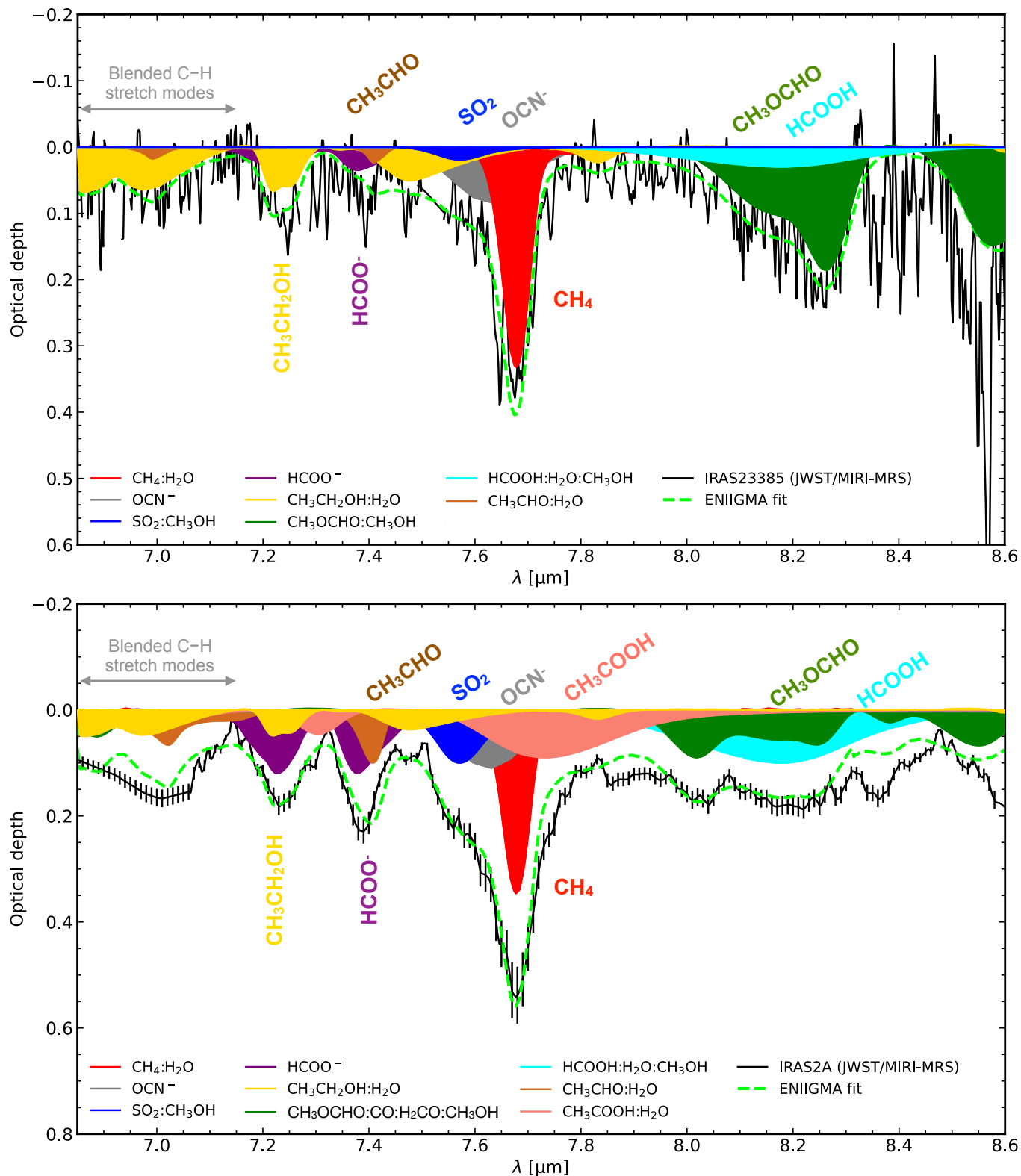


Fig. 6. ENIIGMA fits of IRAS 23385 (top) and IRAS 2A (bottom). Gas-phase lines are masked. The figure labels show the ice mixture used in the fits, and a simplified version with the names of the chemical species names is shown close to the bands. The corresponding temperature of these laboratory spectra ranges between 10 K and 15 K.

731 7.63 μm , in addition to its well-known feature at 4.61 μm , commonly seen towards protostars. In fact, recent observations of
 732 IRAS 2A with the JWST/Near-Infrared Spectrometer (NIRSpec)
 733 detect the 4.61 μm band, thus confirming the presence of OCN^-
 734 in the ices towards IRAS 2A as part of the JOYS program. The
 735

analysis of the NIRSpec data of this source will be presented in
 a future paper, but we calculate the ice column density of OCN^-
 at 4.61 μm to check the consistency of the fit in the mid-IR (see
 Section 4.3). As a result, the blue wing of the 7.68 μm feature is
 composed both by SO_2 and OCN^- . We also note that OCN^- in
 736
 737
 738
 739
 740

both sources has a similar intensity, whereas SO₂ is stronger in IRAS 2A.

Protostar observations in the mid-IR show the 7.2 and 7.4 μm features with similar strengths across a number of sources, which suggests the dominance of a single species. In fact, we find that the formate ion, initially proposed by Schutte et al. (1999), matches well the 7.2 and 7.4 μm bands of IRAS 2A and IRAS 23385. This ion is formed by the acid-base reaction of H₂O:NH₃:HCOOH (100:2.6:2) ice mixture at 14 K (Gálvez et al. 2010). The intensity of the formate ion in IRAS 2A is a factor of three stronger than in IRAS 23385. In Appendix H, we compare the 7.2 and 7.4 μm band with the formate ion at other temperatures. The formate ion spectrum at 150 K has a broader profile at 7.4 μm, whereas laboratory data at 210 K shows a strong feature at 7.3 μm that is not observed in either source. Thus, the 7.2 and 7.4 μm features are a signature of ices dominated by ions in cold regions. Our results also show that despite HCOO⁻ being the main carrier of the 7.2 and 7.4 μm bands, other components can contribute to these two features separately as discussed below.

The presence of HCOO⁻ in the ice is supported by the detection of HCOOH at 8.2 μm, in addition to its band at 5.8 μm. The best fit is found when formic acid is mixed with CH₃OH and H₂O as suggested by Bisschop et al. (2007). The lower intensity of formic acid in IRAS 23385 can be related to the nature of the source. At warmer temperatures (>50 K), HCOOH is more efficiently destroyed via an acid-base reaction (e.g., Schutte et al. 1999; Gálvez et al. 2010). Another possibility is that HCOOH was not efficiently formed in this high-mass source because of the lower amount of CO ice available in a high-mass star-forming region.

CH₃CH₂OH is detected in both protostars through the absorption of four vibrational modes at 6.8–7.15 μm (C–H stretch), 7.25 μm (CH₃ s-deformation), 7.4–7.7 μm (OH deformation) and at 7.85 μm (CH₂ torsion). Among the ethanol data tested, the mixture with H₂O provides the best fit. Ethanol is stronger and contributes significantly to the 7.2 μm band in IRAS 23385, whereas it is less prominent in IRAS 2A.

CH₃CHO shows weak absorption around 7.03 μm (C–H stretch), and at 7.41 μm (CH₃ s-deformation/CH wagging). These bands are stronger in IRAS 2A than in IRAS 23385. Experimental characterization of the CH₃ s-deformation/CH wagging shows a strong dependence on the chemical environment and temperature (Terwisscha van Scheltinga et al. 2018). The closer match with both protostars is for acetaldehyde mixed with H₂O ice, which has a peak at 7.41 μm. The observed band, however, has a peak at 7.38 μm, indicating other carriers for this band (e.g., HCOO⁻).

CH₃OCHO is observed in both sources around 8.2 and 8.6 μm, but with different spectral shapes and intensities. In IRAS 23385, the methyl formate band is better fitted by a mixture with methanol at 15 K, although the data at 30 and 80 K are also statistically likely (see Section 4.2.3). Other methyl formate mixtures do not exhibit such an asymmetric profile, which makes them unlikely to be the carrier of this band (see Section 5.1.1). While the shape of the 8.2 μm is well defined, this is not the case for the 8.6 μm band, which is affected by saturation due to the strong silicate feature. In IRAS 2A the bands at 8.2 and 8.6 μm are consistent with a mixture containing CO, H₂CO, and CH₃OH. This ice mixture of CH₃OCHO also fits well the 8.0 μm band associated with H₂CO.

CH₃COOH is found to fit well to the IRAS 2A spectrum, but not that of IRAS 23385. In addition, a better match with the observations is found for acetic acid mixed with H₂O ice. The two identified bands are located at 7.3 and 7.7 μm (salmon colour in

Figure 6, bottom). Specifically, the 7.7 μm band in IRAS 2A has a broad profile that is more than just CH₄ and it is necessary to fit the absorption excess around this region without strong overlap between 7.7 and 7.85 μm. The 7.3 μm is slightly over-estimated in the fits, because of the amount of absorption needed to fit the 7.7 μm band. This can be because of the SO₂ emission lines subtraction around 7.3 μm or the uncertainties involved in the local continuum choice around the 7.7 μm band.

The robustness of these detections based on the difference in local continuum choice is discussed in Section 4.2.4 for IRAS 2A, the higher S/N source.

4.2. Statistical analysis

4.2.1. Confidence intervals

We derive the confidence intervals (see Section 3.5) of the fits for IRAS 23385 and IRAS 2A in three different ranges separately: (i) 6.85–7.5 μm, (ii) 7.5–7.8 μm and (iii) 7.8–8.6 μm. The components in these three ranges are relatively isolated, and therefore their contribution in one given interval is kept constant when analysing other ranges.

In Figure 7, we show the confidence intervals for the fit of IRAS 2A in the range between 7.5 and 7.8 μm. The yellow and red contours indicate 2σ and 3σ confidence intervals. Based on these contours, one can note that all components, but CH₃CH₂OH, are required to fit IRAS 2A. In this particular spectral range (7.5 and 7.8 μm), only a small portion of CH₃CH₂OH spectrum at 7.5 μm contributes to the absorption. Therefore, the confidence interval analysis shows that CH₃CH₂OH is not crucial to fit the 7.5 and 7.8 μm. The contribution of CH₃CH₂OH in IRAS 2A is better evaluated using the range between 6.86 and 7.5 μm, which is shown in Appendix I. In Figure I.1 (top), the CH₃CH₂OH:H₂O is not zero, which reinforces the idea that CH₃CH₂OH is robustly found in IRAS 2A. Another important result from Figure 7 is that SO₂ (w1) and OCN⁻ (w3) are both required to fit IRAS 2A since their coefficients cannot be zero. Finally, CH₃COOH:H₂O cannot be excluded as a solution based on this statistical analysis. Further analysis of the 6.86–7.5 μm range allows us to conclude that CH₃CHO, HCOO⁻, and HCOOH are also robust detections. In addition to these chemical species, Figure I.1 (bottom) also shows that CH₃COOH cannot be excluded from the fit obtained with one specific continuum subtraction. More details for CH₃COOH are presented in Section 4.2.4. The analysis of the spectral range between 7.8 and 8.6 μm, shows that another COM, CH₃OCHO is also a robust detection in IRAS 2A spectrum.

A similar analysis is performed for IRAS 23385 (Figures I.2 and I.3). For the range between 7.5 and 7.8 μm, CH₄ and OCN⁻ are essential, whereas SO₂ can be statistically not required due to the low S/N in IRAS 23385 spectrum. Likewise, the analysis of the 6.86–7.5 μm range shows that CH₃CH₂OH, CH₃CHO and HCOOH are robust detections, whereas the formate ion (HCOO⁻) absorption may be explained by CH₃CH₂OH or HCOOH ice features. For the 7.8–8.6 μm interval, both HCOOH and methyl formate (CH₃OCHO) are robust detections.

4.2.2. Recurrence of the ice components

A complementary statistical analysis is performed on the recurrence of all solutions within a given confidence interval. The difference in this method is that we do not vary the coefficient values of each solution, but the laboratory data instead. Figure 8 (top) shows the recurrence of the IRAS 2A fit of 15 chemical

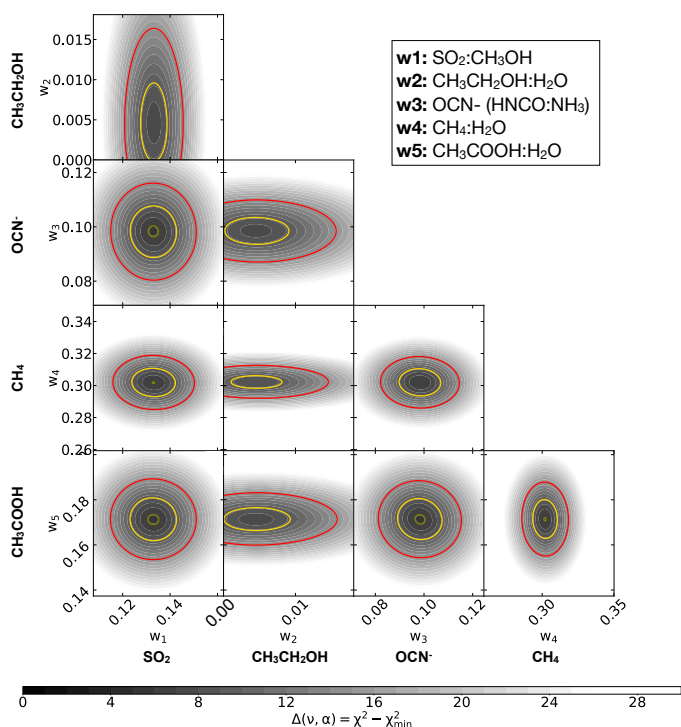


Fig. 7. Corner plots showing the IRAS 2A coefficient confidence intervals for the range between 7.5 and 7.8 μm . The grey scale colour is the $\Delta\chi^2$ map derived from a total of 5000 values. Yellow and red contours represent 2 and 3 σ significance, respectively.

species inside 3 σ confidence interval and considering several solutions. This analysis indicates that the COMs providing the best fits (see Figure 6), are the most recurrent in the bar chart (87.5% $\leq R \leq 100\%$), and therefore cannot be excluded as a solution. Other chemical species, such as CH₃NH₂, CH₃OCH₃, NH₂CHO, HCOCH₂OH and CH₃COCH₃, some of which have been suggested previously to contribute in this range, have a recurrence lower than 50%. This is not sufficient to claim a firm detection and at best upper limits can be derived.

The reason that formamide and acetone are not part of the global fit is that the formate ion band shape dominates the absorption profile at 7.2 and 7.4 μm . In addition, acetic acid and ethanol also contribute to these two absorption profiles. In the cases of methylamine and dimethyl ether, the fits indicate that methyl formate contributes more to the 8.5–8.6 μm range.

The same analysis is done for IRAS 23385, shown in Figure 8 (bottom). Since the MIRI data for this source have a lower S/N compared to IRAS 2A, there exist slightly more variations among the recurrence values. The components found in the global fit have a recurrence above 85%, whereas other COMs are recurrent by $\sim 40\%$ or less. Interestingly, CH₃COOH does not participate in any of the solutions tested because OCN⁻ and CH₃CH₂OH account for all the absorption around 7.7 μm .

4.2.3. Temperature degeneracy

Despite the well-known changes in the band profiles of astrophysical ices with temperature, there are some absorption features that barely vary with temperature. Consequently, the fitting routine is not able to distinguish between these data. Rocha et al. (2021) show that when data that is known to provide a good fit is arbitrarily removed from the database, the ENIIGMA fitting tool uses another data of the same species, but with similar temper-

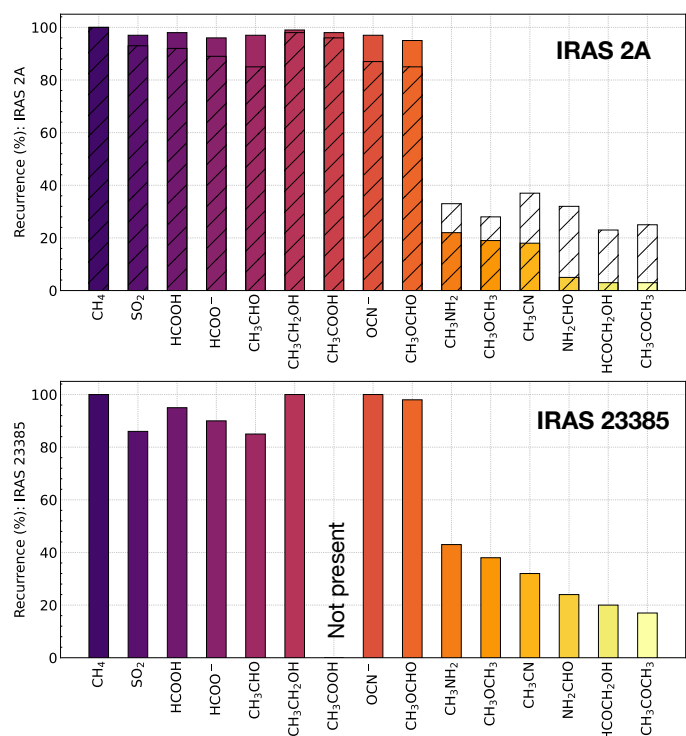


Fig. 8. Bar plot showing the recurrence of the difference chemical species to the fit in IRAS 2A (top) and IRAS 23385 (bottom). Recurrences above 50% are considered essential to the fit and robust detection. CH₃COOH in IRAS 23385 does not occur in any of the solutions. In the case of IRAS 2A (top panel) we present hatched bars that show the recurrence of the solutions if the errors in optical depth are increased by a factor of three.

ature when possible. This slightly increases the fitness function value, but the fit is still good within the confidence intervals. In this section, we perform a statistical analysis to evaluate which temperature ranges are degenerate and provide a good fit, from those temperature ranges that can be excluded as a solution.

Figure 9 shows the recurrence plots for CH₃CH₂OH, CH₃CHO and CH₃OCHO in IRAS 2A and CH₃OCHO in IRAS 23385 for different temperatures settings available. The analysis of CH₃CH₂OH and CH₃CHO is not performed for IRAS 23385 because of the low S/N in the spectral range considered for the fits. To calculate the recurrence plot for these COMs, we selected the solutions that are ranked inside a 3 σ confidence interval. For example, in the case of CH₃CH₂OH, we found 352 solutions where ethanol is present. The ethanol mixture at 15 K is present in all of these solutions, and therefore it has a recurrence of 100%. There are solutions that combine the low temperature (15%) ethanol mixture with other temperatures (e.g., 30, 70, 100 K). Because of the similarity of the ethanol bands in the fitted range, the recurrence of these additional ethanol data is slightly reduced, but still high. For the data at 150 and 160 K, there are around 70 solutions using one of these data, which gives a recurrence of $\sim 20\%$. Another way to perform the same analysis is by using the best global solution as the initial guess and running new fits by replacing the IR spectra of specific COMs at different temperatures. This forces ENIIGMA to use only one CH₃CH₂OH data at a time, and prevents overlaps of data with similar spectral shapes. For ethanol, we obtain a total of 9 solutions if the presence of the other components is fixed. In this case, the temperature range between 15 and 100 K has a recurrence of 100%, and the higher temperatures, have a recur-

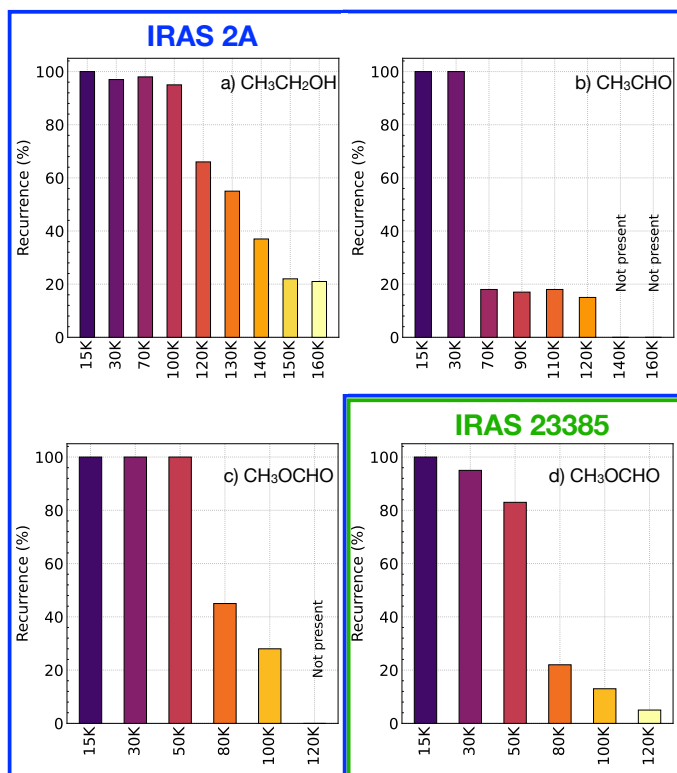


Fig. 9. Bar plot showing the recurrence of the same ice mixture, but at different temperatures. Plots inside the blue and green polygons refer to IRAS 2A and IRAS 23385, respectively.

925 recurrence of 0%. In the case of ethanol, IR spectra with temperatures
 926 below 100 K are degenerate, and all $\text{CH}_3\text{CH}_2\text{OH}:\text{H}_2\text{O}$ mixtures
 927 fit IRAS 2A in that temperature range. Above 120 K, the ethanol
 928 ice mixture no longer fits the IRAS 2A spectrum well because of
 929 band broadening and shift.

930 Repeating the same procedure for the other species, we
 931 notice a similar behaviour. The fits with acetaldehyde in
 932 IRAS 2A are degenerate below 30 K. Above this temperature,
 933 $\text{CH}_3\text{CHO}:\text{H}_2\text{O}$ ice mixtures do not offer likely solutions mostly
 934 because of band shift. The fits with methyl formate are degener-
 935 ated below 50 K in IRAS 2A. At higher temperatures, some sub-
 936 structures arise in the CH_3OCHO spectrum that deviates from
 937 the observational data. Similarly, in IRAS 23385, methyl for-
 938 mate is degenerated below 50 K, whereas solutions at 80 K and
 939 above are less recurrent because of changes in the band profile.
 940 In conclusion, it is likely that most of the ices towards IRAS 2A
 941 and IRAS 23385 are located in regions with temperatures below
 942 50 K.

943 4.2.4. Robustness of detection based on different local 944 continuum choices

945 Other local continuum fits for IRAS 2A (higher S/N) in the 6.8–
 946 8.6 μm region are also investigated and presented in Appendix J.
 947 The first three panels of Figure J.1 display different continuum
 948 profiles, where the top panel is the version adopted for the analy-
 949 sis in this paper that traced a third-order polynomial to the guid-
 950 ing points. The second panel displays the fourth-order polynomi-
 951 al where the red dot is added to the guiding points. In this
 952 case, the continuum is slightly elevated at shorter wavelengths
 953 to accommodate the fit to the extra point at 8.5 μm . The third
 954 panel presents the continuum when two extra points are added

($\lambda = 7.8 \mu\text{m}$ and $8.5 \mu\text{m}$), and a sixth-order polynomial is used. 955
 All subtracted spectra using these three approaches are shown 956
 in the bottom panel of Figure J.1. The major difference is seen 957
 in the last case (orange continuum), which completely removes 958
 any absorption excess at $7.8 \mu\text{m}$, thus excluding any band at this 959
 wavelength. 960

961 Given the variability of the optical depth spectra of IRAS 2A
 962 between 6.8–8.6 μm with the choice of the local continuum, it is
 963 worth accessing the robustness of the detections reported in the
 964 previous sections considering other continuum profiles. This is
 965 shown in Figure J.2. Figure J.2 top presents the new fit assuming
 966 the red continuum profile (inset panel) from Fig J.1. This spectral
 967 fit remains good and all components found in the best fit are still
 968 present. The only issue is found at 8.5 μm (added guiding point)
 969 where the CH_3OCHO band is slightly over-predicted. This situ-
 970 ation changes when the orange continuum is used to isolate the
 971 absorption features in IRAS 2A. The bottom panel of Figure J.2
 972 depicts a fit where CH_3COOH is no longer needed because of
 973 the guiding point at 7.8 μm to trace the local continuum. In this
 974 version of the fit, the HCOO^- and OCN^- components become
 975 much stronger than in the other cases, and the COMs bands are
 976 reduced by a factor between 1.5–2.0. A clear mismatch is seen
 977 around 7 μm because of the reduction of the COM bands. Also,
 978 there is more excess around 7.3 μm that is not fitted with the
 979 other COMs tentatively detected in this work (see Section 4.4).

980 This analysis reinforces that the detections of CH_3CHO ,
 981 $\text{CH}_3\text{CH}_2\text{OH}$ and CH_3OCHO , as well as the ions and the simple
 982 molecules, are robust and do not depend on the local continuum
 983 choice. Clearly, the only exception is for CH_3COOH . However, a
 984 valid question is what other chemical species would create an ab-
 985 sorption profile similar to the orange continuum. There is no triv-
 986 ial answer to this question. A tentative explanation comes from
 987 the five components decomposition from Boogert et al. (2008),
 988 in which only the C5 broad feature contributes to the 7.8 μm .
 989 The nature of the C5 component is not well understood and can
 990 be related to a flat profile of high-temperature H_2O ice bending
 991 mode, the overlap of other negative ions (HCO_3^- , NO_3^- , NO_2^-)
 992 or organic refractory residue produced by energetic processing.
 993 The flatter bending mode would have little absorption at 7.8 μm
 994 and therefore is less likely, but the other two options are strong
 995 candidates.

996 4.3. Ice column densities and abundances

997 The column densities of the molecules fitting the 6.8–8.6 μm
 998 range are presented in Table 2. To derive their abundances with
 999 respect to H_2O ice, we use the libration band around 12 μm to
 1000 calculate the water ice column density as shown in Appendix K.
 1001 These abundances are compared to literature values for low- and
 1002 high-mass protostars. In Section 5.3 we also show abundances
 1003 with respect to CH_3OH ice, in which the method to derive the
 1004 column density is demonstrated in Appendix K.

1005 The ice abundances of CH_4 , SO_2 , OCN^- , HCOO^- and
 1006 HCOOH are within or close to the range expected for LYSOs
 1007 and MYSOs. From the analysis in this paper, CH_4 , SO_2 , OCN^-
 1008 compose the band around 7.67 μm , whereas previous works as-
 1009 signed this band to only CH_4 , with a possible contribution of SO_2
 1010 (Öberg et al. 2008). Additionally, instead of using Gaussian pro-
 1011 files to derive the column densities, this paper uses laboratory
 1012 data of $\text{CH}_4:\text{H}_2\text{O}$ and $\text{SO}_2:\text{CH}_3\text{OH}$. Gaussian profiles provide
 1013 first-order approach analysis of the profile of the ice bands, but
 1014 they can under or overestimate the FWHM of real CH_4 and SO_2
 1015 bands.

Table 2. Ice column densities and abundances with respect to H₂O ice towards IRAS 2A and IRAS 23385. These values are compared to literature values for other objects.

Specie	N_{ice} (10^{17} cm ⁻²)		$X_{\text{H}_2\text{O}}$ (%)		Literature (% H ₂ O)		
	IRAS 2A	IRAS 23385	IRAS 2A	IRAS 23385	LYSOs	MYSOs	Comet 67P/C-G ^m
H ₂ O*	300±12	158±36	100	100	100	100	100
CH ₄ *	4.9 ^{7.5} _{3.2}	5.2 ^{6.8} _{4.3}	1.6	3.3	<3 ^a	1–11 ^b	0.340±0.07
SO ₂ *	0.6 ^{1.9} _{0.4}	0.2 ^{0.7} _{0.0}	0.2	0.1	0.08–0.76 ^a	< 0.9–1.4 ^b	0.127±0.100
HCOOH*	3.0 ^{5.3} _{1.7}	1.8 ^{2.7} _{1.3}	1.0	1.1	< 0.5–4 ^c	< 0.5–6 ^d	0.013±0.008
CH ₃ OH*	15, 23 [†]	...	5.0, 7.6	...	< 1–25 ^d	< 3–31 ^d	0.21±0.06
CH ₃ CHO*	2.2 ^{2.8} _{1.4}	0.7 ^{1.1} _{0.4}	0.7	0.4	...	<2.3 ^e	0.047±0.017
CH ₃ CH ₂ OH*	3.7 ^{4.5} _{0.5}	2.9 ^{4.1} _{1.9}	1.2	1.8	...	<1.9 ^e	0.039±0.023
CH ₃ OCHO*	0.2 ^{0.4} _{0.1}	1.1 ^{1.3} _{1.0}	0.1	0.7	<2.3 ^f	...	0.0034±0.002
CH ₃ COOH [‡]	0.9 ^{1.3} _{0.6}	0.0	0.3	0	0.0034±0.002
HCOO ⁻ * (7.4 μm)	1.4 ^{2.4} _{0.4}	0.3 ^{0.5} _{0.1}	0.4	0.2	~0.4 ^g	<0.3–2.3 ^b	...
OCN ⁻ *	3.7 ^{6.6} _{3.3}	0.9 ^{1.7} _{0.6}	1.2	0.6	< 0.1–1.1 ^h	0.04–4.7 ⁱ	...
H ₂ CO [‡]	12.4 ^{19.7} _{6.6}	...	4.1	...	~6 ^g	~2–7 ^b	0.32±0.1
Upper limits							
CH ₃ NH ₂	< 4.1	...	< 1.4	...	< 16 ^j	< 3.4 ^j	...
CH ₃ OCH ₃	< 2.5	...	< 0.8	0.039±0.023
CH ₃ COCH ₃	< 1.1	...	< 0.4	0.0047±0.0024
HCOCH ₂ OH	< 0.9	...	< 0.3	0.0034±0.002
CH ₃ CN	< 5.0	...	< 1.6	...	< 4.1 ^k	< 3.4 ^k	0.0059±0.0034
NH ₂ CHO	< 1.3	...	< 0.4	...	< 3.7 ^l	< 2.1 ^l	0.0040±0.0023
Glycine	< 0.1–0.6	...	< 0.03–0.2	~0.3 ^b	...

Notes. ^aÖberg et al. (2008), ^bGibb et al. (2004), ^cÖberg et al. (2011), ^dSchutte et al. (1999), ^eTerwisscha van Scheltinga et al. (2018), ^fTerwisscha van Scheltinga et al. (2021), ^gBoogert et al. (2008), ^hvan Broekhuizen et al. (2005), ⁱBoogert et al. (2022), ^jRachid et al. (2021), ^kRachid et al. (2022), ^lSlavicinska et al. (2023), ^mRubin et al. (2019). [†] The CH₃OH ice column density is considered a factor of 2 and 3 higher than the Gaussian fit shown in Figure K.2 because of the band saturation. *Chemical species with secure detection. [‡]Tentative detections. CH₃COOH depends on the local continuum choice. H₂CO is based on a single band of this molecule mixed in the ice with other CO, CH₃OH and CH₃OCHO.

In the case of OCN⁻, we derived ice column densities and abundances from the band at 7.62 μm for IRAS 2A. For consistency, we also calculated the ice column from the NIRSpec feature at 4.61 μm, which is 2.5×10¹⁷ cm⁻². Both values are consistent within the errors, and they result in OCN⁻ abundances in agreement with the range estimated in the literature for low-mass protostars (van Broekhuizen et al. 2005). For IRAS 23385, the OCN⁻ abundance calculated from the MIRI data is within the range found in MYSOs taken from Boogert et al. (2022).

Finally, the formic acid (HCOOH) and the formate ion (HCOO⁻) abundances are closely aligned with the literature values for both LYSOs and MYSOs. In the case of the formate ion in LYSOs, there is only one estimate in the literature for the low-mass protostar HH 46 IRS, which is similar to the abundance calculated for IRAS 2A. The ratios between HCOO⁻ and HCOOH are 0.46 and 0.16 for IRAS 2A and IRAS23385, respectively.

For the COMs, we derive ice column densities and abundances for CH₃CHO, CH₃CH₂OH, CH₃OCHO and CH₃COOH. In terms of ice abundance with respect to H₂O ice, IRAS 2A is more abundant in CH₃CHO by a factor of 1.75 compared to IRAS 23385. CH₃COOH is not detected in IRAS 23385, but has

an estimated abundance of 0.3% in IRAS 2A. CH₃CH₂OH and CH₃OCHO are more abundant in IRAS 23385 by a factor of 1.5 and 7, respectively, compared to IRAS 2A. We note that the CH₃CH₂OH abundance for IRAS 23385 is in line with the upper limit derived from the high-mass protostar W33A (Terwisscha van Scheltinga et al. 2018). The other ice abundances are consistent with the upper limits derived in the literature, illustrating that JWST can now probe deeper than previous instruments.

With respect to CH₃OH ice, the abundances are between 9.3–14.6% for CH₃CHO, 16.1–24.6% for CH₃CH₂OH, 0.9–1.3% for CH₃OCHO and 3.9–6.0% for CH₃COOH, depending on the lower and higher CH₃OH listed in Table 2. The values are much lower than the upper limits derived in the literature (Terwisscha van Scheltinga et al. 2018) for CH₃CHO (52%) and for CH₃CH₂OH (42%).

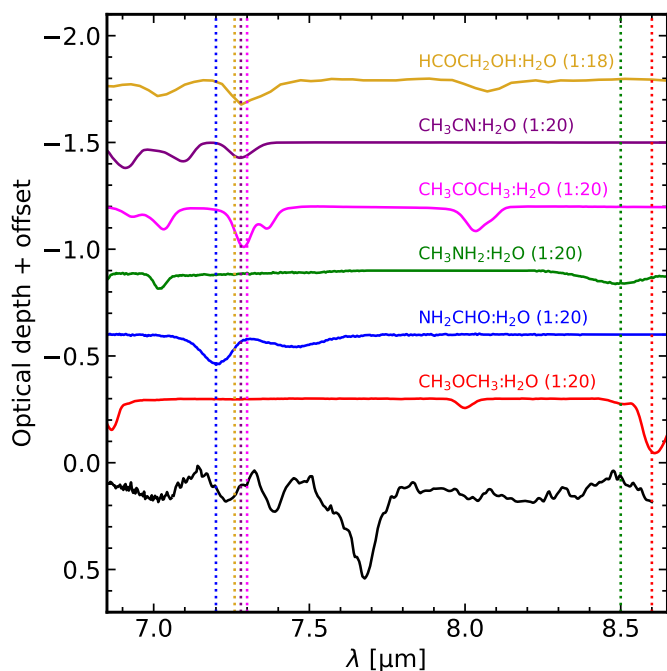


Fig. 10. IR spectra of COMs not contributing to the global fit, but with absorption features in the range between 6.8 and 8.6 μm . These spectra are scaled to the IRAS 2A spectrum (black) to derive upper limit column densities. The vertical dotted lines are colour-coded and indicate the features used to derive the ice column densities. A small horizontal shift in the vertical lines is used to distinguish the bands at 7.3 μm .

4.4. Tentative detections and upper limits on column densities

A few COMs were not part of the global solution shown in Figure 6. In this case, we perform a separate comparison of these data to check for tentative detections and derive upper limit column densities in IRAS 2A. This procedure is not applied to IRAS 23385 due to the low signal-to-noise ratio. For this step, we scale laboratory spectra of COMs at specific wavelengths to the MIRI spectrum. This allows us to take into account both the intensity and width of the IR ice band. We performed separate scaling for COMs that have overlaps of the IR features. The molecules used in this step are CH_3OCH_3 , CH_3COCH_3 , HCOCH_2OH , NH_2CHO , CH_3NH_2 and CH_3CN mixed with H_2O ice. Figure 10 shows the COMs spectra superposed to the IRAS 2A MIRI data, with upper limit column densities also listed in Table 2. To scale CH_3OCH_3 , we use the CH_3 -rock mode at 8.6 μm as a reference. This band has also contributions of ammonia and methyl formate. CH_3COCH_3 and CH_3CN have a CH_3 symmetric deformation mode at $\sim 7.3 \mu\text{m}$, and HCOCH_2OH a CH_2 deformation mode at the same position. Both CH_3COCH_3 and CH_3OCH_3 may contribute to the band at 8.1 μm due to the CCC asymmetric stretch. In the case of CH_3NH_2 , we use the CH_3 -rock mode at 8.5 μm as a reference, whereas the C–H bend at 7.2 μm is considered for NH_2CHO .

Finally, we also check the potential presence of solid-phase glycine, the simplest amino acid, in the spectrum of IRAS 2A. In Ioppolo et al. (2021), the solid-state formation of this simplest amino acid was proven. Glycine has many absorptions features in the IR, and the ωCH_2 mode at 7.46 μm is the strongest band of β -glycine. Depending on the glycine structure (e.g., neutral - $\text{NH}_2\text{CH}_2\text{COOH}$ or zwitterion - $\text{NH}_3^+\text{CH}_2\text{COO}^-$), the position of this band may shift (Potapov et al. 2022) or be nar-

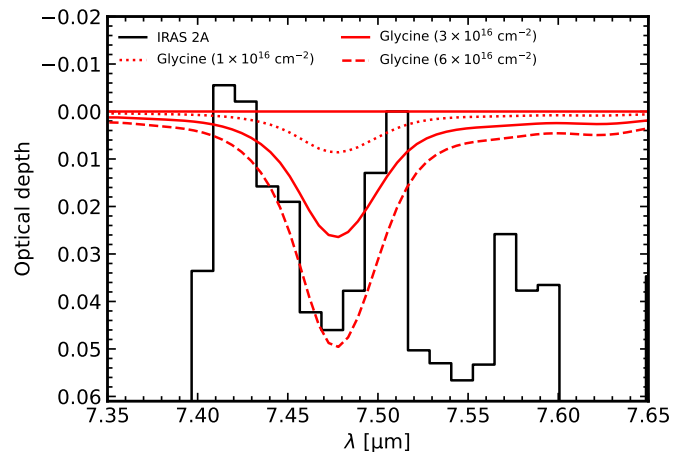


Fig. 11. Comparison of the ωCH mode of glycine IR spectrum (red) with local subtracted spectrum of IRAS 2A (black). The intensities of the glycine band are given for three ice column densities.

rowed if the molecule is mixed in an argon sample (Ehrenfreund et al. 2001). In this paper, we use the zwitterionic form ($\text{NH}_3^+\text{CH}_2\text{COO}^-$; Pilling et al. 2011), which is available in the UNIVAP database⁴. In Figure 11, we compare the local subtracted spectrum around the 7.46 μm band with the β -glycine data at three different column densities. We use the band strength from Holtom et al. (2005) of the 7.46 μm band, calculated as $1.16 \times 10^{-17} \text{ cm molecule}^{-1}$. This range of column densities is compatible with Gibb et al. (2004) who estimated an upper limit glycine column density of $3 \times 10^{16} \text{ cm}^{-2}$, based on the absorption feature around 5.8 μm band. With respect to H_2O ice, we find an upper limit of between 0.03–0.2% (See Section 4.3 and Table 2). This is close to the upper limit derived for W33A (<0.3; Gibb et al. 2004), and in agreement with the theoretical models (0.03–0.7%; Ioppolo et al. 2021).

4.5. Testing more complex alcohols and other molecules

In this section, we compare the IRAS 2A spectrum with two other alcohols more complex than $\text{CH}_3\text{CH}_2\text{OH}$, for instance, propanal ($\text{CH}(\text{O})\text{CH}_2\text{CH}_3$) and 1-propanol ($\text{CH}_3\text{CH}_2\text{CH}_2\text{OH}$). The goal is to check for similarities and differences between the functional groups of these alcohols with ethanol since these more complex alcohols are expected to have features at similar locations. It is worth mentioning that propanal and 1-propanol have been synthesized in experiments with ice analogues (Qasim et al. 2019) using atom addition reactions, and in the case of propanol, via CH_3OH ice UV irradiation (Tenelanda-Osorio et al. 2022). Both propanal (starless core TMC-1; Agúndez et al. 2023) and propanol (Galactic Centre; Belloche et al. 2022; Jiménez-Serra et al. 2022) have been securely detected in the gas phase. Figure 12 shows that these three alcohols have absorption features around 6.8, 7.2 and 7.5 μm . However, the relative intensities among these bands for these three molecules are different. For example, ethanol has similar intensities at these three bands, whereas 1-propanol and propanal have different intensities by factors of 3–4. In the case of 1-propanol, the fit of the 7.2 μm band would require twice more absorption at 6.8 μm than observed in IRAS 2A. On the other hand, propanal could contribute to the blue wing of the 7.2 μm band. We highlight, however, that in addition to HCOO^- , NH_2CHO can also contribute

⁴ <http://www1.univap.br/gaa/nkabs-database/S3.txt>

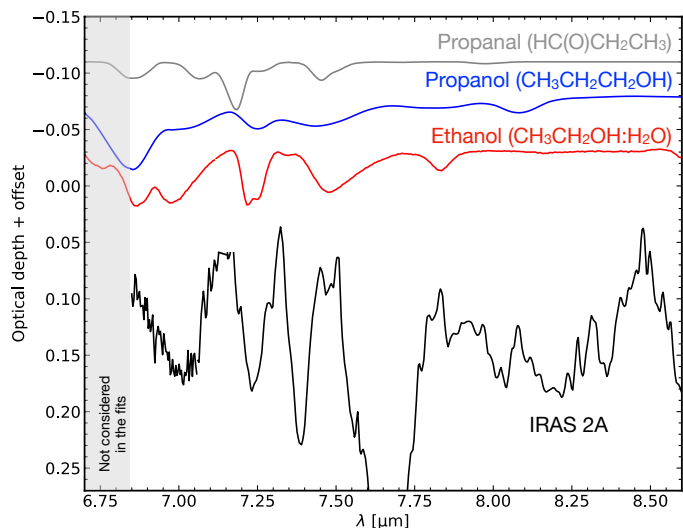


Fig. 12. Experimental IR spectra of ethanol, propanal and propanol compared to IRAS 2A spectrum in the range between 6.8–8.6 μm . The grey area is not considered in the fits, but it is shown here to highlight the C–H stretching mode of these molecules. For better readability of this figure, the gas-phase emission lines between 6.8–7.2 μm are masked.

to the same absorption feature (see Section 4.4 and Figure 10). Another caveat is that both 1-propanol and propanal IR spectra correspond to pure molecules, and therefore spectral differences because of the chemical environment are not perceived in this analysis.

Other than alcohols, hydrocarbons may also contribute to the 7.2 and 7.4 μm bands. In Appendix L, we show a comparison of IRAS 2A spectrum with pure C_2H_2 , C_2H_4 and C_2H_6 around the 7 μm bands and beyond 11 μm . As a result, it can be seen that C_2H_2 and C_2H_6 could contribute to the red wing of the 7.2 μm band. However, their absorption bands longwards of 11 μm exceed the absorption profile in IRAS 2A. Based on these comparisons, the statistical analysis, and different choices for the silicate (Figure B.1) and local continuum (Figure J.1) we can conclude that $\text{CH}_3\text{CH}_2\text{OH}$ is the alcohol that contributes most to the 7.2 μm band in addition to HCOO^- . The systematic analysis of additional high S/N MIRI data is necessary to obtain robust constraints of larger COMs.

5. Discussion

In this section, we discuss the implications of our results from the analysis of the 6.8–8.6 μm region in a low- and high-mass source. This discussion is focused on the presence of simple and neutral species (CH_4 , SO_2 , HCOOH , H_2CO), simple and ionic species (OCN^- , HCOO^-), and complex organic molecules (CH_3CHO , $\text{CH}_3\text{CH}_2\text{OH}$, CH_3OCHO , CH_3COOH). This section ends with a direct comparison between the ice abundances in the low-mass protostar, IRAS 2A, and the ice bulk abundances in comet 67P/G-C. The goal of this comparison is to evaluate the COM inheritance scenario in solar-type protostellar environments. Because of this, we do not perform the same comparison with IRAS 23385.

5.1. Chemical complexity of protostellar ices

In this work, we expand the COMs ice inventory by reporting the detection of at least two vibrational modes of COMs frozen in protostellar ices. We consider secure detections in the cases of

CH_3CHO , $\text{CH}_3\text{CH}_2\text{OH}$, and CH_3OCHO . CH_3COOH also has two vibrational modes and a high recurrence in the degeneracy analysis of IRAS 2A. However, its presence depends on silicate subtraction and local continuum determination and therefore it is considered a tentative detection. This series of molecules are chemically related and strongly supports laboratory experiments and computational simulations that suggest COMs formation in the solid phase. We also note that all these COMs are commonly detected in the gas phase in hot core sources and are among the most abundant ones (e.g., Chen et al. 2023). A detailed comparison between gas and ice abundances is left to a future paper (Chen et al. in prep.). Below we discuss particular aspects of the COMs solid phase detections reported in this work.

5.1.1. A polar ice environment

In both protostars, the CH_3CHO , $\text{CH}_3\text{CH}_2\text{OH}$, and CH_3COOH (continuum-dependent) molecules are diluted in a polar environment (i.e., molecules with high dipole moment), in particular, dominated by H_2O ice. In the general case where H_2O is the major ice component, this means that COM features are under the strong influence of the water ice polarity. In Figure 13, we compare the MIRI observations with the band shape of three COMs in the best fit, the same COMs in an apolar ice matrix, for instance, mixed with CO ice, and finally, in a CH_3OH -rich environment. $\text{CH}_3\text{CH}_2\text{OH}$ mixed with H_2O band shape at 7.25 μm agrees better with the data than the mixture with CO that has narrow and separate bands compared with the observations of IRAS 2A and IRAS 23385. In the case of the IRAS 2A observations, which has a higher signal-to-noise ratio, $\text{CH}_3\text{CH}_2\text{OH}:\text{CO}$ could, potentially, contribute to faint features at 7.16 and 7.29 μm . However, this particular ice mixture is not part of the possible solutions selected by the ENIGMA code. If present, it would have an ice column density one order of magnitude lower than ethanol mixed with water ice. The other mixtures with CH_3OH are less recurrent because of the narrow 7.2 μm and the stronger 7.5 μm that in the global fit makes the 7.2 μm less prominent. In the case of CH_3CHO , the apolar mixture ($\text{CH}_3\text{CHO}:\text{CO}$) makes the CH_3 deformation mode narrow by a factor of 2 and red-shifted by 0.02 μm . In the case of CH_3OH -rich mixtures, the peak is red-shifted by 0.03 μm and the feature is broader.

This result does not necessarily contradict laboratory experiments that show that COMs are formed via hydrogenation of CO molecules (e.g., Fuchs et al. 2009) and C atoms (Fedoseev et al. 2022), as well as that a fraction of CH_3OH ice is mixed with CO (Cuppen et al. 2011). Instead, it points towards a strong effect of H_2O ice on the spectral IR bands of COMs. Moreover, results from the JWST-Ice Age program (McClure et al. 2023), suggest that a fraction of CH_3OH , the most abundant COM, coexists with H_2O in the same ice matrix in cold prestellar clouds. This can be linked to another formation scheme, $\text{CH}_4 + \text{OH}$, as studied by Qasim et al. (2020). Regardless of whether CH_3CHO and $\text{CH}_3\text{CH}_2\text{OH}$ reside in a H_2O - or CH_3OH -rich ice, the important message is that the IR band shapes that resemble better the observations are induced by a polar environment.

Finally, CH_3OCHO seems to be primarily mixed with another polar environment that includes CH_3OH instead of H_2O . The spectral shape of CH_3OCHO mixed with H_2O has a broader profile centred at 8.1 μm which does not match well the observations. From the degeneracy analysis of IRAS 23385, it is not completely excluded as a solution, but in the global fits, the presence of HCOOH discards this component as part of the fit. The mixture with CO creates a sharp peak at 8.25 μm that devi-

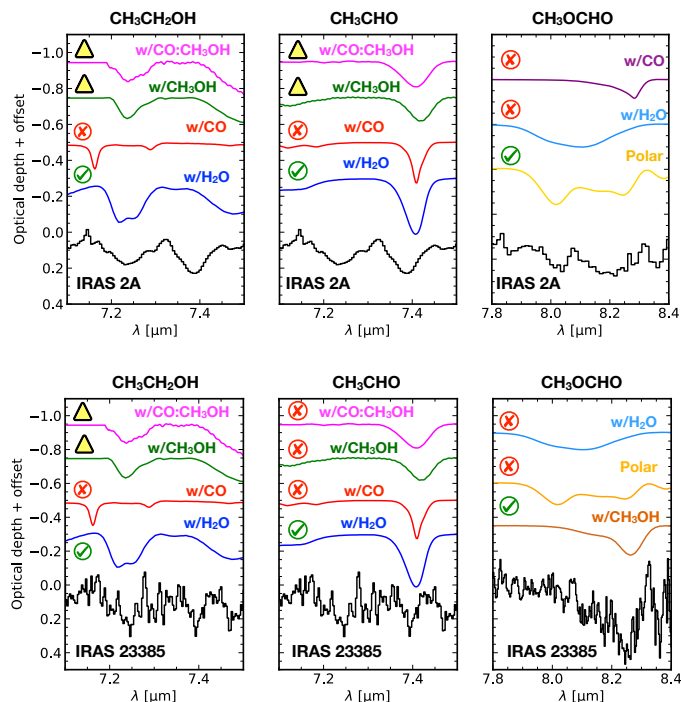


Fig. 13. Comparisons between the IR spectra of COMs in different ice matrices with the observed bands of IRAS 2A (top) and IRAS 23385 (bottom). The green checkmarks indicate the data providing the best fit. Excluded data are given by the red cross. Data not part of the best fit and with lower recurrence are indicated by the yellow triangle. The term “polar” in the right panels refers to CO:H₂CO:CH₃OH and it is the original label published in [Terwisscha van Scheltinga et al. \(2021\)](#).

ates from the observations. The differences between the chemical environment of CH₃CH₂OH and CH₃CHO compared to CH₃OCHO could indicate that methyl formate in IRAS 23385 may have experienced a physical process different from those in IRAS 2A. We discuss this possibility below in Section 5.1.2.

5.1.2. Evidence of ice thermal processing?

Among the ice features identified in this work, CH₃OCHO has different spectral shapes in IRAS 2A and IRAS 23385, regardless of the local continuum choice. While the fit of the IRAS 2A spectrum contains CH₃OCHO mixed with CO:H₂CO:CH₃OH, in IRAS 23385, the CH₃OCHO mixed with CH₃OH provides the best fit, and excludes other solutions (see right panels in Figure 13). A possible cause for this difference can be due to thermal processing, in particular ice distillation. In this process, the most volatile species desorbs from the ice while other species with higher sublimation temperatures remain. For example, during the CH₃OH formation via CO hydrogenation (e.g., [Watanabe & Kouchi 2002](#); [Fuchs et al. 2009](#)) both CH₃O and HCO are formed (e.g., [Chuang et al. 2016](#); [Garrod et al. 2022](#); [Chen et al. 2023](#)), leading to CH₃OCHO. H₂CO is also an intermediate step towards the CH₃OH formation. In a trivial situation, it is expected that at low temperature (< 30 K) CH₃OCHO should be mixed with CO, H₂CO and CH₃OH, the exact components of the ice mixture used to fit the IRAS 2A spectrum. When this ice is warmed up to 50-100 K, CO ice is fully desorbed and H₂CO is partially desorbed, and the ice would be composed mostly of CH₃OCHO and CH₃OH. Because of the low S/N spectrum of IRAS 23385 we cannot definitely conclude if H₂CO is present in the ices toward this source.

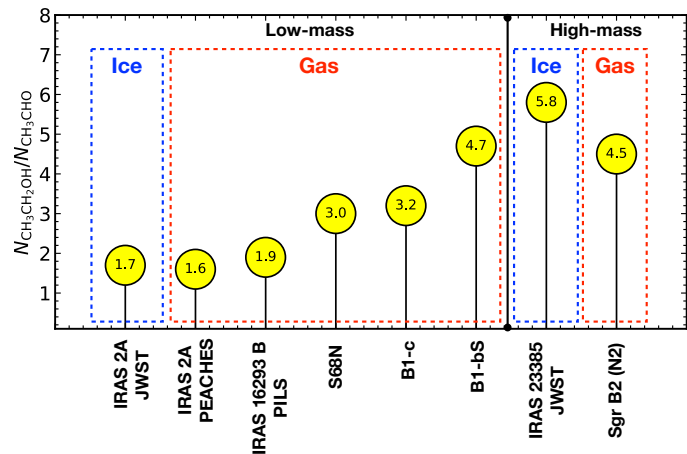


Fig. 14. Ethanol/acetaldehyde ratio in the gas and solid phases towards different sources.

5.1.3. Gas vs. ice: CH₃CH₂OH/CH₃CHO ratio

CH₃CH₂OH and CH₃CHO are chemically linked since the double hydrogenation of acetaldehyde in the solid state leads to ethanol ([Fedoseev et al. 2022](#)). In this regard, the ratio of these two molecules provides a way to understand the hydrogenation efficiency of solid-phase molecules to form larger species in protostars.

Figure 14 compares the inferred CH₃CH₂OH/CH₃CHO ratios in the solid phase with those found in the gas phase of many protostars. A persistent ratio of CH₃CH₂OH and CH₃CHO above the unity has been observed in the gas phase with sensitive observations towards protostars in both low- and high-mass star-forming regions (e.g., [Yang et al. 2021](#); [Jørgensen et al. 2020](#); [van Gelder et al. 2020](#); [Chen et al. 2023](#)). For example, the ratios summarized by [Jørgensen et al. \(2020\)](#) for IRAS 16293B and Sgr(B2) N2 are 1.9 and 4.5, respectively. For low-mass protostars, the CH₃CH₂OH/CH₃CHO ratio taken from [van Gelder et al. \(2020\)](#) are 3.2 (B1-c), 3.0 (S68N), and <4.7 (B1-bS). For the first time, a comprehensive analysis of the 6.8-8.6 μm JWST data allows us to observe the same trend in the solid phase. The CH₃CH₂OH/CH₃CHO ratios derived in this work are 1.7 and 5.8 for IRAS 2A and IRAS 23385, respectively.

This overall trend in protostars suggests that the ethanol/acetaldehyde ratio in the gas phase reflects those in the solid phase. This is a strong hint that ices are the birthplace of COMs detected in the gas phase. Additionally, these COMs are inherited from molecular cloud stages where the ice hydrogenation is efficient to form saturated molecules (e.g., [Fedoseev et al. 2022](#)). We also mention that a full three-phase chemical modelling of these sources, assuming reactions within the bulk of the ice, on the ice surface, and in the gas phase can help us constrain the ice chemistry from the observed ice column densities, and provide a more complete explanation for the ethanol/acetaldehyde ratio in both gas and solid-phase. In fact, recent three-phase chemical modelling work by [Garrod et al. \(2022\)](#) assuming general physical conditions of molecular clouds during collapse and warm-up as well as with non-diffusive ice chemistry confirms that the solid-and gas-phase ratios of ethanol/acetaldehyde are consistent with the results presented in this paper.

5.2. Ions in icy grain mantles

The presence of ions in interstellar ices has long been proposed in the literature as a result of the energetic processing of ice mantles (e.g., Grim & Greenberg 1987; Strazzulla & Palumbo 1998; Allamandola et al. 1988; Martinez et al. 2014; Pilling et al. 2010) and acid-base reactions (e.g., Novozamsky et al. 2001). Among these ions, OCN^- has been detected in several protostellar envelopes (e.g., van Broekhuizen et al. 2005), and recently with JWST in the Chameleon I molecular cloud towards background stars (McClure et al. 2023). Other ions, such as HCOO^- , were proposed as one of the carriers of the 7.2 and 7.4 μm by Schutte et al. (1999) based on the IR peak position.

In the analysis presented in this work, we find that both HCOO^- and OCN^- are important contributors to signals in the range between 6.8–8.6 μm . In particular, an important aspect to highlight regarding HCOO^- is the same relative intensities of the 7.2 and 7.4 μm bands at low temperature (see Appendix H), which is considered the main carrier of the absorption profiles in the two protostars presented in this work. The fact that higher temperature HCOO^- profiles do not match well the observations indicates that the acid-base reaction occurs in cold regions of the protostellar envelope without further thermal processing. One could argue that the HCOO^- profile at 14 K is degenerate with the data at 150 K as seen in Appendix H. However, the full IR spectrum of HCOO^- has an intense peak at 6.3 μm that is around 8 times stronger than the 7.2 and 7.4 μm bands, and therefore can not be the main carrier of those bands. This strongly suggests that acid-base reactions occur in IRAS 2A and IRAS 23385 and that ions cannot be neglected when interpreting the IR observations.

The formation of HCOO^- can occur via the acid-base reaction involving $\text{H}_2\text{O}:\text{HCOOH}:\text{NH}_3$. This is explained by theoretical calculations of $\text{HCOOH}(\cdot\text{H}_2\text{O})_n$ clusters (Park & Woon 2006). In particular, formic acid partially ionizes when mixed with H_2O , forming HCOO^- and H_3O^+ via proton exchange (Theule et al. 2011). Another reaction to form HCOO^- was studied by Bergner et al. (2016), in which only HCOOH and NH_3 are present in the ice, without any H_2O .

Similar to HCOO^- , OCN^- is efficiently formed via acid-base reaction, which has been studied in laboratory experiments starting with HNCO and NH_3 (Schutte & Khanna 2003; Raunier et al. 2003; van Broekhuizen et al. 2004). A large fraction of OCN^- is produced in these experiments, as well as the counter ion, NH_4^+ to maintain the electric neutrality. A possible difficulty in this approach is the high abundance of HNCO in the ice needed to synthesize OCN^- , associated with the non-detection of this molecule in ices yet. However, gas-phase observations (e.g., Hernández-Gómez et al. 2019) show high abundances of HNCO and laboratory experiments in the ice by Fedoseev et al. (2015) and Noble et al. (2015) show that HNCO can be rapidly formed via an exothermic solid-phase reaction between NH and CO . Additionally, the non-detection of HNCO in ices (e.g., McClure et al. 2023) could be related to the low abundance after being converted into OCN^- . The presence of OCN^- and HNCO in ices has a strong astrobiological appeal. HNCO participates as a peptide bond between two single amino acids as shown by Fedoseev et al. (2015). Moreover, irradiation experiments of ice samples containing OCN^-/HNCO would lead to the formation of amino acids and their anions, as well. Finally, we highlight that although NH_4^+ is one of the byproducts of this acid-base reaction, it does not contribute to the absorption bands covered in this work, and therefore, it is not discussed here.

Another mechanism for the OCN^- formation is via UV irradiation (van Broekhuizen et al. 2005), which is discussed as being less dominant in low-mass protostars. This route requires high UV fluxes and an abundance of around 30% of NH_3 in the ice. The former condition is satisfied for high-mass protostars, but not otherwise. In fact, a recent paper by Onaka et al. (2022) shows a clear correlation in the high-mass-source AFGL 2006 between the OCN^- ice column density with the flux intensity of the $\text{HI Br}\alpha$ line. This hydrogen recombination line is a tracer of strong UV radiation and supports an OCN^- formation induced by UV photons. Other mechanisms, such as UV-induced flux by cosmic rays are not enough to produce significant amounts of OCN^- , and low-mass stellar UV would not reach the regions where ice is located. The latter condition exceeds the abundances estimated in the literature for both low- and high-mass protostars, which is between 2% and 15% (Bottinelli et al. 2010).

5.3. Similarities and differences between IRAS 2A, IRAS 23385 and the Comet 67P/G-C

Gas-phase comparisons between the abundances of CHO-bearing COMs with respect to CH_3OH in low- and high-mass protostars, and with the bulk composition of the comet 67P/G-C were made by Drozdovskaya et al. (2019) and Jørgensen et al. (2020). The main conclusion is that there is a good correlation between the abundances of gas-phase COMs in high- and low-mass star-forming regions. On the other hand, there are also differences between the low-mass protostar (IRAS 16293B) and the comet 67P/G-C. In particular, the COMs abundances onto the comet 67P/G-C are enhanced by a factor of up to 10. This difference is interpreted as ice inheritance followed by chemical alteration towards later protostellar phases.

In Figure 15, we show a comparison between the ice CHO-bearing COMs abundances in IRAS 2A and in the comet 67P/G-C, both with respect to methanol ice. We stress that the peak of the methanol band in IRAS 2A is saturated, and the comparisons are made by assuming that the real methanol ice column density is higher by a factor of 2–3 based on the wings of the C–O band at 9.74 μm (see Appendix K). Under this assumption, we see that COMs and the volatile CH_4 correlate well with the cometary abundances within a factor of 5. This agrees with previous conclusions that these COMs are inherited by comets from early protostellar stages. The scatter, however, can be attributed to further chemical alteration at later stages, or slightly different initial composition in the parental molecular cloud. It is also interesting that the volatiles, CH_4 and SO_2 are enriched in the comet 67P/G-C. This could indicate that these molecules are also formed in the gas phase and condensed at later stages in the comet. However, more analysis of other JWST observations is needed to draw strong conclusions from this correlation.

In Figure 16, we show a comparison between the COMs abundances with respect to H_2O ice in IRAS 2A, IRAS 23385 and the comet 67P/G-C. The abundances in the low- and high-mass protostar are very close to a linear correlation, which agrees with the results from Jørgensen et al. (2020) between IRAS 16293B and Sgr B2(N2). On the other hand, the COMs abundances compared to H_2O ice are lower in the comet 67P/G-C than in IRAS 2A. Such a high abundance of molecules in low-mass protostars with respect to H_2O ice was noticed before for other molecules, such as NH_3 (Kawakita & Mumma 2011), and CO , CH_4 and CH_3OH (Öberg et al. 2011). The reason is unclear, but it can indicate selective ice destruction of these species compared to H_2O ice in the protosolar nebula or that those COMs

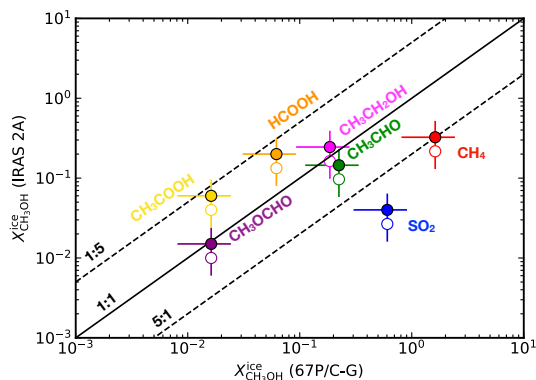


Fig. 15. Comparison between ice abundances with respect to CH_3OH ice in IRAS 2A and the comet 67P/G-C (Rubin et al. 2019). Full and hollow circles show the abundances considering $N_{\text{CH}_3\text{OH}}^{\text{ice}} = 1.5 \times 10^{18} \text{ cm}^{-2}$ and $1.3 \times 10^{18} \text{ cm}^{-2}$, respectively. The solid line indicates the 1:1 abundance relation, and the dashed lines indicate a cometary abundance lower and higher by a factor of 5.

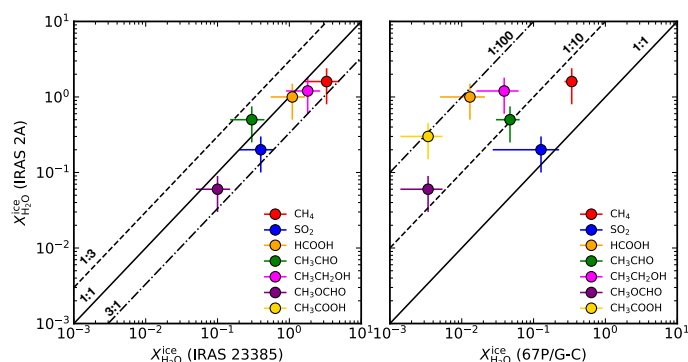


Fig. 16. Comparison between ice abundances with respect to H_2O ice. The left panel shows the ice abundances in IRAS 2A and IRAS 23385. The solid line indicates the 1:1 abundance relation, whereas the dashed and dot-dashed lines indicate the enhancement and diminution of IRAS 23385 abundance by a factor of 3. The right panel compares the ice abundances between IRAS 2A and the comet 67P/G-C from Rubin et al. (2019). The solid line indicates the same as in the left panel. The dot-dashed and dashed lines indicate a cometary abundance lower by a factor of 10 and 100, respectively.

1412 were formed in a carbon-poor protostellar envelope (Öberg et al.
1413 2011).

1414 6. Conclusions

1415 This paper presents a comprehensive analysis in the range
1416 between 6.8–8.6 μm of JWST spectra observed towards the
1417 IRAS 2A and IRAS 23385 protostars. We perform spectral fits
1418 exploring a vast number of IR laboratory spectra that cover, simple
1419 molecules, ions and COMs. The main conclusions are summarised
1420 below:

- 1421 – The 7.7 μm band is fully resolved in the MIRI spectrum
1422 of IRAS 2A and IRAS 23385. As found in previous studies,
1423 CH_4 ice is the main carrier of this band. In addition to
1424 CH_4 , our analysis shows that OCN^- and SO_2 contribute
1425 to the blue wing of the 7.7 μm band. SO_2 was tentatively
1426 detected based on *ISO* and *Spitzer* observations, and based on a
1427 statistical analysis we confirm that SO_2 is present in ices
1428 towards IRAS 2A. For IRAS 23385, SO_2 is classified as likely
1429 detection because of a lower S/N and statistical arguments.

In the case of OCN^- , this is the first time that this ion is
1430 attributed to the 7.7 μm band. Besides the statistical analy-
1431 sis confirming this detection, OCN^- is also seen at 4.59 μm
1432 in IRAS 2A with NIRSpc observation, thus confirming the
1433 feature at 7.7 μm .
1434

- The 7.2 and 7.4 μm bands observed in IRAS 2A and
1435 IRAS 23385 are mainly due to the formate ion (HCOO^-).
1436 Since this ion is efficiently formed via acid-base reactions,
1437 and given the detection of OCN^- at 7.65 μm , these results
1438 demonstrate that this type of chemical reaction may be rather
1439 common in interstellar ices.
1440
- The earlier suggestions that $\text{CH}_3\text{CH}_2\text{OH}$ (ethanol) and
1441 CH_3CHO (acetaldehyde) contribute to the absorption pro-
1442 files at 7.2 and 7.4 μm , respectively, are confirmed in this
1443 work. In addition, we find that $\text{CH}_3\text{CH}_2\text{OH}$ contributes to
1444 other bands in the range considered in this work, most no-
1445 tably, at 6.8–7.05 μm and 7.4–7.6 μm . Other possibilities,
1446 such as hydrocarbons (C_2H_2 , C_2H_4 , C_2H_6) and more com-
1447 plex alcohols (1-propanol, propanal) are less likely based on
1448 their absorption profiles. In the case of CH_3CHO , it also con-
1449 tributes to the range between 6.9–7.2 μm .
1450
- We find robust evidence that CH_3OCHO is present in the
1451 ices towards IRAS 2A and IRAS 23385. At least two strong
1452 bands of this molecule are found between 8.1–8.35 μm and
1453 8.45–8.6 μm . The statistical analysis shows that this spectral
1454 component cannot be excluded as a solution for the fit. Based
1455 on the criteria for a firm identification, CH_3OCHO is classi-
1456 fied as a secure detection. We also find that another COM,
1457 CH_3COOH (acetic acid), is present in the fits of IRAS 2A
1458 and cannot be excluded based on the confidence interval
1459 analysis for two out of three choices of continuum. However,
1460 since it is not found in IRAS 23385, and the local continuum
1461 strongly affects the shape of the bands around 7.8 μm , we
1462 classify acetic acid only as a likely detection. More compar-
1463 isons with other JWST data will elucidate at which level if
1464 acetic acid is present in interstellar ices.
1465
- The COMs found in this work are likely mixed in a polar en-
1466 vironment. For example, $\text{CH}_3\text{CH}_2\text{OH}$ and CH_3CHO fit bet-
1467 ter the observations when mixed with H_2O . These molecules
1468 mixed with CO have spectral profiles that deviate from the
1469 observed protostellar. In the case of CH_3COOH , the mixture
1470 with H_2O ice also provides a good fit to the IRAS 2A spec-
1471 trum. In the case of CH_3OCHO , the two protostars show dif-
1472 ferent spectral shapes. This differentiation could be related
1473 to ice distillation in IRAS 23385, the high-mass protostar.
1474
- Ice-gas ratios between $\text{CH}_3\text{CH}_2\text{OH}$ and CH_3CHO show val-
1475 ues above unity in both gas and ice phases. This suggests
1476 solid-phase reactions for the formation of these molecules.
1477 In addition, the high abundance of $\text{CH}_3\text{CH}_2\text{OH}$ shows that
1478 saturated molecules efficiently form in ices because of the
1479 high amount of hydrogen available.
1480
- For the first time, we compare ice COMs abundances relative
1481 to CH_3OH ice in a protostar and the comet 67P/G-C. Our
1482 results indicate that the COMs ice abundances in the comet
1483 67P/G-C correlate well with those in the protostar within a
1484 factor of 5, which strongly suggests that COMs in comets are
1485 significantly inherited from earlier protostellar phases. In the
1486 case of CH_4 and SO_2 with respect to CH_3OH ice, we find an
1487 enhancement in the comet 67P/G-C. On the other hand, the
1488 abundance comparison with respect to H_2O ice shows that
1489 the COMs, SO_2 and CH_4 are depleted in the comet.
1490

The results presented in this paper illustrate how JWST,
1491 aided by laboratory experiments, is fully capable of probing the
1492

chemical complexity in interstellar ices. Future work using more JWST data with high S/N (e.g., IRAS 15398; Yang et al. 2022) will enable us to verify the recurrence of the COMs found in this paper in other sources, and consequently, assess the robustness of these detections. Another outlook would be the determination of ice-gas ratios of COMs more complex than CH₃OH. Ultimately, an analysis based on a large sample will help us to further answer the question: to what extent chemical complexity can be reached in interstellar ices?

Acknowledgements. The following National and International Funding Agencies funded and supported the MIRI development: NASA; ESA; Belgian Science Policy Office (BELSPO); Centre Nationale d'Études Spatiales (CNES); Danish National Space Centre; Deutsches Zentrum für Luft- und Raumfahrt (DLR); Enterprise Ireland; Ministerio De Economía y Competitividad; The Netherlands Research School for Astronomy (NOVA); The Netherlands Organisation for Scientific Research (NWO); Science and Technology Facilities Council; Swiss Space Office; Swedish National Space Agency; and UK Space Agency. We thank the anonymous reviewer for the careful reading of our manuscript and the comments and suggestions that improved the clarity of this work. WRMR, EvD, K.S, N.B, McG, L.F and HL acknowledge the funding from the European Research Council (ERC) under the European Union's Horizon 2020 research and innovation programme (grant agreement No. 291141 MOLDISK). WRMR thanks Niels Ligterink and Maria Drozdovskaya for useful discussions about the 67P/G-C comet abundances. We are grateful for continuing support through NOVA, the Netherlands Research School for Astronomy, the NWO through its Dutch Astrochemistry Program (DANII). The present work is closely connected to ongoing research within INTERCAT, the Center for Interstellar Catalysis located in Aarhus, Denmark. L.M. acknowledges the financial support of DAE and DST-SERB research grants (SRG/2021/002116 and MTR/2021/000864) from the Government of India. T.R. acknowledges support from ERC grant no. 743029 EASY. T.H. acknowledges support from the ERC Advanced grant no. Origins 83 24 28. H.B. acknowledges support from the Deutsche Forschungsgemeinschaft in the Collaborative Research Center (SFB 881) "The Milky Way System" (sub-project B1). P.J.K. acknowledges financial support from the Science Foundation Ireland/Irish Research Council Pathway programme under Grant Number 21/PATH-S/9360. A.C.G. has been supported by PRIN-INAF MAIN-STREAM 2017 "Protoplanetary disks seen through the eyes of new generation instruments" and from PRIN-INAF 2019 "Spectroscopically tracing the disk dispersal evolution (STRADE)". K.J. acknowledges the support from the Swedish National Space Agency (SNSA).

References

- Adams, F. C., Lada, C. J., & Shu, F. H. 1987, *ApJ*, 312, 788
- Agúndez, M., Loison, J. C., Hickson, K. M., et al. 2023, *A&A*, 673, A34
- Allamandola, L. J., Sandford, S. A., & Valero, G. J. 1988, *Icarus*, 76, 225
- Argyriou, I., Glasse, A., Law, D. R., et al. 2023, *A&A*, 675, A111
- Avni, Y. & Bahcall, J. N. 1980, *ApJ*, 235, 694
- Baeck, T., Fogel, D., & Michalewicz, Z. 2000, *Evolutionary Computation 2: Advanced Algorithms and Operators*, Evolutionary computation (Taylor & Francis)
- Balucani, N., Ceccarelli, C., & Taquet, V. 2015, *MNRAS*, 449, L16
- Belloche, A., Garrod, R. T., Zingsheim, O., Müller, H. S. P., & Menten, K. M. 2022, *A&A*, 662, A110
- Belloche, A., Maury, A. J., Maret, S., et al. 2020, *A&A*, 635, A198
- Bergner, J. B., Öberg, K. I., Garrod, R. T., & Graninger, D. M. 2017, *ApJ*, 841, 120
- Bergner, J. B., Öberg, K. I., Rajappan, M., & Fayolle, E. C. 2016, *ApJ*, 829, 85
- Berné, O., Martin-Drumel, M.-A., Schroetter, I., et al. 2023, *Nature*, 621, 56
- Beuther, H., van Dishoeck, E. F., Tychoniec, L., et al. 2023, *A&A*, 673, A121
- Bisschop, S. E., Fuchs, G. W., Boogert, A. C. A., van Dishoeck, E. F., & Linnartz, H. 2007, *A&A*, 470, 749
- Blake, G. A., Sutton, E. C., Masson, C. R., & Phillips, T. G. 1987, *ApJ*, 315, 621
- Boogert, A. C. A., Brewer, K., Brittain, A., & Emerson, K. S. 2022, *ApJ*, 941, 32
- Boogert, A. C. A., Gerakines, P. A., & Whittet, D. C. B. 2015, *ARA&A*, 53, 541
- Boogert, A. C. A., Huard, T. L., Cook, A. M., et al. 2011, *ApJ*, 729, 92
- Boogert, A. C. A., Pontoppidan, K. M., Knez, C., et al. 2008, *ApJ*, 678, 985
- Boogert, A. C. A., Schutte, W. A., Helmich, F. P., Tielens, A. G. G. M., & Wooden, D. H. 1997, *A&A*, 317, 929
- Bottinelli, S., Boogert, A. C. A., Bouwman, J., et al. 2010, *ApJ*, 718, 1100
- Bottinelli, S., Ceccarelli, C., Williams, J. P., & Lefloch, B. 2007, *A&A*, 463, 601
- Boudin, N., Schutte, W. A., & Greenberg, J. M. 1998, *A&A*, 331, 749
- Bouilloud, M., Fray, N., Bénilan, Y., et al. 2015, *MNRAS*, 451, 2145
- Bouwman, J., Ludwig, W., Awad, Z., et al. 2007, *A&A*, 476, 995
- Brinch, C., Jørgensen, J. K., & Hogerheijde, M. R. 2009, *A&A*, 502, 199
- Brönsted, J. N. 1923, *Recueil des Travaux Chimiques des Pays-Bas*, 42, 718
- Bushouse, H., Eisenhamer, J., Dencheva, N., et al. 2022, *spacetelescope/jwst: JWST 1.6.2*, Zenodo
- Casoli, F., Dupraz, C., Gerin, M., Combes, F., & Boulanger, F. 1986, *A&A*, 169, 281
- Cazaux, S., Tielens, A. G. G. M., Ceccarelli, C., et al. 2003, *ApJ*, 593, L51
- Cesaroni, R., Beuther, H., Ahmadi, A., et al. 2019, *A&A*, 627, A68
- Chen, Y., van Gelder, M. L., Nazari, P., et al. 2023, *A&A*, 678, A137
- Chiar, J. E. & Tielens, A. G. G. M. 2006, *ApJ*, 637, 774
- Chu, L. E. U., Hodapp, K., & Boogert, A. 2020, *ApJ*, 904, 86
- Chuang, K. J., Fedoseev, G., Ioppolo, S., van Dishoeck, E. F., & Linnartz, H. 2016, *MNRAS*, 455, 1702
- Chuang, K. J., Fedoseev, G., Qasim, D., et al. 2020, *A&A*, 635, A199
- Colzi, L., Rivilla, V. M., Beltrán, M. T., et al. 2021, *A&A*, 653, A129
- Coutens, A., Persson, M. V., Jørgensen, J. K., Wampfler, S. F., & Lykke, J. M. 2015, *A&A*, 576, A5
- Cuppen, H. M., Penteado, E. M., Isokoski, K., van der Marel, N., & Linnartz, H. 2011, *MNRAS*, 417, 2809
- Dartois, E., Schutte, W., Geballe, T. R., et al. 1999, *A&A*, 342, L32
- Dartois, E., Thi, W. F., Geballe, T. R., et al. 2003, *A&A*, 399, 1009
- De Simone, M., Codella, C., Testi, L., et al. 2017, *A&A*, 599, A121
- Do-Duy, T., Wright, C. M., Fujiyoshi, T., et al. 2020, *MNRAS*, 493, 4463
- Domínik, C., Min, M., & Tazaki, R. 2021, *OpTool: Command-line driven tool for creating complex dust opacities*
- Dorschner, J., Begemann, B., Henning, T., Jaeger, C., & Mutschke, H. 1995, *A&A*, 300, 503
- Drozdovskaya, M. N., van Dishoeck, E. F., Rubin, M., Jørgensen, J. K., & Alltwegg, K. 2019, *MNRAS*, 490, 50
- Ehrenfreund, P., Bernstein, M. P., Dworkin, J. P., Sandford, S. A., & Allamandola, L. J. 2001, *ApJ*, 550, L95
- Fedoseev, G., Ioppolo, S., Zhao, D., Lamberts, T., & Linnartz, H. 2015, *MNRAS*, 446, 439
- Fedoseev, G., Qasim, D., Chuang, K.-J., et al. 2022, *ApJ*, 924, 110
- Fuchs, G. W., Cuppen, H. M., Ioppolo, S., et al. 2009, *A&A*, 505, 629
- Gálvez, O., Maté, B., Herrero, V. J., & Escribano, R. 2010, *ApJ*, 724, 539
- Garrod, R. T., Jin, M., Matis, K. A., et al. 2022, *ApJS*, 259, 1
- Geballe, T. R. 1984, *Occasional Reports of the Royal Observatory Edinburgh*, 12, 56
- Gerakines, P. A., Schutte, W. A., & Ehrenfreund, P. 1996, *A&A*, 312, 289
- Gibb, E. L., Whittet, D. C. B., Boogert, A. C. A., & Tielens, A. G. G. M. 2004, *ApJS*, 151, 35
- Gieser, C., Beuther, H., Semenov, D., et al. 2021, *A&A*, 648, A66
- Gieser, C., Beuther, H., van Dishoeck, E. F., et al. 2023, *arXiv e-prints*, arXiv:2309.10410
- Greenfield, P. & Miller, T. 2016, *Astronomy and Computing*, 16, 41
- Grim, R. J. A., Baas, F., Geballe, T. R., Greenberg, J. M., & Schutte, W. A. 1991, *A&A*, 243, 473
- Grim, R. J. A. & Greenberg, J. M. 1987, *ApJ*, 321, L91
- Harris, C. R., Millman, K. J., van der Walt, S. J., et al. 2020, *Nature*, 585, 357
- Herbst, E. & van Dishoeck, E. F. 2009, *ARA&A*, 47, 427
- Hernández-Gómez, A., Sahnoun, E., Caux, E., et al. 2019, *MNRAS*, 483, 2014
- Holland, J. H. 1975, *Adaptation in natural and artificial systems: an introductory analysis with applications to biology, control, and artificial intelligence* (Ann Arbor: University of Michigan Press)
- Holtom, P. D., Bennett, C. J., Osamura, Y., Mason, N. J., & Kaiser, R. I. 2005, *ApJ*, 626, 940
- Hudgins, D. M., Sandford, S. A., Allamandola, L. J., & Tielens, A. G. G. M. 1993, *ApJS*, 86, 713
- Hudson, R. L. & Ferrante, R. F. 2020, *MNRAS*, 492, 283
- Hudson, R. L., Ferrante, R. F., & Moore, M. H. 2014a, *Icarus*, 228, 276
- Hudson, R. L. & Gerakines, P. A. 2019, *MNRAS*, 485, 861
- Hudson, R. L., Gerakines, P. A., & Moore, M. H. 2014b, *Icarus*, 243, 148
- Hudson, R. L., Loeffler, M. J., Ferrante, R. F., Gerakines, P. A., & Coleman, F. M. 2020, *ApJ*, 891, 22
- Hudson, R. L., Moore, M. H., & Cook, A. M. 2005, *Advances in Space Research*, 36, 184
- Ioppolo, S., Fedoseev, G., Chuang, K. J., et al. 2021, *Nature Astronomy*, 5, 197
- Jiménez-Serra, I., Rodríguez-Almeida, L. F., Martín-Pintado, J., et al. 2022, *A&A*, 663, A181
- Jørgensen, J. K., Belloche, A., & Garrod, R. T. 2020, *ARA&A*, 58, 727
- Jørgensen, J. K., Bourke, T. L., Myers, P. C., et al. 2005, *ApJ*, 632, 973
- Kawakita, H. & Mumma, M. J. 2011, *ApJ*, 727, 91
- Koza, J. R. 1992, *Genetic programming: on the programming of computers by means of natural selection*, Complex adaptive systems. 09800994X (Cambridge, MA [etc.]: The MIT Press)
- Kruczkiewicz, F., Vitorino, J., Congiu, E., Theulé, P., & Dulieu, F. 2021, *A&A*, 652, A29
- Kurtz, S., Hofner, P., & Álvarez, C. V. 2004, *ApJS*, 155, 149

- 1645 Labiano, A., Argyriou, I., Álvarez-Márquez, J., et al. 2021, *A&A*, 656, A57
- 1646 Lacy, J. H., Carr, J. S., Evans, Neal J., I., et al. 1991, *ApJ*, 376, 556
- 1647 Ligterink, N. F. W., Ahmadi, A., Luitel, B., et al. 2022, *ACS Earth and Space Chemistry*, 6, 455
- 1648 Looney, L. W., Mundy, L. G., & Welch, W. J. 2000, *ApJ*, 529, 477
- 1649 Lowry, T. M. 1923, *Journal of the Society of Chemical Industry*, 42, 43
- 1650 Manigand, S., Jørgensen, J. K., Calcutt, H., et al. 2020, *A&A*, 635, A48
- 1651 Marechal, Y. 1987, *J. Chem. Phys.*, 87, 6344
- 1652 Martínez, R., Bordalo, V., da Silveira, E. F., & Boechat-Roberty, H. M. 2014, *MNRAS*, 444, 3317
- 1653 Maté, B., Herrero, V. J., Rodríguez-Lazcano, Y., et al. 2012, *ApJ*, 759, 90
- 1654 McClure, M. K., Rocha, W. R. M., Pontoppidan, K. M., et al. 2023, *Nature Astronomy*, 7, 431
- 1655 Min, M., Hovenier, J. W., & de Koter, A. 2005, *A&A*, 432, 909
- 1656 Molinari, S., Faustini, F., Testi, L., et al. 2008, *A&A*, 487, 1119
- 1657 Molinari, S., Testi, L., Brand, J., Cesaroni, R., & Palla, F. 1998, *ApJ*, 505, L39
- 1658 Morbidelli, A., Karato, S.-I., Ikoma, M., et al. 2018, *Space Sci. Rev.*, 214, 110
- 1659 Morbidelli, A., Lunine, J. I., O'Brien, D. P., Raymond, S. N., & Walsh, K. J. 2012, *Annual Review of Earth and Planetary Sciences*, 40, 251
- 1660 Moreno, M. A., Maté, B., Rodríguez-Lazcano, Y., et al. 2013, *Journal of Physical Chemistry A*, 117, 9564
- 1661 Nazari, P., van Gelder, M. L., van Dishoeck, E. F., et al. 2021, *A&A*, 650, A150
- 1662 Noble, J. A., Theule, P., Congiu, E., et al. 2015, *A&A*, 576, A91
- 1663 Novozamsky, J. H., Schutte, W. A., & Keane, J. V. 2001, *A&A*, 379, 588
- 1664 Öberg, K. I., Boogert, A. C. A., Pontoppidan, K. M., et al. 2008, *ApJ*, 678, 1032
- 1665 Öberg, K. I., Boogert, A. C. A., Pontoppidan, K. M., et al. 2011, *ApJ*, 740, 109
- 1666 Öberg, K. I., Bottinelli, S., & van Dishoeck, E. F. 2009a, *A&A*, 494, L13
- 1667 Öberg, K. I., Fraser, H. J., Boogert, A. C. A., et al. 2007, *A&A*, 462, 1187
- 1668 Öberg, K. I., Garrod, R. T., van Dishoeck, E. F., & Linnartz, H. 2009b, *A&A*, 504, 891
- 1669 O'Brien, D. P., Izidorio, A., Jacobson, S. A., Raymond, S. N., & Rubie, D. C. 2018, *Space Sci. Rev.*, 214, 47
- 1670 Onaka, T., Sakon, I., & Shimonishi, T. 2022, *ApJ*, 941, 190
- 1671 Ortiz-León, G. N., Loinard, L., Dzib, S. A., et al. 2018, *ApJ*, 865, 73
- 1672 Ossenkopf, V. & Henning, T. 1994, *A&A*, 291, 943
- 1673 Park, J.-Y. & Woon, D. E. 2006, *ApJ*, 648, 1285
- 1674 Perotti, G., Jørgensen, J. K., Fraser, H. J., et al. 2021, *A&A*, 650, A168
- 1675 Pilling, S., Andrade, D. P. P., Do Nascimento, E. M., et al. 2011, *MNRAS*, 411, 2214
- 1676 Pilling, S., Seperuelo Duarte, E., Domaracka, A., et al. 2010, *A&A*, 523, A77
- 1677 Poch, O., Istiqomah, I., Quirico, E., et al. 2020, *Science*, 367, aaw7462
- 1678 Pontoppidan, K. M., Dullemond, C. P., van Dishoeck, E. F., et al. 2005, *ApJ*, 622, 463
- 1679 Pontoppidan, K. M., van Dishoeck, E. F., & Dartois, E. 2004, *A&A*, 426, 925
- 1680 Potapov, A., Fulvio, D., Krasnokutski, S., Jäger, C., & Henning, T. 2022, *Journal of Physical Chemistry A*, 126, 1627
- 1681 Poteet, C. A., Whittet, D. C. B., & Draine, B. T. 2015, *ApJ*, 801, 110
- 1682 Qasim, D., Fedoseev, G., Chuang, K. J., et al. 2020, *Nature Astronomy*, 4, 781
- 1683 Qasim, D., Fedoseev, G., Chuang, K. J., et al. 2019, *A&A*, 627, A1
- 1684 Quénard, D., Jiménez-Serra, I., Viti, S., Holdship, J., & Coutens, A. 2018, *MNRAS*, 474, 2796
- 1685 Rachid, M. G., Brunken, N., de Boe, D., et al. 2021, *A&A*, 653, A116
- 1686 Rachid, M. G., Rocha, W. R. M., & Linnartz, H. 2022, *A&A*, 665, A89
- 1687 Rachid, M. G., Terwisscha van Scheltinga, J., Koletzki, D., & Linnartz, H. 2020, *A&A*, 639, A4
- 1688 Raunier, S., Chiavassa, T., Marinelli, F., Allouche, A., & Aycard, J. P. 2003, *Chemical Physics Letters*, 368, 594
- 1689 Reipurth, B., Rodríguez, L. F., Anglada, G., & Bally, J. 2002, *AJ*, 124, 1045
- 1690 Rieke, G. H., Wright, G. S., Böker, T., et al. 2015, *PASP*, 127, 584
- 1691 Rocha, W. & Pilling, S. 2014, *Spectrochimica Acta Part A: Molecular and Biomolecular Spectroscopy*, 123, 436
- 1692 Rocha, W. R. M., Perotti, G., Kristensen, L. E., & Jørgensen, J. K. 2021, *A&A*, 654, A158
- 1693 Rocha, W. R. M., Pilling, S., de Barros, A. L. F., et al. 2017, *MNRAS*, 464, 754
- 1694 Rocha, W. R. M., Rachid, M. G., Olsthoorn, B., et al. 2022, *A&A*, 668, A63
- 1695 Rubin, M., Altwegg, K., Balsiger, H., et al. 2019, *MNRAS*, 489, 594
- 1696 Sandell, G., Kneel, L. B. G., Aspin, C., Robson, I. E., & Russell, A. P. G. 1994, *A&A*, 285, L1
- 1697 Schutte, W. A., Boogert, A. C. A., Tielens, A. G. G. M., et al. 1999, *A&A*, 343, 966
- 1698 Schutte, W. A. & Khanna, R. K. 2003, *A&A*, 398, 1049
- 1699 Shimonishi, T., Onaka, T., Kato, D., et al. 2010, *A&A*, 514, A12
- 1700 Skinner, C. J., Tielens, A. G. G. M., Barlow, M. J., & Justtanont, K. 1992, *ApJ*, 399, L79
- 1701 Skouteris, D., Balucani, N., Ceccarelli, C., et al. 2018, *ApJ*, 854, 135
- 1702 Slavicinska, K., Rachid, M. G., Rocha, W. R. M., et al. 2023, *A&A*, 677, A13
- 1703 Strazzulla, G. & Palumbo, M. E. 1998, *Planet. Space Sci.*, 46, 1339
- 1704 Taquet, V., López-Sepulcre, A., Ceccarelli, C., et al. 2015, *ApJ*, 804, 81
- 1705 Tenelanda-Osorio, L. I., Bouquet, A., Javelle, T., et al. 2022, *MNRAS*, 515, 5009
- 1706 Terwisscha van Scheltinga, J., Ligterink, N. F. W., Boogert, A. C. A., van Dishoeck, E. F., & Linnartz, H. 2018, *A&A*, 611, A35
- 1707 Terwisscha van Scheltinga, J., Marcandalli, G., McClure, M. K., Hogerheijde, M. R., & Linnartz, H. 2021, *arXiv e-prints*, arXiv:2105.02226
- 1708 Theule, P., Duvernay, F., Ilmane, A., et al. 2011, *A&A*, 530, A96
- 1709 Thi, W. F., van Dishoeck, E. F., Dartois, E., et al. 2006, *A&A*, 449, 251
- 1710 Tobin, J. J., Dunham, M. M., Looney, L. W., et al. 2015, *ApJ*, 798, 61
- 1711 van Broekhuizen, F. A., Keane, J. V., & Schutte, W. A. 2004, *A&A*, 415, 425
- 1712 van Broekhuizen, F. A., Pontoppidan, K. M., Fraser, H. J., & van Dishoeck, E. F. 2005, *A&A*, 441, 249
- 1713 van Dishoeck, E. F., Bergin, E. A., Lis, D. C., & Lunine, J. I. 2014, in *Protostars and Planets VI*, ed. H. Beuther, R. S. Klessen, C. P. Dullemond, & T. Henning, 835–858
- 1714 van Dishoeck, E. F., Grant, S., Tabone, B., et al. 2023, *Faraday Discussions*, 245, 52
- 1715 van Dishoeck, E. F., Kristensen, L. E., Mottram, J. C., et al. 2021, *A&A*, 648, A24
- 1716 van Gelder, M. L., Ressler, M. E., van Dishoeck, E. F., et al. 2023, *arXiv e-prints*, in press, arXiv:2311.17161
- 1717 van Gelder, M. L., Tabone, B., Tychoniec, L., et al. 2020, *A&A*, 639, A87
- 1718 Vazart, F., Ceccarelli, C., Balucani, N., & Skouteris, D. 2022, *ApJ*, 941, 196
- 1719 Watanabe, N. & Kouchi, A. 2002, *ApJ*, 571, L173
- 1720 Weingartner, J. C. & Draine, B. T. 2001, *ApJ*, 548, 296
- 1721 Wells, M., Pel, J. W., Glasse, A., et al. 2015, *PASP*, 127, 646
- 1722 Woitke, P., Min, M., Pinte, C., et al. 2016, *A&A*, 586, A103
- 1723 Wright, G. S., Rieke, G. H., Glasse, A., et al. 2023, *PASP*, 135, 048003
- 1724 Wright, G. S., Wright, D., Goodson, G. B., et al. 2015, *PASP*, 127, 595
- 1725 Yang, Y.-L., Green, J. D., Pontoppidan, K. M., et al. 2022, *ApJ*, 941, L13
- 1726 Yang, Y.-L., Sakai, N., Zhang, Y., et al. 2021, *ApJ*, 910, 20
- 1727 Yarnall, Y. Y., Gerakines, P. A., & Hudson, R. L. 2020, *MNRAS*, 494, 4606
- 1728 Zasowski, G., Kemper, F., Watson, D. M., et al. 2009, *ApJ*, 694, 459
- 1729 Zucker, C., Schlafly, E. F., Speagle, J. S., et al. 2018, *ApJ*, 869, 83
- 1730 Öberg, K. I. 2016, *Chemical Reviews*, 116, 9631, pMID: 27099922

-
- ¹ Laboratory for Astrophysics, Leiden Observatory, Leiden University, P.O. Box 9513, NL 2300 RA Leiden, The Netherlands. e-mail: rocha@strw.leidenuniv.nl
- ² Leiden Observatory, Leiden University, PO Box 9513, NL 2300 RA Leiden, The Netherlands
- ³ Max Planck Institut für Extraterrestrische Physik (MPE), Giessenbachstrasse 1, 85748 Garching, Germany
- ⁴ Jet Propulsion Laboratory, California Institute of Technology, 4800 Oak Grove Drive, Pasadena, CA 91109, USA
- ⁵ Dublin Institute for Advanced Studies, Dublin, Ireland
- ⁶ Max Planck Institute for Astronomy, Königstuhl 17, 69117 Heidelberg, Germany
- ⁷ INAF-Osservatorio Astronomico di Capodimonte, Salita Moiarielello 16, 80131 Napoli, Italy
- ⁸ UK Astronomy Technology Centre, Royal Observatory Edinburgh, Blackford Hill, Edinburgh EH9 3HJ, UK
- ⁹ Department of Experimental Physics, Maynooth University, Maynooth, Co Kildare, Ireland
- ¹⁰ Department of Space, Earth and Environment, Chalmers University of Technology, Onsala Space Observatory, 439 92 Onsala, Sweden
- ¹¹ European Southern Observatory, Karl-Schwarzschild-Strasse 2, 85748 Garching bei München, Germany
- ¹² SETI Institute 189 Bernardo Avenue, 2nd Floor, Mountain View, CA 94043, USA
- ¹³ School of Earth and Planetary Sciences, National Institute of Science Education and Research, Jatni 752050, Odisha, India
- ¹⁴ Homi Bhabha National Institute, Training School Complex, Anushaktinagar, Mumbai 400094, India
- ¹⁵ NASA Postdoctoral Program Fellow, NASA Ames Research Center, Moffett Field, CA, USA
- ¹⁶ Bay Area Environmental Research Institute and NASA Ames Research Center, Moffett Field, CA 94035, USA

Appendix A: 9.8 μm band compared to ISO and Spitzer sources

Figures A.1 and A.2 show comparisons with the silicate feature towards GCS 3 and with other low- and high-mass protostars observed with *Spitzer* and *ISO*. The first note is that both IRAS 2A and IRAS 23385 have a broader 9.8 μm silicate profile compared to GCS 3. This highlights the need of considering different grain compositions when subtracting the silicate absorption band. Secondly, IRAS 2A and IRAS 23385 show a similar blue side of the spectrum with other sources. On the other hand, the red profile has more differences, which are related to the amount of H_2O ice towards the source. In fact, icy-grain models by Ossenkopf & Henning (1994) show that coagulated icy grains have a prominent spectral bump around 12 μm because of the H_2O ice libration band.

Appendix B: Effect of using different silicates for subtraction in IRAS 2A

In Section 3.1, we describe how the silicate feature is removed from IRAS 23385 and IRAS 2A MIRI-MRS spectra using a synthetic silicate profile combining olivine and pyroxene. In this section, we compare subtractions using different profiles to check how this step affects the shape of the 6.8–8.6 μm region. Figure B.1 (top) shows three silicate profiles, scaled to IRAS 2A spectrum, i) the synthetic silicate used in Section 3.1, ii) the silicate profile of GCS 3, and iii) the MgSiO_3 profile taken from Poteet et al. (2015). The peak optical depths are set to match the synthetic silicate profile. We point out that this comparison is focused on the 6.8–8.6 μm region, and therefore mismatches of these silicate spectra at longer wavelengths are not relevant for this specific analysis. We briefly mention SiO (silica), as another possible candidate for the blue wing of the 9.8 μm band. However, silica has not been found in absorption in protostars so far and its relatively narrow profile at 18 μm is not seen in both sources investigated in this paper. Nevertheless, if present, SiO would not affect the COMs bands investigated in this paper because of its broadband at around 8.3 μm . At most, it could slightly reduce the HCOOH ice column density.

Figure B.1 (bottom) shows the silicate subtracted optical depth spectrum of IRAS 2A. Both synthetic and enstatite silicates result in similar spectral profiles between 6.8–8.6 μm . On the other hand, the silicate subtraction using GCS 3 creates an unrealistic absorption excess (also observed in Boogert et al. (2008)) that deviates from the other two profiles.

Appendix C: List of laboratory data

A comprehensive list of molecules was used in this paper to search for the best fit of the region between 6.8 and 8.6 μm . This list includes COMs in different mixtures as well as simple molecules. The full list is shown in Table C.1.

Appendix D: Acetic acid and OCN^- band strengths

Most of the band strengths for the molecules detected in the range addressed in this paper are available in the literature. However, to the best of our knowledge, the band strengths of acetic acid and OCN^- between 6.8 and 8.6 μm were not calculated before. In particular, the band strength of acetic acid at 5.8 μm is often assumed to be the same as, or corrected from, the gas-phase acetic acid (e.g., Öberg et al. 2009b; Chuang et al. 2020) based on Marechal (1987).

We derive the absolute (A) and apparent (A') band strengths of acetic acid. The absolute band strengths are derived from the imaginary refractive index, by the following equation:

$$A = \frac{m}{\rho N_A} \int_{\nu_1}^{\nu_2} 4\pi\nu k(\nu) d\nu \quad (\text{D.1})$$

where m is the molar mass of acetic acid in g mol^{-1} (60.052), ρ is the density of acetic acid (0.892 g cm^{-3} ; Hudson et al. 2020), N_A is the Avogadro's number, ν is the wavenumber and k is the imaginary refractive index. We derive k using the recent version of the NKABS code (Rocha & Pilling 2014). This code calculates the real (n) and imaginary (k) refractive index from the absorbance spectrum ($Ab_{s,\nu}$). The input spectrum is taken from Hudson & Gerakines (2019), who also estimated the thickness of the ice ($d = 2.1 \mu\text{m}$) and the refractive index around 700 nm ($n_0 = 1.29$). The n and k values are shown in Figure D.1. Finally, the band strengths derived for two acetic acid bands are listed in Table D.1.

The apparent band strength is calculated by:

$$A' = 2.303 \frac{m}{\rho N_A d} \int Ab_{s,\nu} d\nu \quad (\text{D.2})$$

As one can see, both A and A' values for acetic acid are similar.

In the case of OCN^- , we derive the apparent band strength at 7.62 μm (1312 cm^{-1}). The OCN^- band at 4.59 μm (2175 cm^{-1}) is used as a reference since the band strength is known ($1.3 \times 10^{-16} \text{ cm molecule}^{-1}$; van Broekhuizen et al. 2005). We use the following equation to derive the OCN^- apparent band strength at 7.62 μm :

$$A'_{7.62\mu\text{m}} = 1.3 \times 10^{-16} \frac{\int Ab_{s,1312\text{cm}^{-1}} d\nu}{\int Ab_{s,2175\text{cm}^{-1}} d\nu}, \quad (\text{D.3})$$

where $Ab_{s,2175\text{cm}^{-1}}$ and $Ab_{s,1312\text{cm}^{-1}}$ are the OCN^- bands at the given wavelengths.

Appendix E: Laboratory spectra: removing H_2O and CH_3OH ice features

In this section, we demonstrate how to remove the H_2O and CH_3OH features of COMs spectra containing these two molecules in the range between 6.5 and 9.0 μm . This process is necessary when analysing the observational spectrum between 6.8 and 8.6 μm using local continuum subtraction. Figure E.1 (top) shows the $\text{H}_2\text{O}:\text{CH}_3\text{CH}_2\text{OH}$ ice spectrum (Terwisscha van Scheltinga et al. 2018) and the polynomial (4th-order) function used to trace a baseline under the $\text{CH}_3\text{CH}_2\text{OH}$ bands. In this spectrum, the ethanol features overlap with the broad shoulder of the H_2O ice bending mode, which is represented by the polynomial fit. In Figure E.1 (bottom), we show the $\text{CH}_3\text{OH}:\text{CH}_3\text{CH}_2\text{OH}$ IR spectrum (Terwisscha van Scheltinga et al. 2018). Since both molecules are alcohols they share functional groups, which makes it harder to isolate the ethanol features of methanol. Because of the high dilution factor (20:1), it is not feasible to disentangle the features of the two molecules below 6.8 μm , and therefore, we separate the $\text{CH}_3\text{CH}_2\text{OH}$ bands between 6.9 and 8.6 μm . The step is performed in three stages: (i) high-order polynomial (7th) between 6.9–7.15 μm to remove the CH_3OH shoulder, (ii) 3rd-order polynomial between 7.15–7.45 μm to isolate the ethanol band at 7.2 μm and account for the strong curvature in the data, and (iii) 5th-order polynomial between 7.45–8.7 μm to extract the other ethanol bands.

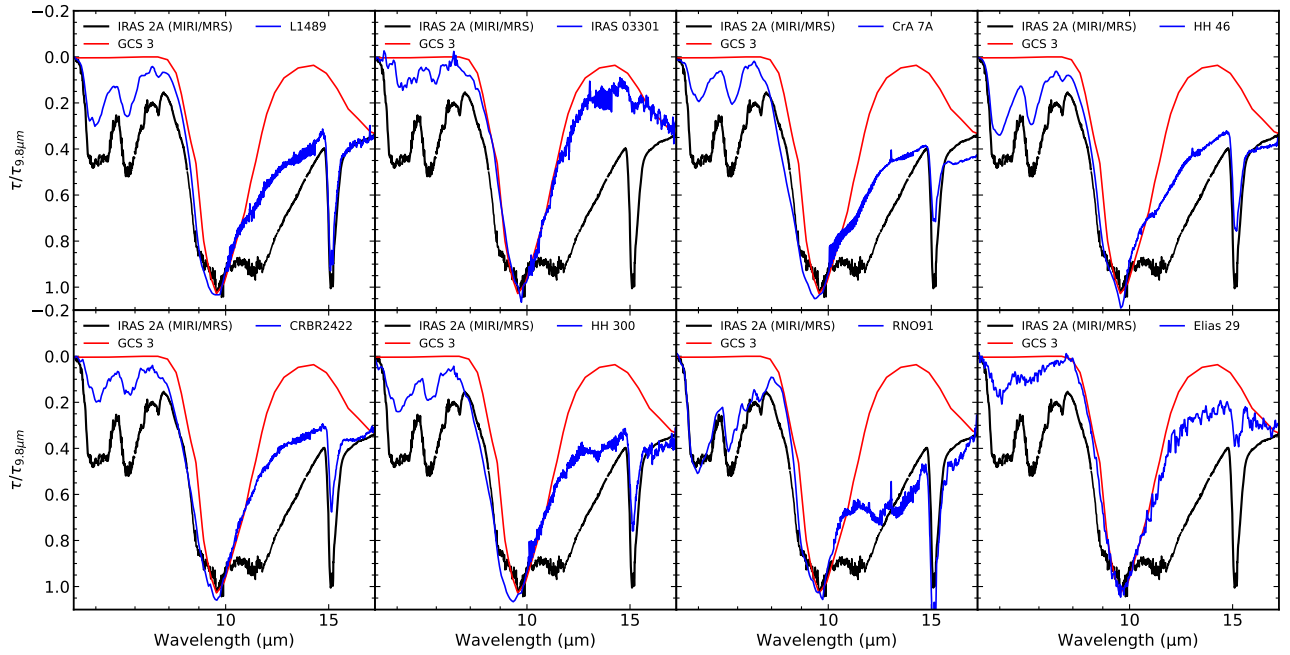


Fig. A.1. Comparison among MIRI/JWST spectrum of IRAS 2A, the silicate profile of GCS 3 and *Spitzer*/IRS spectrum of different low-mass protostars. These spectra are normalized by the optical depth at 9.8 μm .

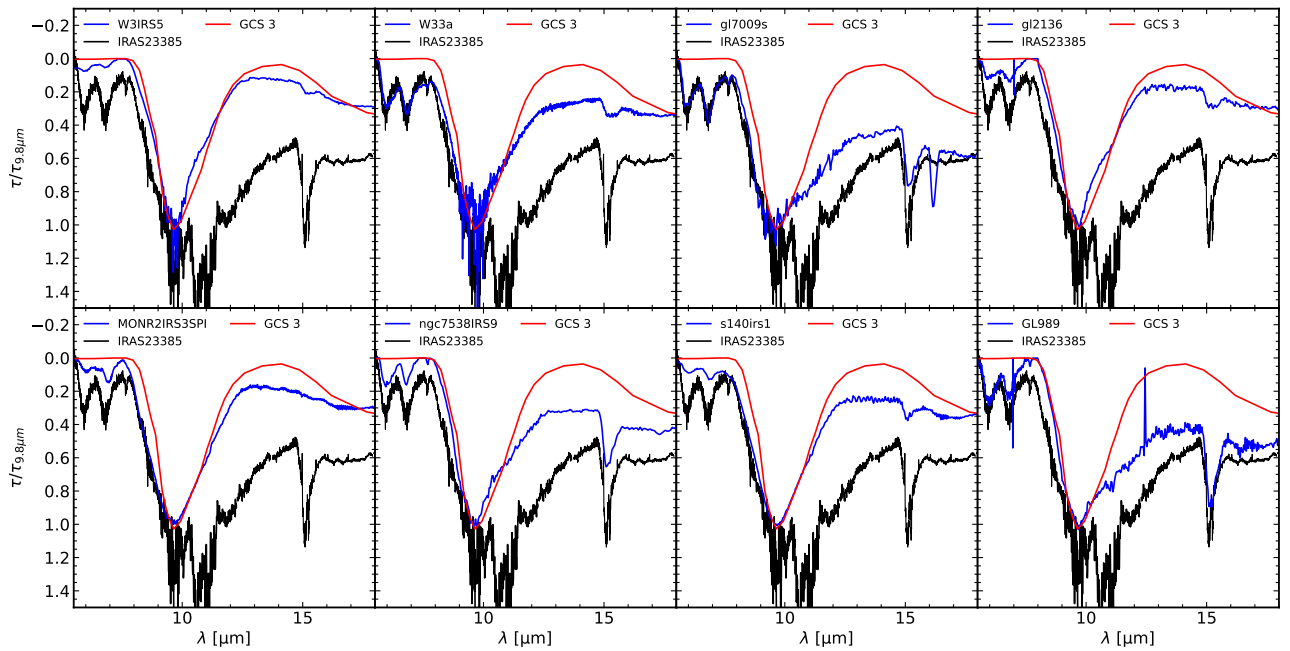


Fig. A.2. Comparison among MIRI/JWST spectrum of IRAS 23385, the silicate profile of GCS 3 and *Spitzer*/IRS spectrum of different low-mass protostars. These spectra are normalized by the optical depth at 9.8 μm .

Appendix F: Laboratory baseline correction: avoiding spurious features

IR spectra of ices are recorded in the laboratory using Fourier Transform Infrared Spectroscopy (FTIR) and interference effects are corrected using a spline or polynomial function, the so-called baseline correction. In Figure F.1 we show the baseline correction of the $\text{H}_2\text{O}:\text{CH}_3\text{CH}_2\text{OH}$ IR spectrum at 15 K. Panels a and b show the laboratory spectrum and a 7th-order polynomial used to correct the interference effect. The difference between these two panels is that in panel a, we use as many points as possi-

ble to trace the baseline, whereas in panel b, we use only half of the points available in the range of 7.8–8.5 μm . This creates a small fluctuation in the polynomial function. Zoom-ins of both cases are shown in panels c and d, respectively. In panel e, we show the baseline data. The spectrum with no polynomial inflexion contains the real $\text{CH}_3\text{CH}_2\text{OH}$ IR features, whereas the other data has spurious features at 8.0 and 8.3 μm . This demonstrates that care must be taken when correcting IR spectrum baselines to avoid creating spurious features.

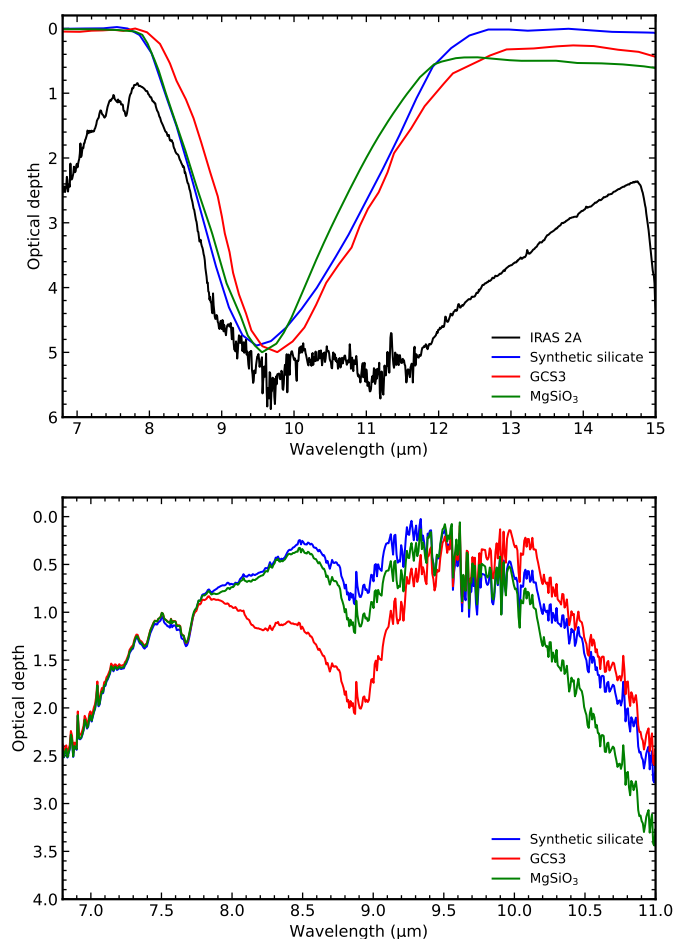


Fig. B.1. Comparing silicate profiles in IRAS 2A. The top panel shows the synthetic silicate providing the best fit in IRAS 2A (blue) compared to GCS 3 (red) and enstatite (green) silicate model from [Poteet et al. \(2015\)](#). The bottom panel shows the IRAS 2A spectrum after removing the three silicate models.

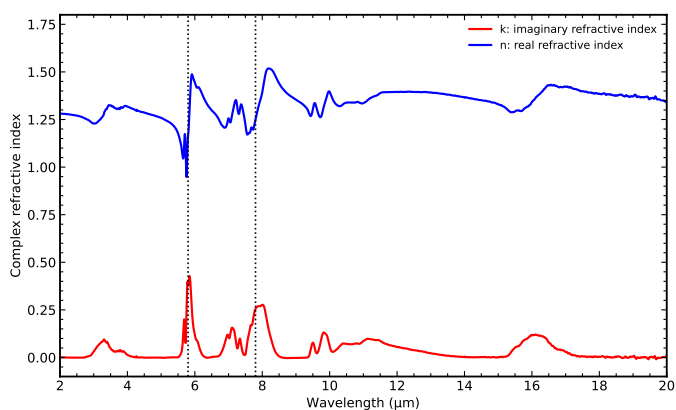


Fig. D.1. Optical contacts of acetic acid. Vertical dotted lines indicate the features with band strength calculated in this paper.

Appendix G: Incremental version of the fits for IRAS 2A and IRAS 23385

Figure [G.1](#) displays the best fits for IRAS 2A (left) and IRAS 23385 (right) by adding one component at a time in each panel. This allows understanding better how each component contributes to the fit.

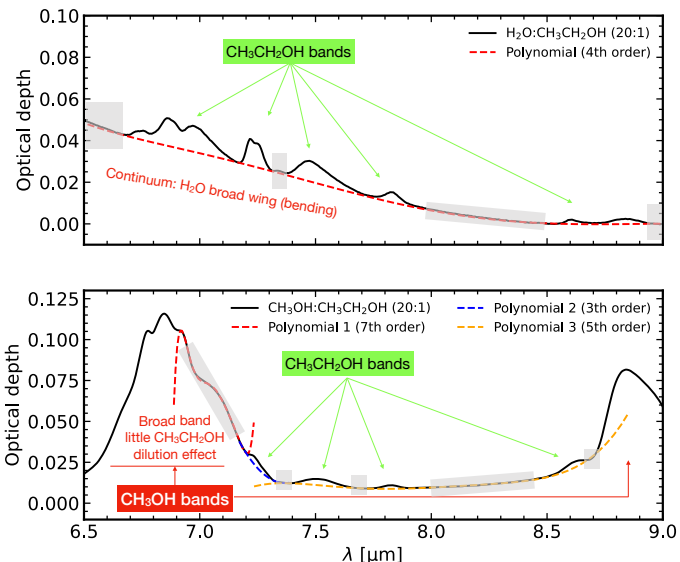


Fig. E.1. Isolating the $\text{CH}_3\text{CH}_2\text{OH}$ ice bands from H_2O and CH_3OH ices. Polynomial functions anchored at the points indicated by the grey areas are used. The top panel shows the ethanol mixed with H_2O ice, and the bottom panel displays the mixture with CH_3OH .

Appendix H: HCOO^- at 14, 150 and 210 K

We compare the absorption profiles of HCOO^- at three temperatures (14 K, 150 K, 210 K) with the 7.2 and 7.4 μm bands in IRAS 2A and IRAS 23385 (Figure [H.1](#)). Our analysis shows that the spectrum at 14 K provides the best fit. The spectrum at 150 K is excluded because the second peak ($\sim 7.4 \mu\text{m}$) is broader and shifted compared to the observations. Likewise, the band shape of the highest temperature data (150 K) does not match with both protostars.

Appendix I: Confidence intervals

The top and bottom panels in Figure [I.1](#) show the confidence intervals for IRAS 2A in the ranges of 6.8–7.5 and 7.8–8.6, respectively. The confidence intervals for IRAS 23385 are shown in Figures [I.2](#) and [I.3](#). For IRAS 2A, it can be noted that all components are essential to the fit, and cannot be excluded. On the other hand, for IRAS 23385, the SO_2 band can be excluded as a solution if the OCN^- band is slightly intense.

Appendix J: Different local continuum profiles between 6.8 and 8.6 μm - IRAS 2A

The first three panels of Figure [J.1](#) show different continuum profiles between 6.8–8.6 μm in the IRAS 2A spectrum. The top panel is the version adopted for the analysis in this paper that traced a third-order polynomial to the guiding points. The second panel displays the fourth-order polynomial where the red dot is added to the guiding points. In this case, the continuum is slightly elevated at shorter wavelengths to accommodate the fit to the extra point at 8.5 μm . The third panel presents the continuum when two extra points are added ($\lambda = 7.8 \mu\text{m}$ and 8.5 μm), and a sixth-order polynomial is used. All subtracted spectra using these three approaches are shown in the bottom panel of Figure [J.1](#).

New fits for IRAS 2A are performed on the other two optical depth spectra obtained from different local continuum choices, which are shown in Figure [J.2](#). The panel at the top shows that all

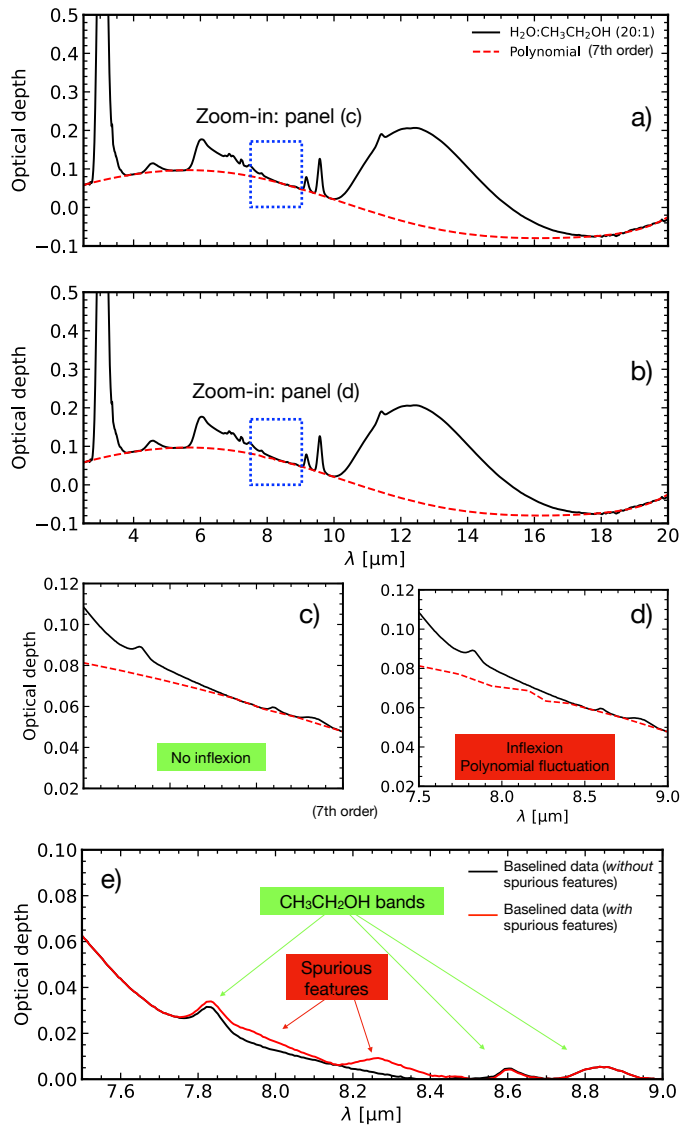


Fig. F.1. Baseline correction of the IR ice spectrum of $\text{H}_2\text{O}:\text{CH}_3\text{CH}_2\text{OH}$ data. Panels a and b show the IR ice spectra and the baselines. The blue dotted squares highlight the zoom-ins shown in panels c and d displaying polynomial baselines without and with little inflexion, respectively. Panel e demonstrates the effect of non-accurate baseline subtraction in the ice spectrum.

Appendix K: Water and methanol ice column densities

1968

1969

The water ice column densities in both protostars are calculated from the libration mode around $12.5 \mu\text{m}$. To determine the profile of the band, we combine water ice spectra at different temperatures (Figure K.1). As pointed out by Boogert et al. (2008), this band is sensitive to the grain geometry. For this reason, we assume small spherical water ice grains which is consistent with Boogert et al. (2008) to fit the libration mode best. The optical constants for ices at 15, 75, and 160 K are taken from Rocha et al. (2022). The water libration band is fitted with two components representing different temperatures. It is likely that the libration band is sensitive to a range of temperatures between 15 and 160 K, but addressing this is beyond the scope of this work. Despite this simplification, one can note that only cold water ice is not enough to fit the libration band of IRAS 23385 and IRAS 2A. In particular, IRAS 2A has a strong blue wing excess that requires H_2O ice at 160 K. The water ice column density is shown in Table 2.

1970

1971

1972

1973

1974

1975

1976

1977

1978

1979

1980

1981

1982

1983

1984

1985

1986

In the case of CH_3OH ice, we use the band at $9.8 \mu\text{m}$ to derive a column density. We fit a Gaussian profile to the feature at $9.8 \mu\text{m}$ (solid curve in Figure K.2) and multiply it by a factor of 2 (dashed curve) and 3 (dotted curve). It is unlikely that the solid curve accounts for all CH_3OH absorption, and therefore the CH_3OH ice column densities used in this paper correspond to the other two Gaussian profiles.

1987

1988

1989

1990

1991

1992

1993

Appendix L: Comparison with hydrocarbons

1994

Because of the degeneracy intrinsic to the ice fittings, particularly regarding COMs that share the same functional groups, we show in this section a comparison of hydrocarbons (C_xH_y) with the IRAS 2A spectrum. These molecules participated in the global fits between 6.8 and $8.6 \mu\text{m}$, but are discarded as solutions. Therefore, these comparisons serve as an additional check that these components are not part of the global minimum solution. Figure L.1 shows scaled IR spectra of pure C_2H_2 , C_2H_4 , C_2H_6 compared to IRAS 2A. The scaling factors are arbitrarily chosen to match the IRAS 2A absorption profile at $7.3 \mu\text{m}$. It can be seen that C_2H_4 does not have any contribution to the 7.2 and $7.4 \mu\text{m}$. On the other hand, the absorption bands of C_2H_2 and C_2H_6 that could be hidden at $7.3 \mu\text{m}$, exceed the IRAS 2A absorption profiles around 12 and $13.5 \mu\text{m}$.

1995

1996

1997

1998

1999

2000

2001

2002

2003

2004

2005

2006

2007

2008

components remain needed to reach the best fit. Only the $8.5 \mu\text{m}$ band of CH_3OCHO exceeds the observations, and this is caused by the guiding point added at $8.5 \mu\text{m}$. The bottom panel of Figure J.2 shows another fit, where two extra points are added at 7.8 and $8.5 \mu\text{m}$. This version of the fit keeps all components, except CH_3COOH , which is excluded because of the anchor point added at $7.8 \mu\text{m}$, where CH_3COOH has a strong feature. Other issues are seen in this fit, for example, around $7 \mu\text{m}$, $7.3 \mu\text{m}$, and a poor fit between 7.8 and $8.6 \mu\text{m}$. Despite all these differences, this analysis shows that CH_3CHO , $\text{CH}_3\text{CH}_2\text{OH}$ and CH_3OCHO are still robust detections, and cannot be excluded from the fits of the IRAS 2A spectrum.

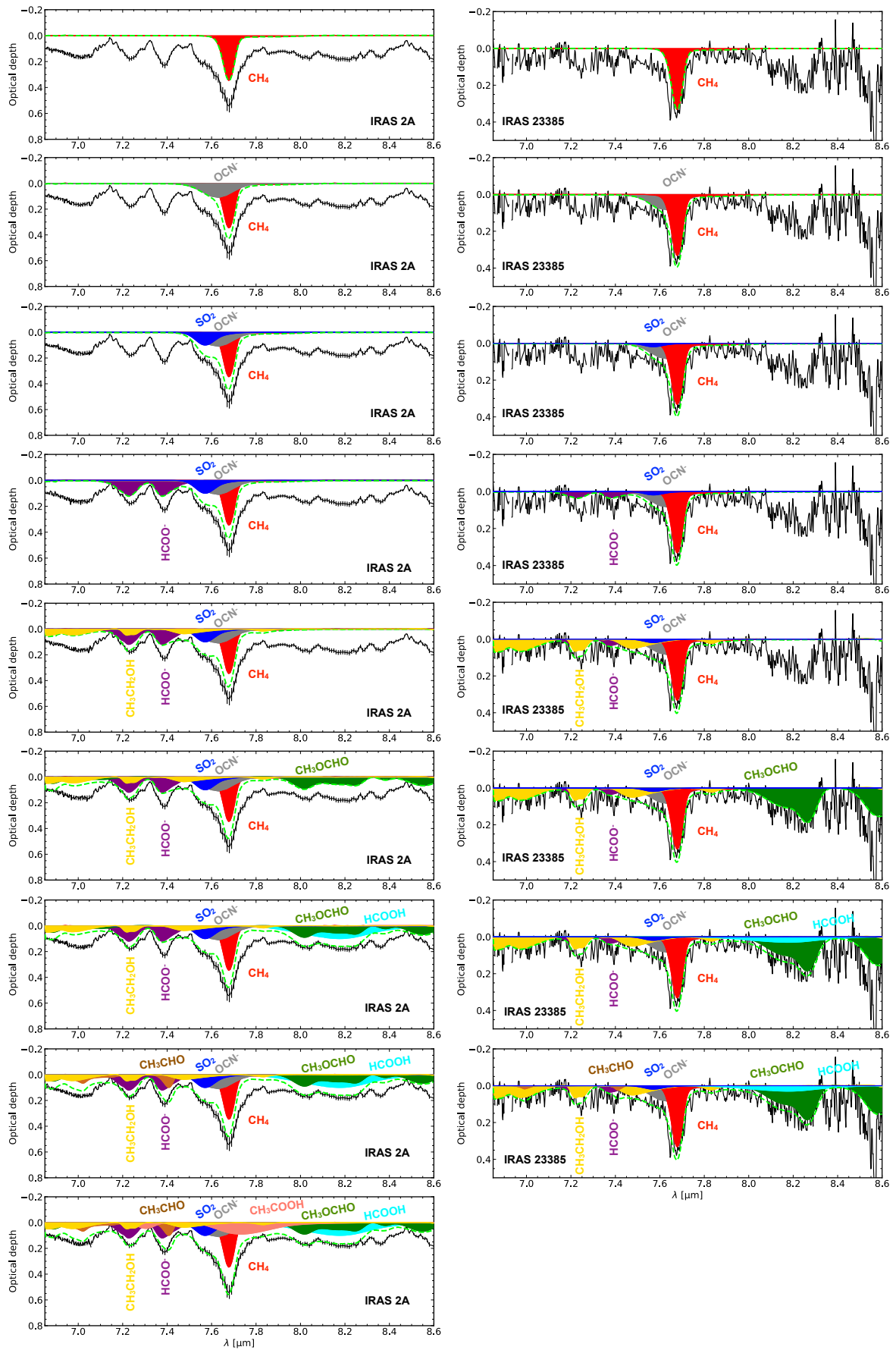


Fig. G.1. Incremental version from top to bottom of the best fits with the ENIGMA fitting tool for IRAS 2A (left) and IRAS 23385 (right). The molecule label follows the colour code of the laboratory components in the fit.

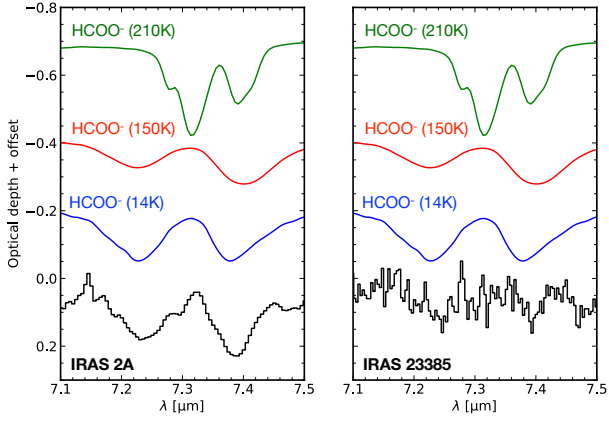


Fig. H.1. Comparison between the 7.2 and 7.4 μm band of IRAS 2A (left) and IRAS 23385 (right) with the HCOO^- absorption profiles at 14, 150 and 210 K. These IR ice spectra are taken from [Gálvez et al. \(2010\)](#).

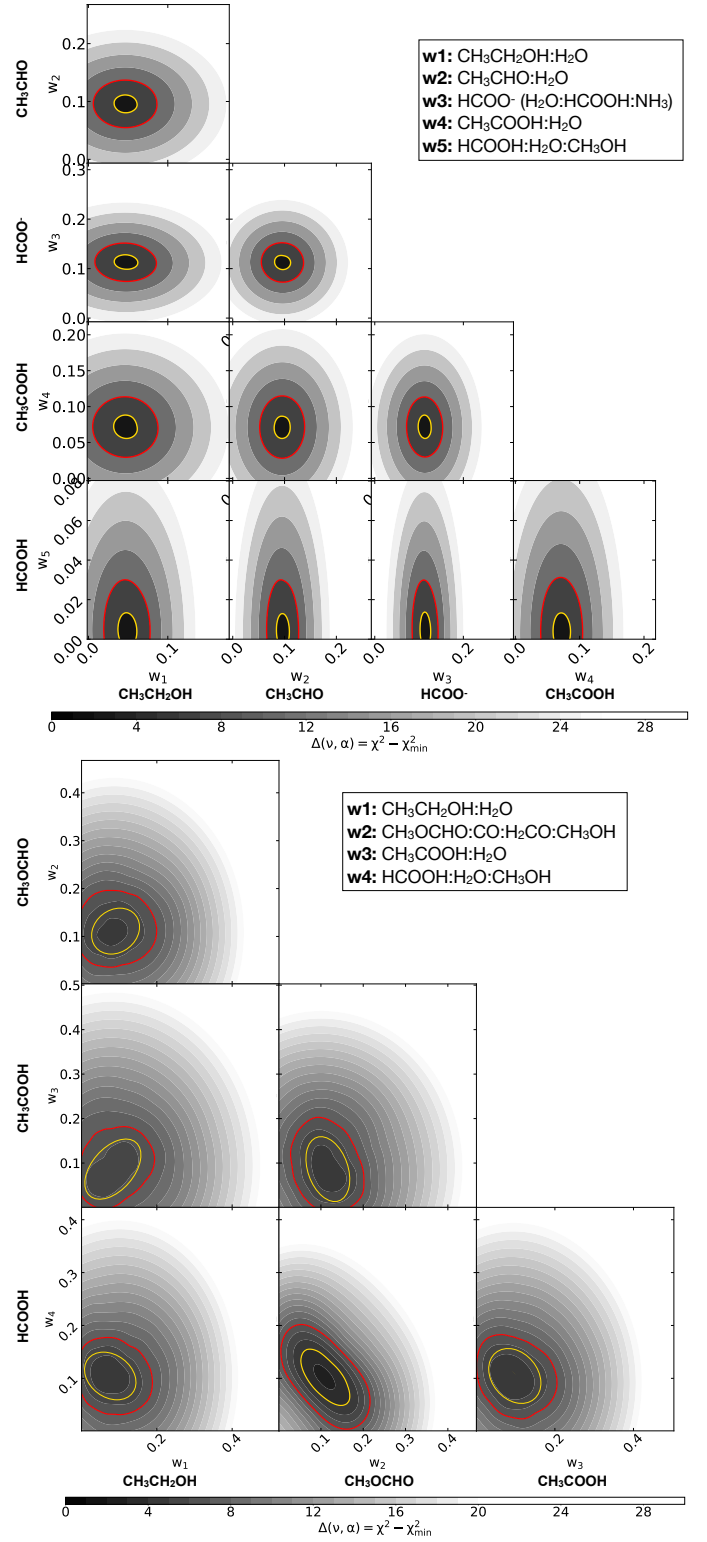


Fig. I.1. The top and bottom corner plots show the IRAS 2A coefficient confidence intervals for the range between 6.86–7.5 (top) and 7.8–8.6 μm (bottom), respectively.

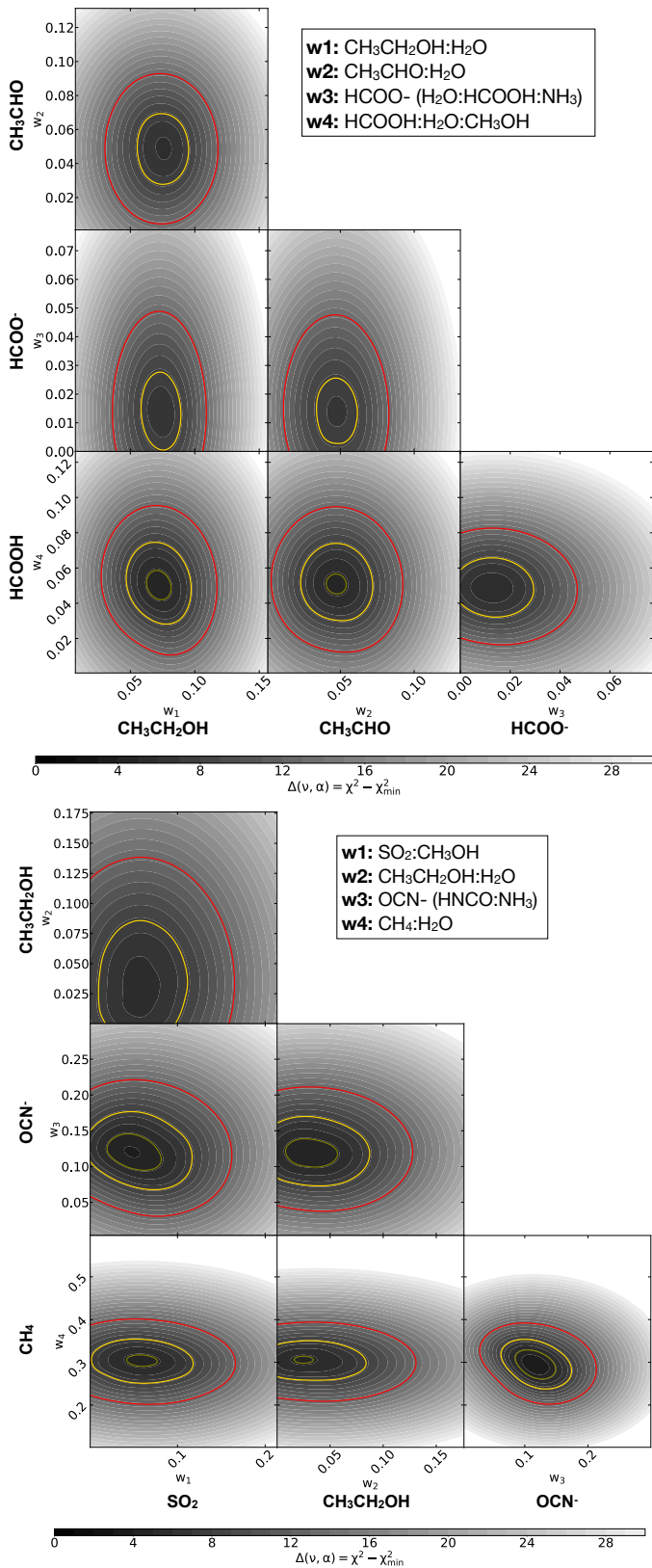


Fig. I.2. The top and bottom corner plots show the IRAS 23385 coefficient confidence intervals for the range between 6.86–7.5 (top) and 7.5–7.8 μm (bottom), respectively.

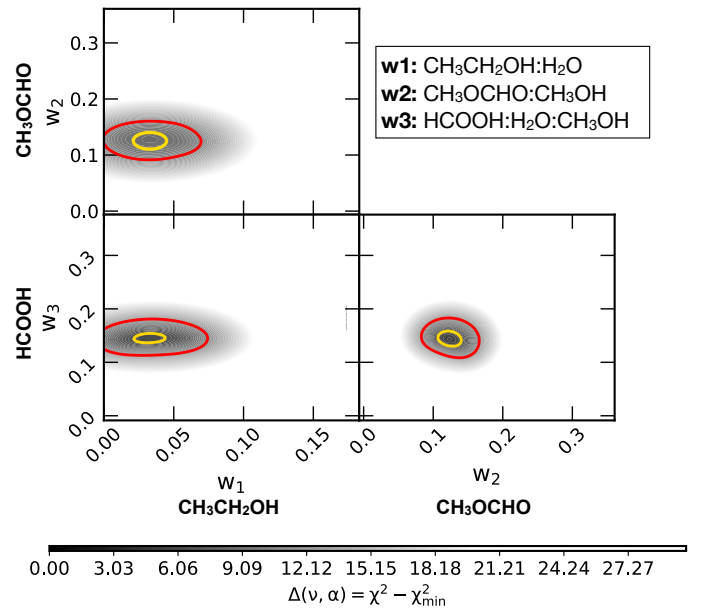


Fig. I.3. Same as in Figure I.2, but for the range 7.8–8.6 μm .

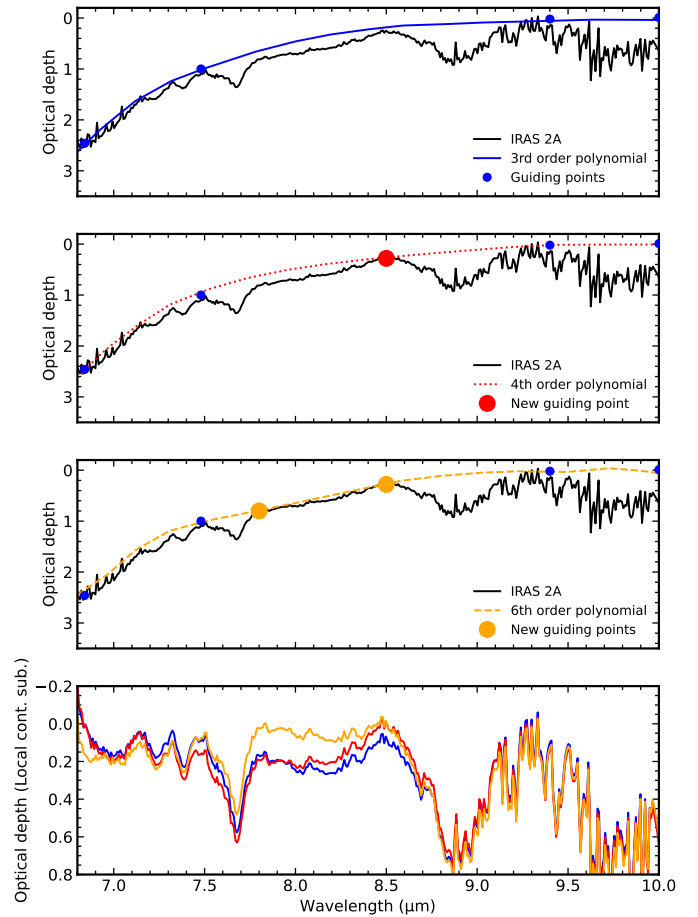


Fig. J.1. Effect of the continuum choice on the local continuum subtracted spectrum of IRAS 2A. The first panel shows the continuum adopted as the best model in this paper. The second and third panels show two other continuum options by adding the red and orange points, respectively. The optical depth subtracted spectra are shown in the fourth panel.

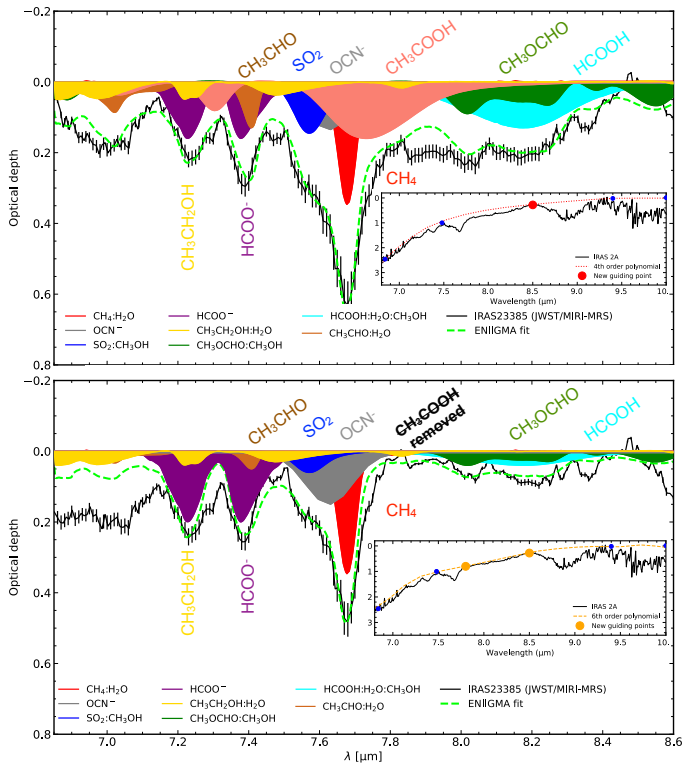


Fig. J.2. Alternative fits of IRAS 2A optical depth spectrum with different local continuum choices (see Figure J.1). The top panel shows the fits with all the components after subtracting the red local continuum with an extra point at $8.5 \mu\text{m}$. The bottom panel shows the same as in the top panel, but considering two extra points for the local continuum (7.8 and $8.5 \mu\text{m}$). Only CH_3COOH is excluded in this fit.

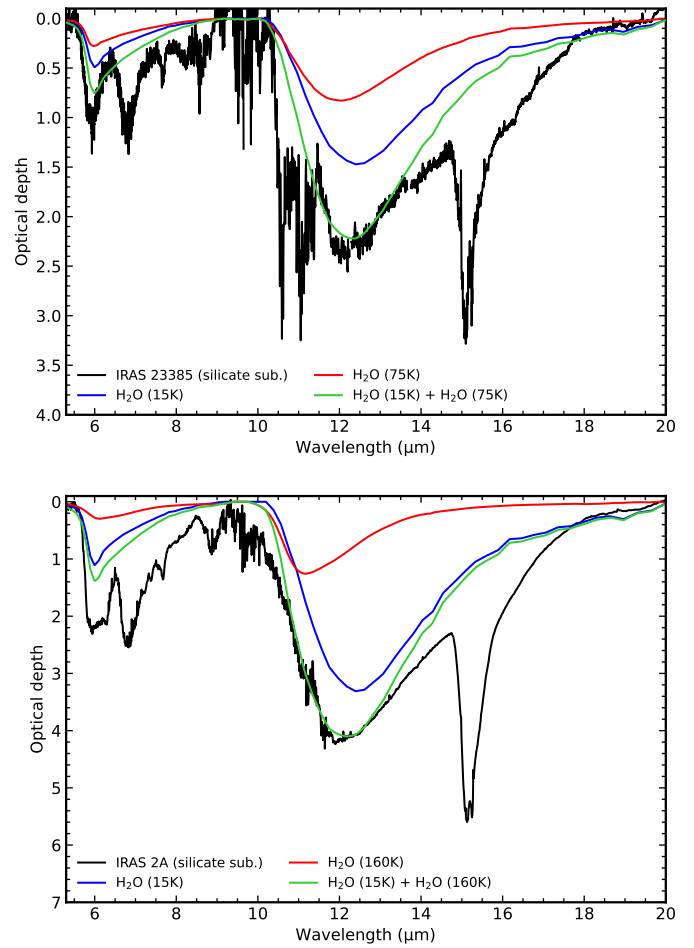


Fig. K.1. Fits for the H_2O ice libration band for IRAS 23385 (top) and IRAS 2A (bottom). The best fit is found by combining two H_2O ice grain-shaped corrected spectra: 15K and 75 K for IRAS 23385 and 15 K and 160 K for IRAS 2A.

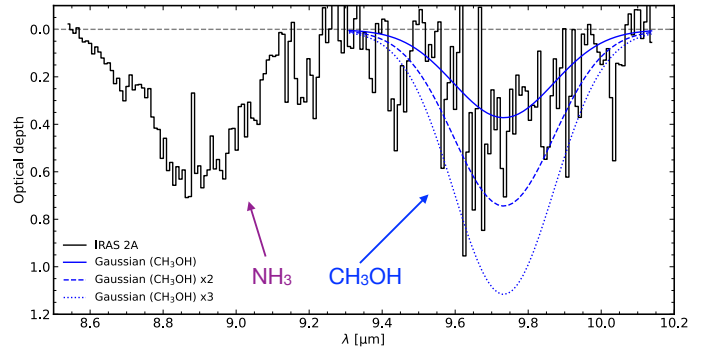


Fig. K.2. NH_3 and CH_3OH features in the bottom of the silicate band and H_2O ice subtracted spectra of IRAS 2A. Three Gaussian profiles are scaled to the CH_3OH band to indicate different ice column densities.

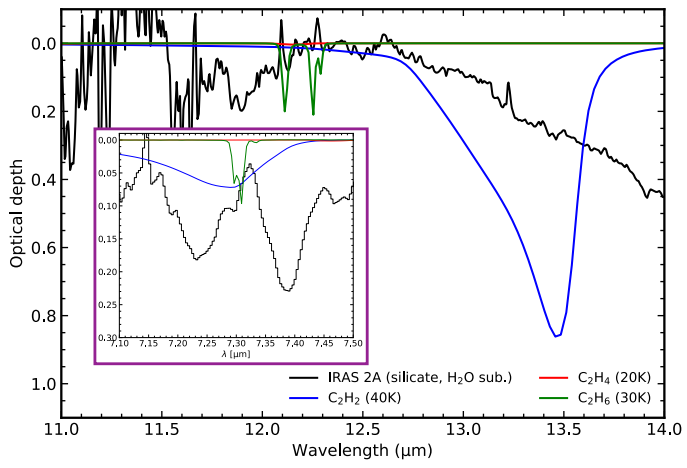


Fig. L.1. Comparison between the 7.2 and 7.4 μm band of IRAS 2A (silicate and H₂O ice subtracted) and hydrocarbons (C₂H₂, C₂H₄ and C₂H₆).

Table C.1. Laboratory data tested in the global fit performed with ENIIGMA.

Label	Temperature (K)	Resolution (cm ⁻¹)	Database ^a	Reference
Simple molecules (less than 6 atoms) and hydrocarbons				
H ₂ O	15–160	2.0	LIDA	[1]
CH ₄	10–30	1.0	OCdb	[2]
HCOOH	15–165	1.0	LIDA	[3]
SO ₂ :CH ₃ OH (1:1)	15	1.0	LIDA	[4]
H ₂ O:CH ₄ (10:1)	15	1.0	UNIVAP	[5]
C ₂ H ₂	15	1.0	NASA	[6]
C ₂ H ₄	15	1.0	NASA	[7]
C ₂ H ₆	15	1.0	NASA	[7]
Ions				
OCN ⁻ :HNCO:NH ₃ (1:1)	15	1.0	LIDA	[8]
HCOO ⁻ :H ₂ O:NH ₃ :HCOOH (100:2.6:2)	14–210	1.0	LIDA	[9]
HCOO ⁻ :NH ₃ :HCOOH (1.3:1)	14–210	1.0	LIDA	[9]
COMs (more than 6 atoms)				
CH ₃ OH	10–120	1.0	OCdb	[2]
CH ₃ CHO	15–120	1.0	LIDA	[10]
CH ₃ CN	15–150	1.0	LIDA	[11]
CH ₃ OCH ₃	15–100	1.0	LIDA	[10]
CH ₃ COCH ₃	15–100	1.0	LIDA	[11]
CH ₃ CH ₂ OH	15–150	1.0	LIDA	[10]
CH ₃ OCHO	15–120	1.0	LIDA	[12]
CH ₃ COOH	10	1.0	NASA	[13]
CH ₃ NH ₂	10	1.0	LIDA	[14]
CH ₃ CH ₂ CH ₂ OH	13	1.0	NASA	[15]
HC(O)CH ₂ CH ₃	10	1.0	NASA	[16]
CH ₃ CH ₂ OH:H ₂ O (1:20)	15–160	1.0	LIDA	[10]
CH ₃ CH ₂ OH:CO (1:20)	15, 30	1.0	LIDA	[10]
CH ₃ CH ₂ OH:CH ₃ OH (1:20)	15–150	1.0	LIDA	[10]
CH ₃ CH ₂ OH:CO:CH ₃ OH (1:20:20)	15–150	1.0	LIDA	[10]
CH ₃ CHO:H ₂ O (1:20)	15–120	1.0	LIDA	[10]
CH ₃ CHO:CO (1:20)	15, 30	1.0	LIDA	[10]
CH ₃ CHO:CH ₃ OH (1:20)	15–140	1.0	LIDA	[10]
CH ₃ CHO:CO:CH ₃ OH (1:20:20)	15–120	1.0	LIDA	[10]
CH ₃ OCH ₃ :H ₂ O (1:20)	15–160	1.0	LIDA	[10]
CH ₃ OCH ₃ :CO (1:20)	15, 30	1.0	LIDA	[10]
CH ₃ OCH ₃ :CH ₃ OH (1:20)	15–120	1.0	LIDA	[10]
CH ₃ OCH ₃ :CO:CH ₃ OH (1:20:20)	15–100	1.0	LIDA	[10]
CH ₃ COCH ₃ :H ₂ O (1:20)	15–160	1.0	LIDA	[11]
CH ₃ COCH ₃ :CO (1:20)	15, 30	1.0	LIDA	[11]
CH ₃ COCH ₃ :CO ₂ (1:20)	15–100	1.0	LIDA	[11]
CH ₃ COCH ₃ :CH ₃ OH (1:20)	15–140	1.0	LIDA	[11]
CH ₃ COCH ₃ :H ₂ O:CO ₂ (1:2.5:2.5)	15–160	1.0	LIDA	[11]
CH ₃ COCH ₃ :CO:CH ₃ OH (1:2.5:2.5)	15–140	1.0	LIDA	[11]
CH ₃ OCHO:H ₂ O (1:20)	15–120	1.0	LIDA	[12]
CH ₃ OCHO:CO (1:20)	15–120	1.0	LIDA	[12]
CH ₃ OCHO:H ₂ CO (1:20)	15–120	1.0	LIDA	[12]
CH ₃ OCHO:CO:H ₂ CO:CH ₃ OH (1:20:20:20)	15–120	1.0	LIDA	[12]
CH ₃ COOH:H ₂ O (1:20)	10	1.0	NASA	[13]
CH ₃ NH ₂ :H ₂ O (1:20)	15–150	1.0	LIDA	[14]
CH ₃ NH ₂ :NH ₃ (1:20)	15–150	1.0	LIDA	[14]
CH ₃ NH ₂ :CH ₄ (1:20)	15–150	1.0	LIDA	[14]
CH ₃ CN:H ₂ O (1:20)	15–150	1.0	LIDA	[11]
CH ₃ CN:CO (1:20)	15–100	1.0	LIDA	[11]
NH ₂ CHO:H ₂ O (7:100)	15–160	1.0	LIDA	[17]
NH ₂ CHO:CO (4:100)	15–34	1.0	LIDA	[17]
HCOCH ₂ OH:H ₂ O (1:18)	10	1.0	NASA	[18]

Notes. [1] Öberg et al. (2007), Gerakines et al. (1996); [2] Hudgins et al. (1993); [3] Bisschop et al. (2007); [4] Boogert et al. (1997); [5] Rocha et al. (2017); [6] Hudson et al. (2014a); [7] Hudson et al. (2014b); [8] Novozamsky et al. (2001); [9] Gálvez et al. (2010); [10] Terwisscha van Scheltinga et al. (2018); [11] Rachid et al. (2022); [12] Terwisscha van Scheltinga et al. (2021); [13] No reference found - taken from the NASA Ice Database (Pure: <https://science.gsfc.nasa.gov/691/cosmicice/spectra/refspec/Acids/CH3COOH/ACETIC-W.txt>, Mixture: https://science.gsfc.nasa.gov/691/cosmicice/spectra/8_compounds/Combined_spectra_2018-12-20.xlsx); [14] Rachid et al. (2021); [15] Hudson & Gerakines (2019); [16] Yarnall et al. (2020); [17] Slavicinska et al. (2023); [18] Hudson et al. (2005). ^aLIDA: The Leiden Ice Database for Astrochemistry (<https://icedb.strw.leidenuniv.nl/>); OCdb: The Optical Constant Database (<https://ocdb.smce.nasa.gov/>); UNIVAP: <https://www1.univap.br/gaa/nkabs-database/data.htm>; NASA Cosmic Ice Laboratory: <https://science.gsfc.nasa.gov/691/cosmicice/spectra.html>

Table D.1. Absolute and apparent band strengths of acetic acid.

λ_{central}	A_{abs} (cm molec ⁻¹)	A_{apr} (cm molec ⁻¹)
5.8	7.5×10^{-17}	7.3×10^{-17}
7.82	4.6×10^{-17}	4.6×10^{-17}